SYNTHESIS AND CHARACTERIZATION OF SILVER NANOWIRES AND MoS₂/METAL OXIDE HYBRIDS FOR ELECTRONICS AND ENERGY APPLICATIONS
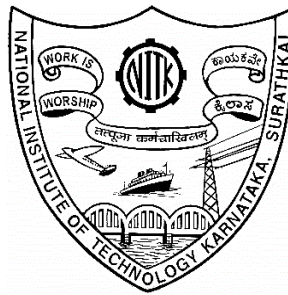
Thesis

Submitted in partial fulfilment of the requirements for the degree of

DOCTOR OF PHILOSOPHY

by

PRABUKUMAR C.

DEPARTMENT OF METALLURGICAL AND MATERIALS ENGINEERING

NATIONAL INSTITUTE OF TECHNOLOGY KARNATAKA

SURATHKAL, MANGALORE - 575025

NOVEMBER, 2021

DECLARATION

I hereby *declare* that the Research Synopsis entitled "**Synthesis and Characterization of Silver nanowires and MoS₂/Metal oxide hybrids for electronics and energy applications**" which is being submitted to the **National Institute of Technology Karnataka, Surathkal** in partial fulfillment of the requirements for the award of the Degree of **Doctor of Philosophy** in the **Department of Metallurgical and Materials Engineering**, is a *bonafide report of the research work carried out by me*. The material contained in this Research Thesis has not been submitted to any other University or Institution for the award of any degree.

Place: NITK, Surathkal

Date: 29.11.2021

Prabukumar C.

145049MT14F04

Department of Metallurgical

and Materials Engineering

CERTIFICATE

This is to *certify* that the Research Thesis entitled "Synthesis and Characterization of Silver nanowires and MoS₂/Metal oxide hybrids for electronics and energy applications" submitted by **Mr. Prabukumar C (Register Number: 145049MT14F04)** as the record of the research work carried out by him, is *accepted as the Research Thesis submission* in partial fulfillment of the requirements for the award of degree of **Doctor of Philosophy**.

Research Guide

Uaapthet·k

Prof. Udaya Bhat K.

Professor

Department of Metallurgical and Materials Engineering

NITK, Surathkal

Chairman - DRPC

Department of Metallurgical and Materials Engineering

NITK, Surathkal

Chairman - DRPC
Dept. of Metallurgical and Materials Engineering
National Institute of Technology Karntaka, Surathkal
Post Srinivasnagar, Mangaluru - 575 025
Karnataka, India

ACKNOWLEDGEMENT

This thesis becomes a reality with the kind support and help of many individuals. I would like to extend my sincere thanks to all of them.

I express my heartfelt gratitude to my research supervisor Prof. Udaya Bhat K., Department of Metallurgical and Materials Engineering, for his continuous support, and motivation and immense knowledge that he has shared with me, whilst allowing me the room to work in my way. His unwavering guidance has helped me in making the appropriate decisions and to remain optimistic during critical times.

I am indebted to The Director, NITK and present Head of the Department, Prof. K. Narayan Prabhu and former department heads Prof. Jagannath Nayak and Prof. S. Anandhan. They have extended their generous support by providing required facilities and support during my doctoral research work. I would like to acknowledge MHRD, Govt. of India for providing financial support for this work in the form of the Institute research fellowship.

I am very thankful to my research progress committee members, Dr. Saumen Mandal, Assistant Professor, Department of Metallurgical and Materials Engineering and Dr. Srikanth Bontha, Associate Professor, Department of Mechanical Engineering, for their valuable technical input and encouragement during this research work.

I extend my sincere thanks to Prof. M.N. Satyanarayan, Department of Physics, Dr. Shashi Bhushan Arya, Assistant Professor and Dr. Saumen Mandal, Assistant Professor, Department of Metallurgical and Materials Engineering for providing me their laboratory facilities to carry out my research work. I express my heartfelt gratitude to all the faculties of Dept. of Metallurgical and Materials Engg. for their constant guidance and support

It has been my pleasure to have supportive fellow researchers who would always help with my research work. I thank Dr. Arun Augustin, Dr. Prashant Huilgol, Dr. Jayalakshmi M., Dr. Sunil Meti, Dr. Nandana M.S., Mr. Sudhish R. and Mr. Naveen Bharadishettar. I express my gratitude to all the fellow research scholars of the department. I am deeply grateful for my friends Dr. Sivananth M., Dr. Marimuthu C.,

PRABUKUMAR C.

To

the immeasurable forces of nature

ABSTRACT

The present study focuses on two important aspects of next-generation electronics and energy storage devices. One is the flexible transparent conductive electrode fabricated using silver nanowires. Another is the ZnO anode used in zinc alkaline batteries. The silver nanowires transparent conductive films are the potential alternative to widely used high-cost, brittle indium tin oxide (ITO). The silver nanowires are synthesised by following the polyol method. Among many synthesis parameters, the oxygen scanger is important for the growth of longer silver nanowires. These oxygen scavengers (ex: Cu or Fe ions) help to prevent the blocking/etching of silver seed particles from atomic oxygen adsorbed on their surface. This work explores the use of manganese ions as the oxygen scavengers during the silver nanowires synthesis due to the multiple oxidative states of manganese. The silver nanowires are synthesised in different chloride conditions: no chloride, NaCl, $CuCl_2$ and $MnCl_2$. The silver nanowires synthesised with the presence of Mn(II) ions and Cl^- ions show more uniform, longer nanowires with a smaller diameter than that synthesised with the presence of Cu(II) ions. The transparent conductive films are fabricated by the spray coating method using the silver nanowires synthesised with Mn(II) ions. Three films with optical transparency (at 550 nm) and sheet resistance of 81% & 40 Ω/sq., 79% & 29 Ω/sq. and 80% & 34 Ω/sq. are produced. The silver nanowires film shows excellent mechanical flexibility. The heater test conducted on the silver nanowires film achieved a temperature of 90 °C.

Factors like the dissolution of Zn anode, hydrogen gas evolution, shape change make the Zn/ZnO anode in zinc alkaline batteries difficult to recharge. These problems can be mitigated by tailoring the morphology of the anode and incorporating desirable additives with the anode. Tin oxide (SnO_2) is an excellent additive to Zn/ZnO. The poor charge transfer within SnO_2 due to volume expansion and microcracks are the drawbacks of using SnO_2. The liquid phase exfoliated MoS_2 nanosheets are used as the support material to facilitate the charge transfer between the SnO_2 nanoparticles. The nanocomposite of MoS_2 nanosheets and SnO_2 nanoparticles (MoS_2-SnO_2) is prepared by the ligand exchange process. The ratio of MoS_2 in SnO_2 is optimized by conducting the supercapacitor characterizations such as cyclic voltammetry, electrochemical impedance spectroscopy and charge-discharge study.

The prepared MoS_2-SnO_2 nanocomposite is tested as an additive with ZnO. For this purpose, the ZnO with three different morphology is used. First, commercial ZnO nanoparticles with plate-like, spherical-like morphology. Second, ZnO nanorods synthesised by microwave heating method. Third, ZnO microrods synthesised by hydrothermal method. The solubility study conducted by atomic absorption spectroscopy shows that the one-dimensional ZnO microrods and nanorods dissolve slower in KOH electrolyte than the ZnO with plate-like and sphere-like morphology. The three ZnO materials with and without the MoS_2-SnO_2 additive are subjected to hydrogen gas evolution, corrosion test, electrochemical impedance spectroscopy and cyclic voltammetry. The electrochemical performance of ZnO with MoS_2-SnO_2 additive is better than the bare ZnO. Among all the samples, the performance of MoS_2-SnO_2/ZnO nanorods is excellent and the most suitable anode material to be used in the alkaline battery.

CONTENTS

List of Figures

List of Tables

List of Abbreviations

AAS	Atomic absorption spectroscopy
BET	Brunauer–Emmett–Teller
EIS	Electrochemical impedance spectroscopy
FESEM	Field emission scanning electron microscopy
HER	Hydrogen evolution reaction
ICDD	International Centre for Diffraction Data
ITO	Indium tin oxide
IUPAC	International Union of Pure and Applied Chemistry
MR	Microrods
MTP	Multiply twinned particle
NP	Nanoparticles
NR	Nanorods
PVA	Polyvinyl alcohol
PVP	Polyvinylpyrrolidone
SAED	Selected-area electron diffraction
SEM	Scanning electron microscopy
TCE	Transparent conductive electrode
TEM	Transmission electron microscopy
UV-VIS	Ultraviolet-Visible
XPS	X-ray photoelectron spectroscopy
XRD	X-Ray diffractometry

CHAPTER 1

INTRODUCTION

The next-generation electronic devices such as flexible displays, paper solar cells, health monitoring patches and sensors are set to meliorate the day-to-day life of the humankind (Brunetti et al. 2019) (Yuan et al. 2019). These devices will be supported by the energy storage systems like flexible thin film supercapacitors and batteries (Gao et al. 2021). These flexible electronic devices are different from the conventional electronic devices in many aspects. They are made on polymers, textiles or soft substrates, in contrast to existing devices based on the rigid substrates. They are designed to work in complex non-planar shapes to utilize the full potential of the devices and materials used in them.

1.1 Flexible Electronics

1.1.1 Sensors

Nanogenerators can harvest electrical energy from the mechanical motions or the vibrations by the piezoelectric principle. When a piezoelectric material, such as ZnO, is subjected to mechanical deflections, there will be flow of electrons. The ZnO nanowires could be integrated into wearable devices to monitor human health by their body movements (Panth et al. 2020). This can be mounted on a moving part of a human body and can also charge portable devices, such as mobile phones (Thakur et al. 2018).

1.1.2 Optoelectronic devices

The solar cell is an optoelectronic device, is a future system for green energy generation. The commercial silicon solar cells can only be used as planar-shaped panels as the materials used in them are primarily brittle. The organic solar cells (OSC) are the potential technology devices for the future as these are flexible systems and can be used in any shape (Reddy et al. 2017). Such cells can be used in roofs, windows or even on clothes to charge the portable/wearable devices.

1

Another optoelectronic device is the light-emitting diode (LED). Like OSCs, organic LEDs (OLED) are flexible. These can be rolled as paper and put into the pocket. Also, they can be used in touch screens and wearable devices, like smart watches (Fukagawa et al. 2018).

1.1.3 Film heaters

The transparent conductive film based heaters are used to defrost/defog the front panels of aircraft, automobile windshields and wearable devices (Tiwari et al. 2017) (Lee et al. 2020). The film heaters are also used as thermography patches to treat arthritis-related illness (Sharma et al. 2020).

1.2 Transparent Conductive Materials

The transparent conductive electrode (TCE) is an essential element in the devices mentioned above. The indium tin oxide (ITO) is the most widely used TCE material in OSCs and OLEDs. It has excellent optical transparency (more than 95 %) and low-sheet resistance (5-10 Ω/sq). ITO is a brittle metal oxide. The mechanical flexibility, a critical property for any flexible devices, is limited in the devices that use ITO as the TCE (Chen et al. 2001). Also, the cost of the material is high because of the low abundance of indium. Therefore, there is a need for an alternative material to replace high-cost, brittle ITO to develop sustainable flexible devices.

Low-sheet resistance, high optical transparency and mechanical flexibility are the critical properties for a flexible transparent conductive film. Graphene, carbon nanotube (CNT), metal nanowires have been explored to replace the ITO. Single-layer graphene is a promising candidate, but synthesis of single-layer graphene using the chemical vapor deposition (CVD) technique is expensive. Graphene produced by the exfoliation of graphite is not uniform and has poor electrical properties. Similarly, CNT grown from the CVD route has high junction resistance between the nanotubes. There are metal nanowires (NWs) mesh electrodes made up of copper and silver. Copper (Cu) is a more abundant material than the silver (Ag). But the optical transparency (93 %) and lower sheet resistance (20 Ω/sq) of Ag NWs based electrodes (Chang et al. 2014) are

too far to reach by Cu NWs based electrodes. It has an optical transparency of 85 % and sheet resistance of 31 Ω/sq (Zhang et al. 2020a).

1.2.1 Silver nanowire electrode

The TCE films fabricated using silver nanowires show excellent transparency and low sheet resistance close to ITO. The optical transparency and electrical conductivity of the Ag NWs film depend on the length and diameter of the nanowires and the density of nanowires in the film. The Ag NWs film can reach 93% transparency with a sheet resistance of less than 20 Ω/sq. The mechanical flexibility of Ag NW film is excellent when compared with the ITO and fluorine-doped tin oxide (FTO). The Ag NW film retains its lower sheet resistance even after many bending cycles (Langley et al. 2013). It can be bent to a bending radius of 5 mm without any loss in electrical conductivity.

1.2.2 Problem of oxidative blocking/etching in the synthesis of Ag nanowires

The one-dimensional growth of the silver nanowires is often hindered by oxidative blocking or etching of silver seed particles during the polyol synthesis process (Wiley et al. 2004). Wiley et al. (2005) and Korte et al. (2008) reported that the introduction of Fe(II)/Fe(III) and Cu(I)/Cu(II) ions during the synthesis process prevented this oxidative blocking of silver seeds and enhanced the growth of silver nanowires. Due to their dual oxidative states, copper and iron are proven to remove the oxygen from the silver seeds through the redox process. Amongst copper and iron, the copper ions showed better results than the iron ions (Bob et al. 2016) (Ma and Zhan 2014). However, the silver nanowires synthesised in the presence of Cu(II) tend to have large diameters, in the range of 125-250 nm (Bob et al. 2016).

Many efforts are put to improve the aspect ratio (length to diameter) of the silver nanowires. Some of them are multistep synthesis (Li et al. 2015), replacing the small chain length PVP molecules with the longer chain PVP molecules (Sonntag et al. 2019), the addition of Br$^-$ ions (Zhang et al. 2018a), synthesising in high pressure (Zhang et al. 2017b) and N$_2$ gas environments (Niu et al. 2018) along with the use of oxygen scavengers, like copper or iron ions. Despite the improvements achieved by tailoring

other parameters, the presence of oxygen scavengers (like Cu/Fe ions) remains crucial in the synthesis of silver nanowires (Zhang et al. 2019).

1.3 Flexible Batteries

The wearable devices have to be incorporated with an energy storage device to ensure continuous supply of the electrical energy. The bio-integrated devices which monitor body movements and blood pulse will experience compression, bending and twisting deformations (Berchmans et al. 2014).

1.3.1 Available battery cells

Lithium-ion batteries are the current leaders in battery domain. These batteries are attractive due to their high open-circuit voltage, low self-discharge and lack of memory effect. But there are many problems along with these merits. The use of hazardous non-aqueous solvents, the need for careful encapsulation to protect these materials from the environmental contact are some of the demerits (Wang et al. 2012). The issues of safety problems and low specific energy (150 Wh Kg^{-1}) increase concerns when used in wearable human-interface devices and underwater applications.

The zinc alkaline batteries like Zn-Ag, Zn-Ni, Zn-Mn and Zn-air are used in many electronic systems ranging from wrist watches to missiles, space and underwater equipments. Unlike lithium-ion batteries, zinc alkaline batteries have the following favourable characteristics (Karpinski et al. 1999),

- Very high specific energy (up to 1084 Wh kg^{-1}) and volumetric energy density (up to 750 Wh dm^{-1})
- High rate discharges and linear voltage over the entire range of its discharge
- Low self-discharge rate (5% per month)
- Safe and environmentally friendly system

As the Zn alkaline batteries are safe and reliable, they can be used to power the wearable devices (Huang et al. 2019b).

1.3.2 Working principle of Zn-Ag battery

The charging and discharging of a zinc-silver battery may be represented by a single reversible equation given below (Eqn. 1 and 2). The anode and cathode are made up of zinc (Zn) metal and silver oxide (Ag_2O), respectively. The aqueous solution of salts LiOH, NaOH and KOH are used as the electrolyte in such batteries. But the KOH solution is widely used as the electrolyte because of its high ionic conductivity. The OH^- anions in the electrolyte act as the charge carriers during the electrochemical cycle (Berchmans et al. 2014).

$$
\begin{array}{cc}
\textit{Cathode} & \textit{Anode} \\
Ag_2O \quad + & Zn \quad\quad\quad\quad\quad (1) \\
\\
\textit{Charge} \quad \Big\updownarrow \quad \textit{Discharge} \\
\\
2Ag \quad + & ZnO \;+ \text{Electrical energy} \quad (2)
\end{array}
$$
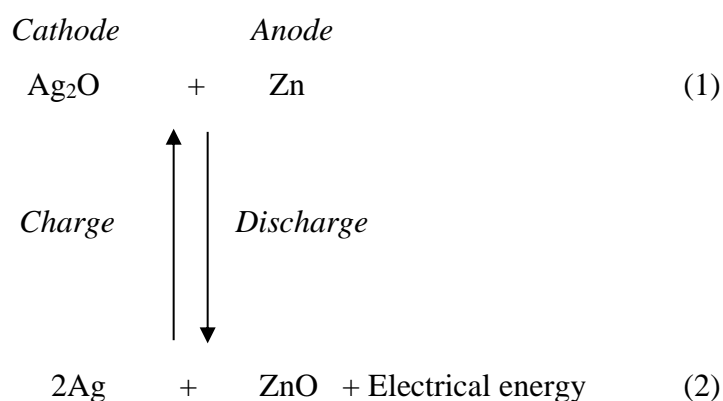
During discharging, the silver oxide is reduced to silver and the zinc is oxidized to zinc oxide (ZnO). The chemical process is reversed during charging after the cell has been discharged. The oxidation and reduction reactions of Zn anode are the same in other Zn alkaline battery systems, such as Zn-Ni, Zn-Mn and Zn-air.

1.3.3 Limitations of Zn alkaline batteries

1.3.3.1 Dissolution of the Zn anode material

High dissolution rate of the Zn/ZnO material in the highly corrosive alkaline electrolyte (KOH) is one of the significant factors for the short lifetime of Zn alkaline batteries. During discharge, the Zn metal is converted into $Zn(OH)_4^{2-}$ ions. These zincate ions slowly dissolve into the electrolyte solution (Mainar et al. 2018b). When the electrolyte near the anode is saturated with the zincate ions, the zincate ions precipitate into compact irreversible ZnO on the anode. A layer of thick ZnO passivates the active

5

anode particles (Mainar et al. 2018a). The cycle life and reversibility of the battery are reduced due to the dissolution and passivation of the Zn/ZnO anode.

1.3.3.2 Dendrites growth

The high dissolution of zincate ions causes another problem of dendrite growth in the anode. During the charging process, the zincate ions are reduced back to metallic Zn. This process is called Zn plating. The local dissolution of Zn and concentration differences lead to the non-uniform deposition of Zn. This non-uniform deposition is the reason for the shape change and the dendritic growth. The dendrites continue to grow and pierce the separator. This leads to a short circuit of the anode with cathode causing failure of the battery. Also, the change in shape decreases the active surface area of the anode material (Ozgit et al. 2014).
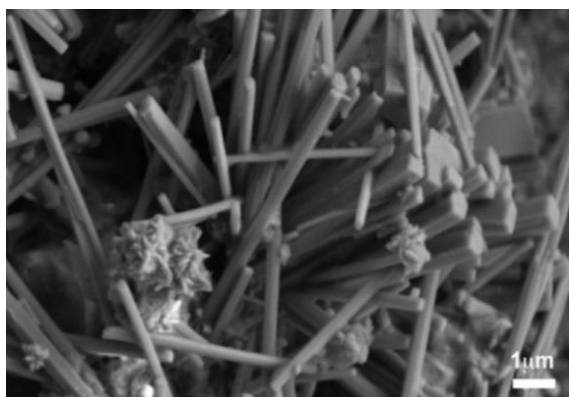
Figure 1.1 SEM micrograph shows the dendrite formation on Zn electrode (Ozgit et al. 2014)

1.3.3.3 Evolution of hydrogen gas

The evolution of hydrogen (H_2) gas is due to the undesirable water electrolysis reaction during the charging process. The evolution of H_2 gas would lead to increase in the internal pressure of the battery, loss of water in the electrolyte and corrosion of the Zn/ZnO anode that produces $Zn(OH)_2$ (Turney et al. 2017) (Mainar et al. 2018a).

Hence, the present study focuses on transparent conductive silver nanowires film and Zn anode for the alkaline battery. The study aims to synthesis uniform, longer and high aspect ratio silver nanowires in the presence of different oxygen scavengers. The

fabrication and characterization of transparent conductive silver nanowires film are also discussed. The present study also investigates the effect of size and morphology of the ZnO anode on their electrochemical performance in the KOH electrolyte. The preparation and analysis of MoS_2-SnO_2 nanocomposite as the additive to the ZnO are also discussed. The details of the study are represented in this thesis as different chapters. The review of relevant literature is presented in chapter two. The experimental details on synthesis, fabrication and various characterization techniques are given in chapter three. The results and discussion on transparent conductive silver nanowires film are presented in chapter four. Chapter five and six discusses the synthesis and characterization of MoS_2 nanosheets and MoS_2-SnO_2 nanocomposite, respectively. The results of the ZnO anode are discussed in chapter seven. The inferences of the present study are summarised in chapter eight. After the list of references, the publications based on this study are listed.

CHAPTER 2

LITERATURE REVIEW

The literature reviews on the synthesis, characterization and applications of transparent conductive silver nanowires, ZnO anode for alkaline battery, MoS₂ nanosheets and tin oxide nanoparticles for energy storage applications are presented in this chapter.

2.1 Review on Silver Nanowire Transparent Conductive Electrodes

Silver nanowires (Ag NWs) are prepared by different routes. Filling the silver metal into the carbon nanotubes (Govindaraj et al. 2000), use of co-polymers to form silver aggregates to grow into wires (Zhang et al. 2001) and electrochemical deposition of the silver into the pore of anodic alumina membrane (AAM) (Zong et al. 2004) are some template-based methods to synthesis silver nanowires. Ag NW is also produced by the polyol method by using the reduction reaction of silver nitrate by the ethylene glycol. The poly (vinyl pyrrolidone) (PVP) act as a capping agent (Sun et al. 2002a). The dimensions of the nanowires produced by the template route were limited to the template dimension. The nanowires produced by this method often form into aggregate bundles. The additional process to remove the template from nanowires adds up with forementioned drawbacks to look into other easier routes for silver nanowire synthesis. On the other hand, the polyol process does not have any such problems and it is a convenient route to produce the Ag NWs on a large scale.

2.1.1 Polyol synthesis of silver nanostructures

Silver nitrate ($AgNO_3$) is used as the silver source in the polyol method. Ethylene glycol is used as the solvent and reducing agent for the silver nitrate. Poly (vinylpyrrolidone) (PVP) is used to act as the capping agent. The experiment is conducted in a round bottom flask under magnetic stirring in a heated oil bath. The Ag^+ ions from the $AgNO_3$ get reduced to form silver nanoparticles and they continue to grow into large particles by Oswald ripening. PVP agent passivates some of the facets of these particles and thus controls the growth in a particular direction (Coskun et al. 2011).

The Ag$^+$ ions from the AgNO$_3$ solution are reduced by ethylene glycol when it is introduced into the heating flask (Figure 2.1). This leads to the formation of silver nuclei (step I). These nuclei grow and reach critical size (step II). Because of the available thermal energy associated with these nuclei, the structure fluctuates and allows defects to form (Baletto and Ferrando 2005, Wiley et al. 2007). The twin boundary defects are preferred to form due to the low surface energy.
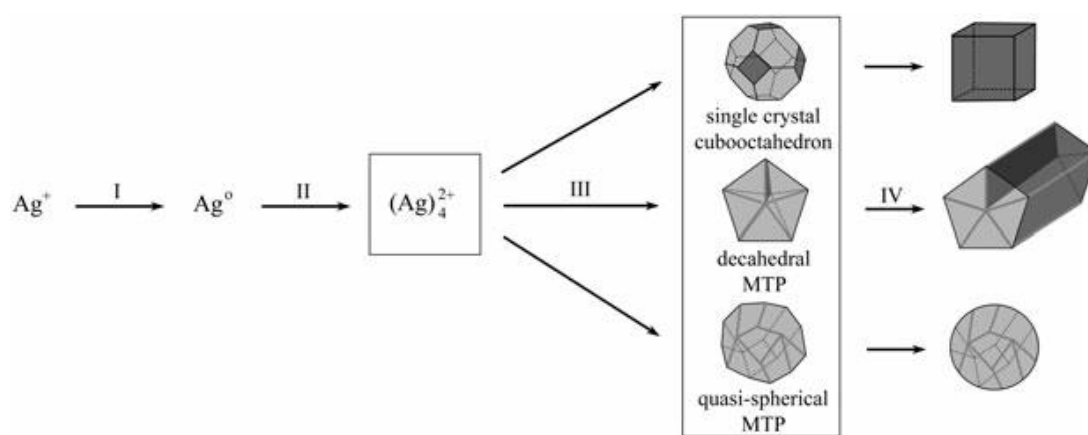
Figure 2.1 Growth of silver nanostructures (Wiley et al. 2005)

With respect to the reduction rate of Ag$^+$ ions, single crystal seed, multiply twinned with 5-fold decahedron and quasi-sphere defects are formed (Wiley et al. 2005).

2.1.2 Growth mechanism

Earlier, it was mentioned that the thermal energy fluctuations during the nucleation stage lead to the formation of twin defects to lower the surface energy. These twins act as the seeds for the growth of the nanostructures. Amongst all twin seeds (crystal, single twin, multiple twins), multiply-twinned decahedra are the most stable seed, as it is bound by {111} facets. Therefore, it is the most abundant seed for the growth of silver nanostructures.
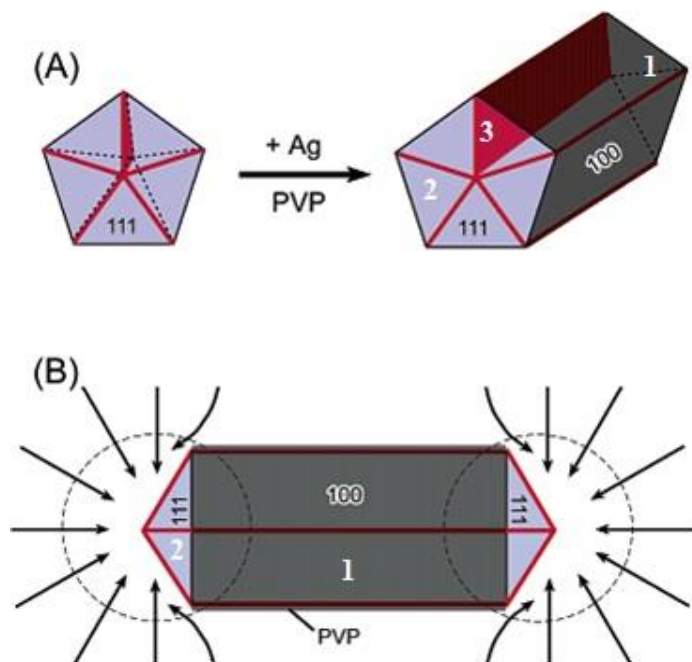
Figure 2.2 Growth mechanism of a silver nanowire (Sun et al. 2003)

Figure 2.2 (A) explains the evolution of a nanorod from a multiply twinned nanoparticle (MTP) of silver under the confinement of five twin planes and with the assistance of PVP. The ends of this nanorod are terminated by {111} facets, and the side surfaces are bounded by {100} facets. The strong interaction between PVP and the {100} facets is indicated with a dark-grey shaded colour (region 1), and the weak interaction with the {111} facets is marked by a light shaded colour (region 2). The MTP consists of five single-crystal tetrahedrons oriented radially about a central axis. All the five tetrahedrons share a common edge in the centre and each tetrahedron has two sides in contact with its neighbours. Each tetrahedron can share an angle of only 70.5°, leaving a gap of 7.5°. Significant lattice distortions, surface relaxations and defects could occur to make up for this angle difference (Wiley et al. 2004). In this case, the twin boundaries (dark lines on the end surfaces) are formed that can serve as active sites for the addition of new silver atoms. The plane marked in the dark colour (region 3) shows one of the five twin planes that can serve as the internal confinement for the evolution of nanowires from MTP. Figure 2.2 (B) is a schematic model illustrating the diffusion of silver atoms toward the two ends of a nanowire, with the side surfaces completely passivated by PVP. This drawing shows a projection perpendicular to one of the five side facets of a nanowire and the arrows represent the diffusion fluxes of silver atoms.

2.1.3 Synthesis of silver nanowires

The silver nanowires were successfully synthesised (Sun et al. 2002a) by injecting AgNO$_3$ dissolved in ethylene glycol into a preheated flask containing PVP dissolved in ethylene glycol. Then, PtCl$_2$ dissolved in ethylene glycol was added, followed by the addition of AgNO$_3$ solution. The Pt nanoparticles acted as heterogeneous nucleation sites for nanowires. The flask was under magnetic stirring continuously. The heating and stirring were continued till the colour of the solution became grey. This grey colour was the indication of the formation of silver nanowires.

Sun and Xia (2002) synthesised Ag NWs without Pt seeds by injecting 3 mL ethylene glycol (0.1 M) solution of AgNO$_3$ and 3 mL ethylene glycol solution of (0.6 M) of PVP into a flask containing 5 mL ethylene glycol. The reaction was continued under magnetic stirring at 160 °C for 60 min. The final solution was washed with acetone by centrifugation to remove the PVP and undesired particles produced as the byproducts.

When silver ions are introduced into the solution, the silver ions are reduced rapidly to Ag^0 state. This rapid reduction leads to the formation of silver aggregates (Hyning and Zukoski 1998). Inorganic ions, such as Cl$^-$ or Br$^-$ are introduced into the solution to form AgCl or AgBr. These silver halides act as the buffer phase. That ensures the controlled supply of silver species into the reaction. In this way, the chloride ions help as the electrostatic stabilizer to prevent the formation of silver aggregation and promote the one-directional growth of silver nanostructures.

2.1.4 Oxidative etching of silver seed particles

As mentioned earlier, the twinned particles produced in the early stages are the seeds, for the growth of silver nanowires. During the synthesis, the molecular oxygen (O$_2$) present in the reaction solution dissociates into atomic oxygen. These atomic oxygen then get adsorbed on the surface of the silver seed particles. The adsorbed atomic oxygen, to some extent, may cause the etching of these twinned particles. But, notably, they block the addition of new silver atoms to {111} reaction sites. So, the growth of the nanowires is affected by this adsorbed oxygen (Wiley et al. 2004).

2.1.5 Role of Fe^{3+} and Cu^{2+} ions

The iron ions were introduced into the reaction to prevent the twins from oxygen etching/blocking. At the reaction temperature of 148 °C, the Fe (III) ions were reduced to Fe (II) ions by ethylene glycol. The Fe (II) ions react with this atomic oxygen and get oxidized back into Fe (III) ions. This way, the oxygen was removed from the silver seeds to help the growth of silver nanowires (Wiley et al. 2005). Copper ions were used in place of iron ions as the oxygen scavenger (Korte et al. 2008) (Wang et al. 2016b). The addition of CuCl or $CuCl_2$ was effective in enhancing the growth of silver nanowires. But the diameter of the silver nanowires synthesised with the addition of copper or iron ions was more than 120 nm (Bob et al. 2016).
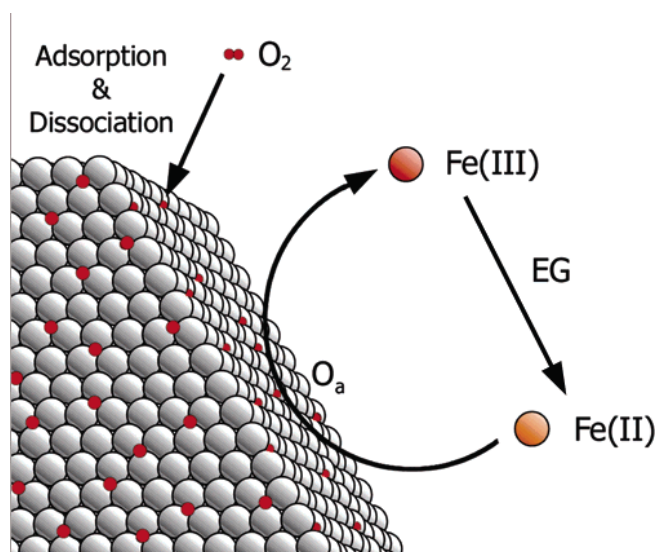
Figure 2.3 Oxygen scavenging from the surface of silver seed particle (Wiley et al. 2005)

Recently, researchers used Co^{2+} ions and Cr^{2+} ions as the oxygen scavengers in place of Fe^{3+} and Cu^{2+} ions (Abbasi et al. 2016) (Zhang et al. 2019).

2.1.6 Process parameters

In polyol synthesis, the process parameters such as $PVP/AgNO_3$ ratio, reaction temperature, amount of NaCl, injection rate of $AgNO_3$ precursor and solution stirring rate play essential roles in quality of the final product (Coskun et al. 2011).

2.1.6.1 Reaction temperature

The reaction temperature should be high enough for ethylene glycol to convert into glycolaldehyde which reduces Ag^+ ions to Ag atoms.

$$2HOCH_2CH_2OH + O_2 \rightarrow 2HOCH_2CHO + 2H_2O \qquad (3)$$

This is possible only if the temperature is above 150 °C and with the aid of oxygen (Coskun et al. 2011). At 110 °C, microns-sized Ag particles are produced instead of the rod or wire structure (Sun et al. 2002b). If the temperature is between 130 °C to 150 °C, the twins start to nucleate and a rod-like shape is formed (De Oliveira et al. 2013). At 170 °C, enough thermal energy is available to produce the multiply twinned particles that grow into nanowires. At higher temperature (190 °C), the thermal energy available for twin formation is excess than the required. So, the nanowires which are formed at the beginning stage grow longer. But short nanowires are also produced in the later stage due to the reduced silver quantity in the reaction solution.

2.1.6.2 PVP/AgNO₃ molar ratio

If the ratio of PVP/AgNO₃ is small, there would be insufficient PVP molecules to passivate the {100} faces of twinned particles. That will lead to the addition of silver atoms to {111} facets, {100} facets and other facets. The micron-sized particles are produced as the result (Coskun et al. 2011). Otherwise, the reaction produces large diameter silver nanowires (Jiu et al. 2009). Both are not desirable. If the ratio is high, the excess PVP molecules will cover {111} faces and block the addition of silver particles. Hence it results in the formation of silver particles (Sun and Xia 2002) or very short silver nanowires. So the optimum molar ratio should be taken to synthesise the nanowires (Sun et al. 2002b). Different shapes such as nanocubes, spheres, nanowires, plates can be produced by changing the PVP/AgNO₃ molar ratio (Wiley et al. 2005).

2.1.6.3 Molecular weight (MW) of PVP

The molecular weight (molecular chain length) of the PVP molecules also influences the growth and yield of the silver nanowires. The earlier works on the synthesis of silver nanowires used PVP (K30) with MW of 40,000-55,000 (Sun et al. 2002b, Gao et al.

2005). Zhu et al. (2011) reported that increasing the MW of PVP would result in a high yield of nanowires without many particles. When the PVP of MW 800,000 was used to synthesis the silver nanowires, the yield of silver nanowires was very high. Also, the length of the silver nanowires increased from 3 µm to 10 µm, due to the chemical adsorption of Ag^+ ions on the chains of the PVP molecules. Zeng et al. (2014) synthesised silver nanowires using PVP with different molecular weights (chain lengths). Only silver nanoparticles and short rods were produced when the PVP of low molecular weight was used. But, the silver nanowires were produced when the molecular weight of the PVP used was more than 40,000. Da Silva et al. (2016) reported that the PVP with MW 1,300,000 yielded high silver nanowires having a diameter of less than 20 nm. As the chain length (molecular weight) of the PVP molecules increases, the interaction of PVP molecules on the {100} facets of silver nanowires becomes stronger. This results in effective passivation of {100} facets to limit the addition of the new silver atoms in the lateral direction.

2.1.6.4 Amount of NaCl

The role of chloride ions on the growth of silver nanowires in the polyol method is discussed earlier. The chloride ions prevent the aggregation of silver particles by forming a buffer phase of AgCl that supplies silver atoms to the reaction in a controlled manner. If the concentration of chloride ions is high, it would produce large AgCl particles (Coskun et al., 2011) or it would etch the twin particle to form silver particles (Wiley et al., 2004). Another result reported that increase in the chloride ions (within the optimum chloride ions concentration range), leads to decrease in the diameter of silver nanowire (Chang et al., 2011).

2.1.6.5 Use of bromide salts

The bromide salts such as NaBr or KBr are used as the electrostatic stabilizers, like NaCl. Similar to Cl^- ions, the Br^- ions react with the silver ions and form the AgBr phase to avoid the formation of silver aggregation. But the use of the Br^- ions reported to yield nanowires with a smaller diameter than that synthesised with Cl^- ions (Zhang et al. 2015). Also, like PVP molecules, the Br^- ions interact more with the {100} facets of the silver nanowires than with the {111} facets. So, the {100} facets are passivated by the

Br$^-$ ions. Due to this passivation of {100} facets against the addition of silver atoms, the silver nanowires with small diameters are produced (Zhang et al. 2018a).

2.1.6.6 Presence of organic solvents and salts

As mentioned earlier, the Br$^-$ ions adsorbed onto the {100} facets of silver limit the addition of silver atoms in the lateral direction. But the Br$^-$ ions desorb from the silver surface due to the high reaction temperature during the synthesis process. Niu et al. (2018) explored benzoin as the reducing agent in the synthesis of silver nanowires. Adding the benzoin and the NaBr helps to bring down the reaction temperature required for the reduction of Ag$^+$ to Ag^0. At this relatively lower temperature, the adsorption of Br$^-$ ions onto the {100} facets of silver surfaces is increased. The increased passivation of {100} faces by the Br$^-$ ions resulted in the growth of silver nanowires with a small diameter.

The addition of ionic liquids, such as tetrapropylammonium chloride, tetrapropylammonium bromide helps to reduce the diameter of silver nanowires (Chang et al. 2014). The mentioned salts are composed of ammonium$^+$ cations and Cl$^-$ and Br$^-$ anions. The halide anions formed AgCl and AgBr phases that controlled the nucleation of silver particles. The ammonium$^+$ cations acted as the size-controllable template for the growth of silver nanowires. Jang et al. (2018) used tetrabutylammonium dichlorobromide salt in place of regular halide salts. The silver nanowires with a diameter of 32 nm were synthesised. It was reported that the diameter of the silver nanowires could be varied by changing the salt concentration or type of the salt used.

2.1.6.7 Solution stirring rate

The stirring during the synthesis ensures that the concentration of Ag$^+$ ions is uniform throughout the solution. If the stirring speed is very slow, the local concentration of Ag$^+$ ions will be high in some regions, leading to the aggregation of silver particles. If the stirring rate is high, it results in thin and short nanowires. Therefore, the stirring should be sufficiently low to ensure the addition of silver atoms onto twinned particles and facilitate the growth of long nanowires (Lee et al. 2012).

2.1.7 Synthesis environment

The silver nanowires were synthesised in a high-pressure environment by the hydrothermal method (Jang et al. 2017). The pressure-controllable autoclave was used to synthesis the silver nanowires. The diameter of the nanowires was reduced with increase in the pressure. The silver nanowires with 15 nm diameter were produced at the pressure of 190 psi. At high pressure, the nucleation rate of silver seed particles increased. This spontaneous nucleation resulted in the formation of small-size silver particles which eventually grew into small diameter nanowires.

Azani and Hassanpour (2019) synthesised the silver nanowires by solvothermal method at a pressure up to 200 psi along with nitrogen gas purging. The synthesised silver nanowires showed a mean diameter of 17 nm. Hence, it is concluded that the synthesis of silver nanowires at high pressure and in an N_2 gas environment would result in small diameter nanowires.

2.1.8 Separation of silver nanowires

The silver product synthesised by the polyol method contains silver nanowires and undesired silver nanoparticles. These particles should be removed along with the PVP molecules and ethylene glycol solvent used for synthesis. The centrifugation technique was used to separate the silver nanowires from particles and wash away the PVP and ethylene glycol. The synthesised product was first diluted with acetone (1:5 to acetone). Then the diluted solution was centrifuged at 2000 rpm for 20 min (Sun and Xia 2002). The supernatant contains particles and other chemicals which was removed. Then obtained sediment/precipitate was washed with isopropyl alcohol (IPA) by centrifugation process, like in the previous step. This washing was repeated further for three more cycles. Finally, the purified silver nanowires was dispersed in isopropyl alcohol to fabricate the transparent conductive films (De et al. 2009).

2.1.9 Preparation of silver nanowire films

2.1.9.1 Drop casting

The drop-casting is a simple technique to produce the silver nanowires transparent conductive film. The known concentration of a solution with silver nanowires was taken in a pipette and dropped onto a glass or any flexible substrate (Tokuno et al. 2011). The patterned coating was made by taping a patterned polyimide tape on the substrate and dropping the nanowire solution. The patterned silver nanowires films could be obtained by removing the polymer tape (Amjadi et al. 2014).

2.1.9.2 Meyer rod method

The transparent conductive silver nanowires electrode film was prepared by Hu et al. (2010) using the Meyer rod coating method. A few drops of silver nanowires solution were dropped on to the substrate and the rod was rolled over to spread the nanowires solution uniformly on the substrate. The film thickness of 4-60 µm was prepared by changing the concentration of the solution. Zhu et al. (2013) prepared the silver nanowires transparent conductive electrode by using Meyer rod method. During the coating, the substrate was kept on a hot plate of 92 °C to evaporate the solvent from the solution immediately.

2.1.9.3 Vacuum filtration

De et al. (2009) prepared silver nanowires film by vacuum filtering the silver nanowires solution using the cellulose ester membrane. The deposited nanowires on the membrane were transferred to polyethylene terephthalate (PET) substrate by heating and pressing. The PET substrate was placed on a hot plate kept at 100 °C. The membrane was placed on PET to make contact and a 3 kg weight was placed over it for 2 hours. Then the membrane was removed by acetone treatment. Lee et al. (2012a) also prepared a flexible silver nanowires film by the same vacuum filtration method but with the Teflon membrane.

2.1.9.4 Spin coating

The silver nanowires films were prepared by adding the drops of the nanowires dispersion on the substrate fixed on a rotating disk. At higher speed, the solution spread out more to produce the less dense and more transparent film. At a lower speed, a denser and less transparent film is produced. Spechler and Arnold (2012) prepared the silver nanowires film by spin coating by adding nanowires dispersion till the transparency of the film became 65%.

Nam et al. (2014) fabricated the flexible transparent conductive films by spin coating silver nanowires dispersion on glass and Si substrate for 40 sec. Different films were prepared by changing the spin speed between 600-3000 rpm. Then, the obtained silver nanowires films were annealed at 100 °C for 5 min. A commercial ultraviolet curable polymer, 'Norland Optical Adhesive (NOA) 63' was spin-coated on the prepared silver nanowires film and cured by UV irradiation. Finally, the Ag NWs/NOA 63 film was peeled off from the glass substrate to get flexible Ag NWs film. Hwang et al. (2015) used poly-dimethylsiloxane (PDMS) instead of NOA 63 to obtain the flexible Ag NWs film.

2.1.9.5 Spray coating

The spray coating is another technique to fabricate the silver nanowires films. The Ag NWs dispersion is sprayed on the substrate using the commercial air-brush spray gun (commercial air-brush) with an air compressor. Yang et al. (2011) used this spray-coating method to prepare the transparent conductive Ag NWs film. The pre-treated PET substrate was taped on a large glass plate kept on a hot plate at 130 °C. Then the film was held between two aluminium plates and pressed. Choi et al. (2013), Abel et al. (2014) and Coskun et al. (2013) had used this spray-coating method to fabricate the Ag NWs film but with hot plate temperatures of 60 °C, 130 °C and 150 °C, respectively.

2.1.10 Post-film treatment

There are a few problems associated with the silver nanowires films fabricated by any one of the above coating methods. As the silver nanowires are randomly arranged on the substrate, the surface roughness of the Ag NWs would be considerably high to cause

short-circuit by penetrating the thin layer of solution-processed polymer blends atop the Ag NWs electrode (Lee et al. 2008). Hu et al. (2010) reported that the mechanical pressing of the Ag NWs film after the coating decreased the surface roughness.

The capping agent (PVP) used to synthesis the silver nanowires remains as a layer around the nanowires. Tokuno et al. (2011) conducted an experiment on the effect of the PVP layer on the electrical resistance of silver nanowires film. The sheet resistance of 6.9×10^6 Ω/sq was observed in the as-prepared film. So, the PVP molecules present on the silver nanowires need to be removed to obtain a good conductive silver nanowires film. Lee et al. (2008) experimented with comparing the sheet resistance of silver grid film and silver nanowires film. They found out that the silver nanowires film showed higher sheet resistance than the silver grid. The resistance at the nanowires junction was the reason for this higher resistance. Annealing the silver nanowires film helps to remove the PVP molecules present in the film and decreases the junction resistance by fusing the nanowires at the junctions. The heat-treatment of silver nanowires film at 200 °C for 20 min removed the PVP molecules from the silver nanowires and fused the nanowires junction to decrease the sheet resistance of the silver nanowires film (Tokuno et al. 2011).

2.1.11 Properties of silver nanowire electrodes

2.1.11.1 Electrical properties

The electrical resistance of the silver nanowires network is higher than the bulk silver due to the surface scattering of electons. Bid et al. (2006) studied and reasoned this phenomenon. If the diameter of the nanowire is close to or below the mean free path of electrons in bulk material, the effect of electron scattering increases the resistance of the individual nanowires. The length of the nanowires also contributes to the electrical properties of the silver nanowires film.

Short nanowires with large diameter

Low transparent & high resistance

Long nanowires with small diameter

High transparent & low resistance

R_{NW-NW}
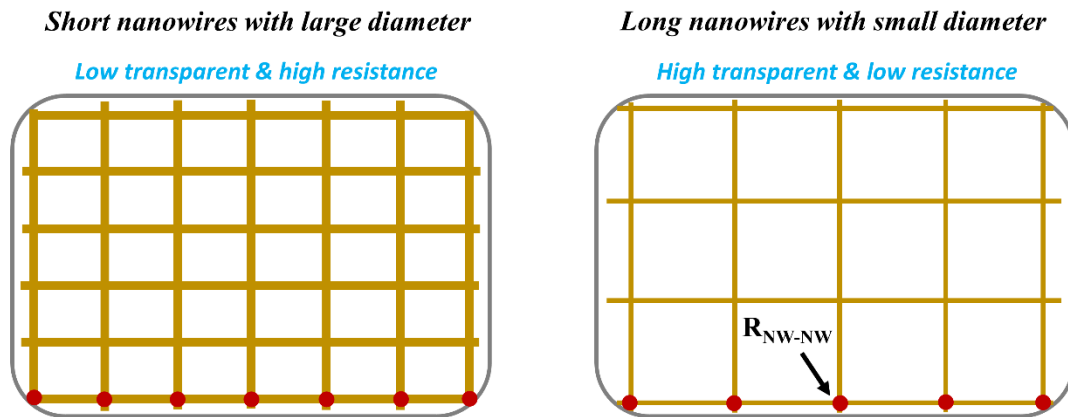
Figure 2.4 Effect of length and diameter of silver nanowires on the sheet resistance and transparency of the film

Hecht et al. (2006) explained this with carbon nanotubes but it can also be applied to silver nanowires network. In this model, it was explained that with longer nanowires, the conductive path (percolation path) is achieved with minimum number of nanowires. This decreases the nanowires junctions and thus lowers the sheet resistance of the film.

2.1.11.2 Electro-optical properties

The density of silver nanowires affects the optical transparency and the sheet resistance of the silver nanowires film. If nanowires density is high, there are more nanowires available to make the path for electrical conductivity. On the other hand, increasing the density of the nanowires will decrease the optical transparency of the film (De et al. 2009). Sonntag et al. (2019) synthesised silver nanowires of different lengths and diameters by varying the molecular weight of the PVP. The transparent conductive silver nanowires films were fabricated by the spray coating method. The silver nanowires film with the optical transparency of 85.5% and sheet resistance of 24.4 Ω/sq was achieved using the silver nanowires with a mean length of 20 μm and mean diameter of 66 nm. Xu et al. (2018) fabricated the silver nanowires films by spin coating. The silver nanowires film showed more than 90% optical transparency and the sheet resistance less than 10 Ω/sq. The high transparency and low sheet resistance were achieved due to the longer silver nanowires and cold-welding at the nanowires junctions.

2.1.11.3 Thermal properties

Thermal annealing is vital to improve the electrical properties of silver nanowires films. It helps to decrease the sheet resistance of the film. This annealing process removes unwanted excess material, such as PVP polymer molecules from the surface of the nanowires. Also, it induces local welding at the nanowires junctions which further decreases the sheet resistance of the film. Although the thermal annealing process improves the electrical conductivity, the silver nanowires film starts to fail when the annealing temperature is increased above 300 °C. When the annealing temperature exceeds the thermal limit, the silver nanowires becomes unstable. This is called as Plateau-Rayleigh instability (Langley et al. 2013). The nanowires break into the small spheres-like structure, thus causing the failure of the nanowires network (Langley et al. 2014). This phenomenon is called as spheroidisation.

2.1.11.4 Mechanical properties

As silver nanowire is made up of metal, it will show excellent mechanical properties such as compression, tension or torsion strength. Langley et al. (2013) compared the sheet resistance of Ag NWs film, ITO and FTO after the bending test to test the mechanical stability. The increase in the sheet resistance of ITO and FTO films was much larger than that of the silver nanowires film. Kang et al. (2013) reported the change in sheet resistance against the bending angle for Ag NWs and ITO films. The sheet resistance of ITO film increased significantly when the bending radius was reduced to 15 mm. But, the sheet resistance of Ag NWs film was not changed up to a bending angle of 5 mm.

Critical review on transparent conductive silver nanowires film

The silver nanowires are conventionally synthesised by the polyol method using silver nitrate as the silver precursor, PVP (MW=40,000-55,000) as the capping agent and NaCl as the electrostabilizer to promote the one-directional growth. The silver nanowires transparent conductive electrode (TCE) is fabricated by spray coating or spin coating or vacuum filtration methods using the synthesised silver nanowires. The transparent conductive silver nanowires film having the optical transparency of more

than 90% and sheet resistance of less than 10 Ω/sq are achieved. The optical
transparency and the sheet resistance could be tailored by changing the dimensions of
the nanowires and the coating parameters. The diameter of the nanowires could be
reduced by the addition of Br⁻ ions, use of high molecular weight PVP, optimising the
PVP/AgNO₃ ratio and high-pressure synthesis environment. The length of the
nanowires is often affected by the atomic oxygens adsorbed on the surface of the silver
seed particles. The ions of iron, copper and chromium are explored as the oxygen
scangers to remove the oxygen from the surface of the seed particles to enhance the
length of the silver nanowires. But the diameter of the silver nanowires is large when
the iron or copper ions are used during the synthesis.

2.2 Review on the Zn/ZnO Anode Materials

The rechargeability and recyclability of the Zn/ZnO anode could be improved by
controlling the dissolution of anode in the alkaline electrolyte, suppressing the
hydrogen evolution and enhancing the charge transfer between electrode and
electrolyte. The efforts are made to improve its electrochemical performance by tuning
the morphology of Zn/ZnO anode and adding external additives with the Zn/ZnO anode
material

2.2.1 Improvements in Zn/ZnO morphology

2.2.1.1 Layered double hydroxides (LDH)

The layered double hydroxides (LDH) are stacked with cationic metal hydroxide layers
with anions in the interlayers as the charge neutralizers. There are notable advantages,
like feasibility of intercalating the structure with different anions, accommodating
divalent and trivalent cations into LDH. These advantages make them as attractive
materials to use for energy storage applications (Vialat et al. 2015). Fan et al. (2013)
developed ZnAl-hydrotalcite LDHs by coprecipitation method as an anode material for
the Zn-Ni alkaline battery. The ZnAl-hydrotalcite showed better electrochemical
activity in terms of cyclic stability and reversibility compared to the Zn powders. It was
attributed to the lamellar structure and aluminium ions. The aluminium played a key
role in restricting dendrite growth by aiding in zinc nucleation during the deposition

process. However, the Zn/Al-LDH based anode performance was limited by their low conductivity that affects electron transportation.

Additives like carbon nanotubes (CNTs) (Yang and Yang 2013), silver nanoparticles (Yang et al. 2014b) and two-dimensional graphene sheets (Long et al. 2017a) were used with Zn/Al-LDHs to improve its conductivity and to facilitate the electron transportation. The enhanced electronic conductivity achieved by the conductive additives resulted in better charge-discharge performance with good cycle stability.

2.2.1.2 Nanorods

Yuan et al. (2005) synthesised ZnO nanorods and ZnO nanoparticles with prism shape by using the chemical vapor deposition process. These synthesised materials were used as the anode for the Zn-Ni battery to study the effect of ZnO morphology on its electrochemical performance. The study revealed that the nanorods are more stable than nanoparticles with prismatic morphology. The nanoparticles become compact after long charge-discharge cycles that reduced their electrochemical activity.

Ullah et al. (2013) studied the solubility of the ZnO in the alkaline electrolyte with microparticles and one-dimensional rods (length >5 µm, diameter =450 nm). The one-dimensional ZnO rod showed better stability in 6 M KOH solution than the ZnO microparticles. The dissolution of material at edges and corners were avoided in the case of ZnO rods that resulted in low solubility of ZnO. Also, the ZnO rods with 450 nm diameter offered more surface area than the microparticles. The surface area and low solubility of the ZnO anode resulted in improved capacity and longer cycles.

Kwak et al. (2017) reported the performance of hexagonal ZnO microrods (diameter = 5 µm, length = 15 µm) in LiOH, NaOH and KOH electrolytes. The electrochemical activity of the ZnO microrods determined from the cyclic voltammetry was high with the KOH electrolyte. The voltage difference between the charge and the discharge process was narrow which indicates the low voltage loss.

2.2.1.3 Nanoflakes and nanoplates

Ma et al. (2008) synthesised ZnO of plate-like morphology by following hydrothermal method. The synthesised ZnO nanoplates were 200 nm to 500 nm in width and 50 nm of thickness. The ZnO nanoplates and conventional ZnO with hexagonal prism morphology were used as the anode material in the Zn-Ni battery. The ZnO plate-like structure converted into a spindle-like structure with a smooth tip after 67 cycles of charge-discharge. But, the conventional ZnO with hexagonal prism structure changed to a sharp-tipped dendritic structure after 67 cycles.

Im et al. (2016) studied the electrochemical performance of ZnO with nanoplate (L=300nm, W=250 nm, t=50 nm), nanobead (L=500 nm), nanorods (L=500 nm) morphology and compared their performance with ZnO cubic morphology. The cyclic voltammetry study revealed that the electrochemical activity of nanoplates and nanorods was higher than that of the nanobeads and conventional cubic particles. The charge-discharge results of the fabricated Zn-Ni battery showed that nanoplates and nanorods possess high capacity retention. After 30 cycles, the nanoplate structures changed into cotton ball structures. The ZnO nanorod morphology changed into small needle-like structures, whereas ZnO nanobeads and ZnO cubes were grown into a dendrite structure.

Yan et al. (2018) used ZnO nanoplate synthesised on the graphene sheets as the anode. This ZnO/graphene showed low electrochemical resistance, excellent charge transfer and uniform deposition during the charging process. These factors helped to reduce the growth of dendrite and shape change that eventually resulted in high capacity and good cyclic stability compared to the commercial ZnO anode. The graphene acted as the platform for effective charge transfer in the anode. The as-assembled flexible Ni-Zn secondary battery retained 86% of the initial capacity of 400 charge-discharge cycles.

Liu et al. (2019) fabricated a Zn-Ni alkaline microbattery with electrodeposited Zn nanosheets as the anode. The battery performance was compared to that prepared with the Zn foil anode. The Zn nanosheet offered more surface area than the Zn foil. The nanosheets with uniform size minimized the polarization and dispersed the electric

field. The battery with Zn nanosheet exhibited high energy density, high reversibility and extended cyclic stability due to the suppressed dendrite growth.

2.2.1.4 Porous foams and sponges

Parker et al. (2014) developed a 3D Zn sponge as the anode material for the Ag-Zn primary battery. This 3D sponge is a monolithic interconnected, continuous Zn. This ensures the long-range electronic conductivity in the anode, uniform current distribution all around the sponge, maintaining the shape/morphology of the electrode in the alkaline electrolyte by restraining the zincate ions into ZnO within an enclosed void-elements inside the porous electrode. In the case of Zn powders, the interconnectivity between the particles was lost during the discharge process. But the 3D sponge maintained its structure throughout the discharge process, thus preventing the growth of dendrites. The sponge Zn anode achieved utilization of 90% (728 mAh g^{-1}) during discharging in a primary Zn-air cell.

A hyper-dendrite nanoporous zinc foam was electrochemically synthesised by Chamoun et al. (2015). It was formed by a three-dimensional network of dendrites that were electrochemically active and electronically conductive at the nanoscale. The Zn foam had a conductive internal structure that caused uniform current distribution. Also, it showed to reduce the concentration gradients and polarization loss at the anode. This zinc foam showed excellent Coulombic efficiency (87.7± 1.5%) and 100 cycles of rechargeability. The excellent performance of this Zn foam is attributed to the 3D nanoscale dendritic network and its large surface area. Davies et al. (2016) demonstrated enhanced utilization of the hyper dendrite porous Zn anode by optimizing the electrolyte concentration and different electrolyte additives. It was reported that increasing the concentration of KOH electrolyte would improve the utilization of the anode. The additives such as potassium citrate or potassium chloride showed a considerable increase in Zn anode utilization.

Wang et al. (2020) fabricated a Zn-Ni battery with the monolithic nanoporous Zn prepared by reduction-induced decomposition process, as the anode material. This nanoporous Zn anode was continuous, electronically conductive, stable in the alkaline electrolyte with high surface area and offered more charge transfer sites. During the

charge-discharge cycle, the anode undergoes coarsening controlled by surface diffusion. This coarsening helped to maintain the continuous zinc phase that resulted in its uniform reaction. That helped in preventing the progress of dendrite growth.

2.2.1.5 Microspheres

Zhao et al. (2015) studied the ZnO microspheres (10-20 µm) as the anode material for the Zn-Ni battery and compared its performance with the conventional ZnO with prism morphology. The dense, compact and spherical ZnO microspheres showed good resistance against corrosion and shape change. Also, the reversibility of the ZnO microsphere anode was better than that of the conventional ZnO. The ZnO microsphere anode was activated before the charge-discharge process. The morphology of microspheres was changed into nanometer scaled ZnO rods due to the dissolution process. This reduction in particle size increased the surface area that resulted in the high electrochemical activity of the ZnO anode. After 50 cycles, it is observed that the size of the particles increased and the shape changed into a block structure.

2.2.2 Additives

The carbon based and the metal oxide based additives are used with the Zn/ZnO anode to prevent the dissolution of active zincate ions into the electrolyte, suppressing the hydrogen evolution reaction (HER) and enhancing the conductivity of the anode to improve the discharge capacity and life cycle of the battery.

2.2.2.1 Carbon based additives

Graphene

Ozgit et al. (2014) studied the effect of graphene sheets as an additive to the Zn anode to improve its electrochemical performance. The Zn nanoparticles (size< 50 nm) were mixed with the reduced graphene oxide (rGO) and a PTFE binder was used as the anode in a Zn-Ag battery. The added rGO improved the conductivity for charge transfer, offered a large surface area for enhanced electrode-electrolyte interaction and suppressed the dendrite formation. These factors, in turn, resulted in the increased electrochemical activity of the anode, high capacity and longer charge-discharge cycles.

Besides, the restacking issue associated with the rGO sheets was prevented by the Zn nanoparticles.

Yan et al. (2018b) reported a lasagna-inspired Zn anode, in which ZnO nanoparticles of 100 nm size were wrapped by the graphene oxide (GO) sheets. The dispersion of ZnO nanoparticles, GO and binder was cast on a polyethylene terephthalate (PET) film. Upon drying, the free-standing ZnO film was peeled off the PET. The free-standing ZnO was used as the anode material. The GO encapsulated the ZnO and it allowed only OH^- ions and water to diffuse through and blocked the larger $Zn(OH)_4^{-2}$ ions that prevented the active material loss. The presence of GO in the alkaline electrolyte reduced the GO and it helped to facilitate electron transportation. Also, the GO-ZnO lasagna structure exhibited less dissolution in the alkaline electrolyte solution than the commercial ZnO. The fabricated Zn-Ni battery cells showed long charge-discharge cycles maintaining the capacity of 565 Ah kg^{-1} for 150 cycles. The morphology of GO/ZnO lasagna anode remained unchanged even after the 150 cycles whereas the morphology of commercial ZnO particles changed entirely after 40 cycles.

Carbon nanotubes

The carbon nanotubes (CNTs) are also used as an additive to the Zn anode, like graphene sheets, to enhance the electronic conductivity of the anode. Yang and Yang (2013) prepared the composite of CNT and Zn-Al layer double hydroxide (LDH). They used it as an anode to fabricate the Zn-Ni battery. As the LDH structure gave good structural stability and controlled solubility of Zn, CNTs enhanced the electronic conductivity of the Zn-Al-LDH nanocomposite. The average discharge capacity increased as a result of improved electron transportation in the anode. The battery retained 95% of its capacity even after 200 cycles.

Cui et al. (2019) synthesised ZnO/CNT composite by the chemical filling method to use it as an anode for the Zn-Ni battery. The inner part of single-walled CNTs was filled with the ZnO nanoparticles. The electrode was prepared by adding the prepared ZnO/CNT composite with PTFE as a binder. It is reported that the contact area between CNTs and ZnO is high in this case compared to physically mixed ZnO and CNTs. It is also noted that the charge/discharge performance of the chemically filled ZnO/CNT showed poor performance at the beginning due to the low interaction of active material

with the electrolyte. The performance of ZnO/CNT composite surpassed the physically mixed ZnO and CNT anode as the number of cycle increases.

Conductive carbon

Huang and Yang (2014) encapsulated the ZnO sheet-like structures with the amorphous carbon layer (thickness= 4 nm) to obtain a cellular-like structure. This cellular-like carbon-coated ZnO was used as an anode for the Zn-Ni secondary battery. The carbon coating on the ZnO enhanced the conductivity and reduced the internal resistance of the anode. The carbon-coated ZnO exhibited a lower charging voltage plateau compared to the bare ZnO. This low charging voltage would result in improved charging efficiency. On the other hand, the discharge voltage plateau of bare ZnO dropped rapidly whereas the discharge voltage remained stable for the carbon-coated ZnO. The limited dissolution of active zincate ions due to the carbon coating prolonged the discharge duration. It is reported that the discharge capacity of the carbon-coated ZnO took 25 charge-discharge cycles to reach its highest capacity. But after 16 cycles, its discharge capacity surpassed that of the bare ZnO. As the electrolyte took more time to impregnate the carbon coating, the initial capacity was less. The carbon coating suppressed the dendrite formation by preventing the dissolution of zincate ions into the electrolyte.

Chen et al. (2018) prepared a novel ZnO anode with a pomegranate structure (6 µm). This pomegranate ZnO was prepared via a bottom-up microemulsion approach. The ZnO nanoparticles are encapsulated by the microporous carbon framework to assemble those as secondary clusters. The small ZnO nanoparticles avoided the passivation problem since their size is much smaller than the critical passivation thickness. The microporous carbon prevented the dissolution of zincate ions into the electrolyte while allowing OH^- and water molecules to take part in the reactions. This eventually led to a high specific capacity of the anode for a longer cycle. By controlling the solubility of zincate ions, the formation of dendrite was suppressed. But it is noted that the charging voltage for pomegranate ZnO anode kept increasing for the consequent cycles. This was due to the hydrogen evolution reaction (HER) resulting from the reduction reaction of water during the charging process.

Long et al. (2017b) coated a carbon layer over sheet-like Zn-Al-Bi layered double oxide to improve the electronic conductivity. Similarly, carbon-coated Zn foil (Li et al. 2018), ZnO nanoparticles coated with carbon (Peng et al. 2019), Zn@C core-shell nanocomposite (Wei et al. 2019) and ZnO coated with nitrogen-doped carbon (Zeng et al. 2020a) are reported as the anode material. The purpose of this carbon coating over Zn/ZnO anode materials in the above reports is to 1) improve the conductivity, 2) discharge capacity, 3) preventing the dissolution of zincate ions, 4) suppress the shape change of the anode.

2.2.2.2 Metal/Metal oxide additives

Aluminum

The effect of aluminum oxide (Al_2O_3) as an additive to the Zn anode was evaluated by Lee et al. (2013). A layer of Al_2O_3 was coated over the Zn powders (52 µm) by chemical solution process. This Al_2O_3-Zn powder was used as the anode to fabricate a Zn-air alkaline battery. It was reported that Al_2O_3 suppressed the hydrogen evolution due to its high overpotential for hydrogen evolution. Also, the Al_2O_3 acted as a protection layer to prevent the Zn dissolution into the KOH electrolyte and it improved the corrosion resistance of the anode. Since the loss of Zn was minimized, the battery with Al_2O_3-Zn anode showed a longer discharging time than the one used by bare Zn powder. The self-discharge of the battery was reduced with the Al_2O_3-Zn anode as the side reaction from H_2 evolution was inhibited.

Bismuth

The influence of additives, such as Bi_2O_3, LiOH, CdO, SnO, $Ni(OH)_2$, $Co(OH)_2$ and alkaline earth oxides on the electrochemical performance of Zn and ZnO in the KOH electrolyte was studied by Renuka et al. (2001). The study was conducted by mixing the additives with the ZnO powder. The PTFE was used as the binder to prepare the ZnO working electrode. The Bi_2O_3 showed excellent results as it enhanced the current densities from anodic and cathodic reactions. The CdO and SnO also demonstrated an excellent performance to improve the electrochemical activity of the ZnO.

Yuan et al. (2009) modified the surface of the commercial ZnO powder with Bi_2O_3 coating by chemical solution method. The prepared Bi_2O_3-ZnO was used as the anode

for the Zn-Ni battery. The study reported that the surface-modified Bi_2O_3-ZnO showed stable discharge capacity for longer cycles than the bare ZnO. During the initial charging process, the Bi_2O_3 undergoes an irreversible reduction reaction and became metallic Bi. This metallic Bi on the ZnO particles improved the electronic conductivity of the anode. Also, the dissolution problem of zincate ions into the electrolyte was minimized due to the passivation of ZnO by this metallic Bi layer. The improved conductivity for electron transfer and reduction of active ZnO loss attributed to high discharge capacity and longer charge-discharge cycles of the Bi_2O_3-ZnO anode.

Moser et al. (2013) investigated the role of Bi_2O_3 as an additive to the ZnO with the help of in-situ X-ray diffraction measurement during charging and discharging processes. The ZnO anodes with and without Bi_2O_3 were prepared to fabricate the Zn-Ni battery. During charging, the intensity of ZnO XRD peaks was reduced to Zero. Simultaneously, the Zn peak was emerged and kept increasing. That showed the reduction reaction of ZnO into Zn which is attributed to the charging process. It is noted that the intensity of the Bi_2O_3 peak was reduced and the emergence of the metallic Bi peak was observed at the first charge. The conversion of Bi_2O_3 into metallic bismuth led to an electronically conductive network at the nanometer scale in the anode. This enhanced the electron transportation and prevented the dissolution of zincate ions that resulted in better discharge stability for more than 50 cycles.

It is reported that the addition of Bi_2O_3 does not only increase the conductivity but also influences the precipitation of zincate ions into ZnO to make it rechargeable (Shin et al. 2016). When the Zn undergoes oxidation reaction during discharging, the Zn is converted into zincate ions. These zincate ions are deposited on the surface of Bi species. Subsequently, these zincate ions are precipitated as ZnO on the surface of Bi species. The electrical contact with the ZnO was maintained due to the deposition of ZnO on the bismuth species. It makes ZnO more rechargeable for long cycles.

Many works are reported with Bi_2O_3 as an additive material to improve the performance of the Zn/ZnO anode based alkaline batteries due to the advantages like improved electronic conductivity in the anode, prevention of active material (Yang et al. 2018) (Schmid and Willert-Porada 2018), etc.

But, the major drawback is heavy molecular weight of Bi_2O_3 compared to In_2O_3 and SnO_2. The addition of Bi_2O_3 increases the weight of the anode (Shin et al. 2016).

Indium

Indium in the form of In_2O_3 is used as the additive to Zn/ZnO anode to improve the electronic conductivity and to prevent anode dissolution into the electrolyte (Ma et al. 2007). Also, the addition of indium suppressed the hydrogen evolution due to its high overpotential for hydrogen evolution. Wang and Yang (2013) incorporated indium into Zn–Al layered double hydroxides (LDHs) to solve the low conductivity of LDHs problem. Like bismuth, the $In(OH)_3$ in Zn-Al-In LDH was reduced to indium metal that cannot be oxidized back due to the discharge cut-off voltage. The metallic indium formed the conductive network in the anode to facilitate electron transfer. The indium network also acted as the protective layer to minimize the dissolution of zincate ions into the electrolyte. The parasitic reaction of undesired hydrogen evolution was also suppressed due to the high hydrogen overpotential of the indium. All these benefits of indium addition led to higher discharge capacity, better stable discharge and long battery life than the Zn–Al-LDHs without indium.

Synthetic Zn-In alloy prepared by fusion of zinc and indium metal powders (0.5% and 1% In) and its electrochemical performance in the KOH electrolyte was studied with a three-electrode setup (Elrouby et al. 2021). The study concluded that the alloying In with Zn resulted in enhanced conductivity, suppressing hydrogen evolution, improved corrosion resistance and longer discharge time. The high cost of indium due to its scarcity would limit its commercial application.

Silver

The silver metal, which has high electronic conductivity, is another potential additive for the ZnO anode for alkaline battery application. Yang et al. (2014a) explored the performance of silver as an additive to the Zn-Al LDH nanosheets for a Zn-Ni battery. The surface of the Zn-Al LDH nanosheets was decorated with the silver nanoparticles. The fabricated battery exhibited high discharge capacity and good cyclic reversibility that resulted from the improved charge transfer due to the addition of silver nanoparticles. Other studies are reported using the silver as an additive to the flower-

like ZnO (Zeng et al. 2020b) and ZnO microspheres (Rong et al. 2020) to improve the electrochemical performance of the ZnO anode for the alkaline battery application.

Tin

Tin is another potential additive to the ZnO anode in alkaline batteries due to its high overpotential for hydrogen evolution (Zheng et al. 2019) and good electronic conductivity. Zhang et al. (2014) investigated the effect of SnO_2 on the electrochemical performance of ZnO anode in the Zn-Ni battery. The composite of ZnO/SnO_2 synthesised by the hydrothermal method was used as the anode. Similar to Bi_2O_3 and In_2O_3, the SnO_2 is reduced to tin metal during the first charging process. The metallic tin formed a conductive network in the anode that resulted in better electronic conductivity. This improved conductivity decreased the charge-transfer resistance between the anode and the electrolyte. It was reported that the dissolution of ZnO was reduced due to the passivation layer formed by the tin over the ZnO surface. The hydrogen evolution was also suppressed due to the high hydrogen overpotential of tin species. The corrosion resistance of the anode was improved which is attributed to the suppression of hydrogen evolution. The discharge capacity and reversibility of the anode were enhanced by the enhanced charge-transfer between the anode and the electrolyte.

Feng et al. (2014) prepared Zn-Sn-Al LDHs as an additive to the ZnO anode. The ZnO anode was prepared by physical mixing of ZnO, Zn-Sn-Al LDHs and PTFE binder to fabricate the Zn-Ni battery. The presence of tin with Zn-Al LDHs made it an excellent additive to the ZnO. The effect was observed by the increased discharge capacity and good capacity retention for longer cycles.

Titanium

Zhang et al. (2018b) fabricated the Zn-Ni alkaline battery. ZnO was used in the form of nanorods synthesised on the conductive carbon paper. These ZnO nanorods were again coated with a thin layer of TiN by atomic layer deposition (ALD). After exposing to air, TiN was converted into TiN_xO_y. It was reported that the rod morphology of ZnO reduced the dissolution of ZnO into the alkaline electrolyte. In addition to that, the passivation of zinc anode by irreversible ZnO was avoided by using ZnO in the

nanometer size scale (<500 nm). The protection layer of TiN_xO_y allowed the charge transfer between the ZnO and the electrolyte but prevented the direct contact of ZnO with the electrolyte. That minimized the dissolution of ZnO into the electrolyte.

Zhao et al. (2018) coated Zn plate with TiO_2 by ALD technique. This TiO_2 served as the protection layer to the Zn plate to avoid direct interaction with the electrolyte. Thus, the loss of active zincate species from the Zn plate into the electrolyte was prevented. The coating of TiO_2 reduced the corrosion of Zn and suppressed the hydrogen evolution due to the high overpotential of Ti. The Zn-Mn battery fabricated with this Zn/TiO_2 anode maintained 85% capacity retention over 1000 cycles.

Critical review on Zn/ZnO anode

Among the various morphologies of ZnO, the nanorods, LDHs and spherical structures showed good stability in the alkaline electrolyte. The nanorods would have a larger surface area than the spherical structures. Also, the ZnO nanorods can be synthesised by following a simple hydrothermal method.

Carbon-based additives, such as graphene, CNTs and conductive carbon showed excellent results in enhancing the conductivity of the anode for easy charge transportation. But the issue of hydrogen evolution reaction (HER) cannot be answered by these carbon-based additives. The bismuth improved the conductivity and stability of the Zn/ZnO anode. But the specific capacity of the battery would decrease owing to its weight. The indium-based additives are the other alternative to bismuth. The low abundance of indium would increase the cost of the battery. The SnO_2 would be a better additive than Bi, In, Ag and Ti based additives due to its low cost and good electrochemical properties such as suppressing hydrogen evolution and good electronic conductivity.

2.3 Review on Tin Oxide for Energy Storage Applications

Tin oxide (SnO_2) is an n-type semiconductor material with a bandgap of 3.6 eV. The SnO_2 is used in various applications such as electronics, photocatalysis, batteries and gas sensors due to its chemical and physical properties.

2.3.1 Applications

2.3.1.1 Electronics

The tin oxide (SnO_2) has high conductivity, high optical transparency and high mobility (Bansal et al. 2012). The SnO_2 films are used as the transparent conductive oxide (TCO) in electrochromic devices (Kim et al. 2018). The introduction of dopant materials such as fluorine, niobium increases the electronic properties of the SnO_2 (Kim et al. 2018) (Ramarajan 2019). The fluorine-doped tin oxide (FTO) is the second widely used TCO material next to ITO due to its excellent electronic and optical properties (Kim et al. 2018).

2.3.1.2 Photocatalysis

The water pollution caused by the dying industry is mainly due to the release of toxic organic dyes into the water. The polluted water is treated by photocatalytic degradation of such toxic dyes by converting or degrading into non-toxic molecules. Because of the strong oxidizing ability, low toxicity, high chemical stability and insolubility, the SnO_2 is an ideal material for water treatment by photocatalysis (Al-Hamdi et al. 2017).

When a semiconductor material is excited by the incident electromagnetic radiation (ex: visible light), the e^- and h^+ pairs formed (Al-Hamdi et al. 2017). The electron-hole pairs can be created in SnO_2 by ultraviolet (UV) light due to its bandgap value of 3.6 eV. When UV light is illuminated, the organic dyes are converted into CO_2 and H_2O by the hydroperoxyl radicals produced by the electron-hole (e^- and h^+) pair. The pure and doped SnO_2 nanoparticles or nanostructures are proved to degrade toxic pollutants such as methylene blue (Sadeghzadeh-Attar 2018), Remazol Yellow (Akti 2018), Eriochrome Black T and 2-chlorophenol (Najjar et al. 2020).

2.3.1.3 Gas sensors

Metal oxides are promising materials for gas sensor applications because of their high-affinity to gases such as CO and H_2 (Al-Hamdi et al. 2017). The gas sensors are working by measuring the change in electrical characteristics of the active material caused by the adsorbed analyte gas. Due to the non-toxic nature, high chemical stability and high

conductivity, the SnO_2 is studied as a gas sensor material. But, the SnO_2 can detect the gases at high-temperature conditions only (> 200 °C) (Ingole et al. 2017). However, by engineering the grain-size, electronic structure and doping the appropriate materials, the gas sensing performance is increased while reducing the requirement operating temperature. The ultra-fine grained SnO_2 nanospike structures showed excellent gas sensing performance to ethanol, methanol, CO and methane (Xu et al. 2011). Also, the SnO_2 based gas sensors are being prepared to detect the gases, such as NO_2, H_2, SO_2 and CO_2 (Liu et al. 2016) (Zhang et al. 2017) (Manikandan et al. 2020).

2.3.1.4 Batteries

Graphite is the widely used anode material in commercial lithium-ion batteries because of its low cost and long life (Rothermel et al. 2016). Due to its low theoretical specific capacity of 370 mAh g^{-1}, recent researches are focussed on the alternative material with a higher specific capacity (Chen et al. 2014). The SnO_2 is a potential anode material due to its higher theoretical specific capacity of 781 mAh g^{-1} (Courtney and Dahn 1997). When SnO_2 is used as the anode in a Li-ion battery, the lithium ions intercalate in the SnO_2 structures during charging. In this process, the SnO_2 is irreversibly converted into Sn metal. This issue can be rectified by using the ultra-small SnO_2 nanoparticle or nanostructures (Chen et al. 2014). The anode fabricated using SnO_2 nanotubes exhibited the specific capacity of 1500 mAh g^{-1} at a rate of 0.1 C which is higher than its theoretical capacity (Liu et al. 2014). The mesoporous structure made of ordered SnO_2 nanoparticles (size 9 nm) showed a capacity of 778 mAh g^{-1} at the discharge current density of 0.1 C (Etacheri et al. 2015).

The tin oxide is also used in the zinc alkaline batteries as an additive to the Zn/ZnO anode. The addition of SnO_2 with the anode resulted in suppressing the hydrogen evolution reaction at the anode. The hydrogen evolution overpotential for SnO_2 is higher than that of the ZnO. The electrochemical performance and life of the anode are increased because of the decreased hydrogen evolution reaction by SnO_2 (Zhang et al. 2014).

2.3.2 Instability of tin oxide electrodes

There are some concerns in using SnO_2 as an electrode material for electrochemical energy storage applications. The volume or size expansion of SnO_2 during the charge-discharge (oxidation-reduction) process leads to cracks and discontinuity in the electrode, resulting in reduced capacity and life cycle (Yan et al. 2014). When the SnO_2 is used as the anode in lithium-ion battery, the SnO_2 undergoes a reduction reaction to form metal Sn during the charging process. The reduced metal Sn subsequently forms Li-S alloy with intercalated lithium ions. The dealloying of Li-S alloys happens when the battery discharges. This alloying/dealloying process leads to the size expansion of the SnO_2 anode. This pulverization effect impacts the cyclability of the anode negatively (Lou et al. 2006). Chung et al. (1995) observed the volume expansion of 32% when the Sn metal film was converted to SnO_2 by annealing in air. This volume expansion also affects the electrochemical performance of the supercapacitors fabricated using SnO_2 as the electrode material (Bonu et al. 2016).

2.3.3 Improving the stability of tin oxide

The instability of tin oxide in electrochemical applications is addressed by using suitable supportive material with it. The materials with a large surface area, good conductivity and porosity are the ideal supporting structure to improve the stability of the SnO_2. The composite of SnO_2 and graphene oxides was prepared as the anode material for lithium-ion battery (Birrozzi et al. 2014). The active SnO_2 particles confined by the graphene oxide sheets have less tendency to particle agglomeration and volume expansion. Also, the large surface area offered by the graphene oxide improved the charge transfer between electrode and electrolyte.

A 3D network of porous graphene oxide/SnO_2 nanoparticles composite was prepared as the anode material. The porous SnO_2 is uniformly dispersed on the reduced graphene oxide (rGO) that served as the supportive structure to SnO_2. The prepared anode shows high conductivity, large surface area with many reactive sites and porous structure to accommodate the volume expansion. The anode delivered a specific capacity of 595 mAh g^{-1} after more than 300 charge-discharge cycles (Zhou et al. 2016). A highly conductive N-doped carbon layer was coated over the SnO_2 hollow nanofibers (Pham-

Cong et al. 2017). Because of the synergic effect of SnO_2 hollow structures and the conductive carbon layer, high specific capacity of 1648 mAh g^{-1} was achieved.

Thus, a supporting material with a large surface area and having the ability to facilitate the charge transfer can improve the electrochemical performance of SnO_2 electrode in the electrochemical energy storage applications.

Critical review on tin oxide electrode

Tin oxide (SnO_2) is used in many applications such as water treatment, gas sensors, electronics and batteries due to its low toxicity, chemical stability, good conductivity, and high theoretical capacity. The SnO_2 based electrodes encounter instability problems in electrochemical energy storage applications. The volume expansion and agglomeration of the SnO_2 particles during the electrochemical cycles lead to discontinuity or cracks in the electrode. This eventually leads to the loss of contact between the electrode materials and the substrate, development of mechanical stresses and reduced charge transfer. The instability of the SnO_2 electrode material can be solved by incorporating the SnO_2 on a suitable supportive material having a large surface area with the ability to hold the SnO_2 on its surface to enable the charge transfer between SnO_2 and electrolyte.

2.4 Review on MoS_2 Nanosheets

Atomic layer molybdenum disulfide (MoS_2) comes under the family of two-dimensional materials, like graphene, hexagonal boron nitrate, etc. A MoS_2 sheet has a layer of Mo atoms sandwiched between the layers of S atoms with a strong covalent bond. The adjusting MoS_2 sheets are held together by weak van der Waals forces (Le Mogne 1994). The MoS_2 nanosheets are attractive due to their two-dimensional structure, high surface area (> 210 m^2 g^{-1}), tuneable band gap and electronic properties (Wang et al. 2015). The MoS_2 nanosheets are easily coated over various substrates owing to their two-dimensional structure and mechanical flexibility (Ji et al. 2019). Also, the surface of the MoS_2 nanosheets can be functionalised by using zero-dimensional (0D) and one-dimensional (1D) nanomaterials.

2.4.1 Optoelectronic properties

The stable 2H phase of MoS_2 exhibits semiconductor behaviour (Eda et al. 2011). The bulk MoS_2 has an indirect band gap of 1.2 eV. Its band gap value increases with decrease in the crystal thickness because of the quantum confinement effect. The monolayer MoS_2 shows a direct band gap of 1.9 eV (Eda et al. 2011) (Gupta et al. 2020). The MoS_2 nanosheets continue to attract interest in the field of optoelectronics and photocatalysis due to this indirect to direct and small to large band gap tunability.

2.4.2 Electronic properties

The MoS_2 nanosheets are a promising material for next-generation thin film transistor (TFT) applications. The mono/few layers of MoS_2 nanosheets show high carrier mobility of 100 to 200 cm^2 V^{-1} s^{-1} and a high on/off current ratio of 10^8 which are the essential characteristics for an active material in a transistor (Gupta et al. 2020). Many works are reported on MoS_2 nanosheets based thin film transistors towards the applications like non-volatile rewritable memory devices (Liu et al. 2012) (Liao et al. 2019) (Liao et al. 2020).

2.4.3 Thermal properties

Li et al. (2014) conducted thermogravimetric analysis (TGA) on MoS_2 and MoS_2/ conductive polymer composite to study the thermal degradation behaviour. It showed that MoS_2 was stable up to 600 °C. Zhou et al. (2014) also reported that MoS_2 is thermally stable up to 700 °C. It was once again confirmed from the reported work by Qin et al. (2014).

2.4.4 Mechanical flexibility

The materials should not fail after repeated bending cycles to use in a flexible device application. They should not lose their properties after a certain period of time. The MoS_2 monolayer sheet shows good mechanical properties due to its strong Mo-S covalent bond (Gupta et al. 2020). Bertolazzi et al. (2011) investigated the mechanical properties of MoS_2 sheets. The monolayer and few-layer MoS_2 sheets were deformed and even broken using an atomic force microscope. The Young's modulus of the

monolayer MoS_2 was found to be 270 ± 100 GPa which is higher than stainless steel. Peng and De (2013) used density functional theory (DFT) to investigate mechanical properties, such as ultimate tensile strain and in-plane stiffness. The estimated value of ultimate tensile strain was 0.24-0.37 and in-plane stiffness was 120 N/m. The reported works concluded that the MoS_2 nanosheets are very flexible and can be used on any kind of substrates.

2.4.5 Electrochemical properties

The MoS_2 nanosheets are very good candidate materials to be used for energy storage applications due to the characteristics such as high surface area, planar electronic transportation and good stability (Huang et al. 2014). The hydrothermally synthesised MoS_2 nanosheets and MoS_2 microflowers were tested as the electrode materials for the supercapacitor application. The corresponding specific capacity was measured as 129.2 $F\ g^{-1}$ and 167.7 $F\ g^{-1}$ at the current density of 1 A g^{-1} (Huang et al. 2014) (Xu et al. 2016). These high specific capacity values of the MoS_2 electrodes were due to their high surface area and layered structure that enhanced the interaction between the electrode and the electrolyte. The MoS_2 based hybrids with materials like graphene and polyaniline reported increased specific capacity (Ren et al. 2019) (Hota et al. 2020).

The MoS_2 is a potential anode material for lithium-ion battery applications because of its layered structure that can allow the lithium ions to intercalate into them. As the weak van der Waals force binds the neighbouring MoS_2 layers, the S-S bonds are broken and Li-S bonds are formed by the intercalated lithium ions (Du et al. 2010). The electrochemical performance of the MoS_2 can be improved by incorporating them into a high conductive network. The MoS_2 nanosheets with a carbon layer improved the conductivity that resulted in a high specific capacity of 1001 mAh g^{-1} (Liang et al. 2013). Similarly, different hybrid MoS_2 based anode materials were prepared with various conductive supportive networks such as macro-micro-mesoporous carbon structure (Huang et al. 2019) and 3D porous charcoal network structure (Xu et al. 2019). So, it is clearly understood that the MoS_2 nanosheets are an excellent candidate to be used for electrochemical storage applications.

2.4.6 Electrochemical performance of MoS₂ nanosheets hybrid electrodes

Stability and charge transportation are the essential properties of any material used for electrochemical energy storage applications, such as batteries and supercapacitors. The MoS$_2$ nanosheets are two-dimensional materials with a large surface area like graphene. There are many reports that show the ability of MoS$_2$ nanosheets in enhancing the electrochemical performance of metal oxide and conductive polymers based supercapacitors (Zhao et al. 2017) (Alamro and Ram 2017).

Huang et al. (2013) prepared a composite of polyaniline (PANI)/MoS$_2$ nanosheets for the supercapacitor application. The specific capacitance of PANI was increased by two folds because of added MoS$_2$ nanosheets. The equivalent series resistance (ESR) of PANI was reduced from 2.05 Ω to 1.25 Ω by compositing it with MoS$_2$. The reason for this improvement is believed to be the rapid movement of charge carriers back and forth through the MoS$_2$ nanosheets. Also, MoS$_2$ nanosheets serve as a high surface area support for PANI, which enhanced the interaction between electrode and electrolyte. It facilitated the rapid transport of electrolyte ions to the electrode during the charge-discharge process. Moreover, the composite lost only 2% of its specific capacitance after 500 cycles.

The poor conductivity of the electrode often reduces the capacity and cyclability of metal oxides such as Co$_3$O$_4$ (Liang et al. 2015) and Mn$_3$O$_4$ (Wang et al. 2016a), MnO$_2$ (Zhang et al. 2020b) and NiFe$_2$O$_4$ (Zhao et al. 2017). This could be enhanced by incorporating MoS$_2$ nanosheets with them. The composite of such materials with MoS$_2$ nanosheets showed the enhanced current values in cyclic voltammetry tests. The discharge time was also increased for such composite materials.

2.4.7 Synthesis methods

2.4.7.1 Chemical vapour deposition

The molybdenum (Mo) source material and sulfur source material are kept inside a horizontal tube furnace and heated. Because of the heating, the source materials get evaporated. The Ar gas or N$_2$ gas is purged inside from one end of the tube furnace. The vapours of Mo and sulfur are carried by this gas and get condensed onto the

substrate. A single layer of MoS_2 film is produced from this process. This method is called as chemical vapour deposition (CVD).

Lee et al. (2012b) and Tsai et al. (2014) produced the few layers MoS_2 with MoO_3 and sulfur as source materials. The CVD process was carried out in a tube furnace, kept at 650 °C, under N_2 gas flow. Heating for 15 minutes produced atomic layers of MoS_2 films. Yu et al. (2013a) used $MoCl_5$ powder as Mo source. High quality MoS_2 film was deposited with 10 minutes of heating at 850 °C under Ar gas flow.

2.4.7.2 Mechanical methods

Mechanical exfoliation is another technique to produce high-quality layers of MoS_2 sheets. This technique was used to exfoliate graphene from graphite flakes (Novoselov et al. 2004). In this method, each layer of graphite was peeled off by scotch tape till its thickness was reduced to few graphite layers. This technique was adapted to produce MoS_2 nanosheets. Bertolazzi et al. (2011) exfoliated MoS_2 sheets from the bulk molybdenite. The obtained nanosheets were dissolved and captured on PVA and PMMA coated SiO_2 substrate. Then PVA and PMMA layer were released by dissolving them in water and vacuum heating at 400 °C for 4 hours. In the end, MoS_2 was transferred to SiO_2 substrate. Choi et al. (2012) and Kwon et al. (2015) also used the mechanical exfoliation method to obtain MoS_2 film to fabricate MoS_2 film based transistor.

2.4.7.3 Physical vapour deposition

Le Mogne (1994) prepared MoS_2 films for super-lubrication application. The MoS_2 sputtering target was made from the MoS_2 powder. The films on different substrates were prepared by sputter depositing MoS_2 by using radio-frequency (RF) magnetron sputtering system.

Ma and Shi (2013) placed MoS_2 pellets in a cubic iron box with small pinholes. Then, this box and Si substrate were kept inside a horizontal tube furnace. The furnace was heated to 500 °C and Ar gas was supplied into the furnace at a rate of 10~30 sccm. The MoS_2 got evaporated and came out through the pinholes to form a narrow vapour beam.

The reaction time was varied between 2-10 minutes to produce MoS_2 film on the Si substrate.

Though CVD, PVD and mechanical exfoliation method produces high-quality MoS_2 sheets, it has limitations, namely, the need for high temperature heating, transfer of film onto another substrate and low yield.

2.4.7.4 Lithium intercalation method

The bulk MoS_2 powder was soaked in a lithium based solvent. After allowing sufficient time for lithium to intercalate into the MoS_2 layers, the solution was mixed with water and ultrasonicated. Also, it was assumed that when water and intercalated Li interact, hydrogen gas is produced. The MoS_2 layers are separated as the hydrogen gas expands.

Joensen et al. (1986) exfoliated single-layer MoS_2 from the bulk MoS_2 powder using 1.6 M n-butyl lithium in hexane under Ar gas atmosphere. Eda et al. (2011) heat-treated the MoS_2 sheets which were produced from Li intercalation technique. They annealed the MoS_2 sheets at 300 °C in the Ar atmosphere. This treatment restored 2H semi conductive phase from the bulk powder that is needed for transistor application. Voiry et al. (2013) and Acerce et al. (2015) synthesised 1T phase MoS_2 by Li intercalation method for hydrogen evolution.

Dungey et al. (1998) explained the structural change involved in MoS_2 bulk sheets during Li intercalation. In bulk MoS_2 (2H phase), the sulfur atoms are in a hexagonal close-packed arrangement. The Mo atoms are sandwiched between the S atoms so that Mo will have six coordinated S atoms to form trigonal prismatic geometry. The van der Waals force holds the sandwiched layers together. During the intercalation, Li donates one electron to the d-band of MoS_2 and Li^+ goes and sits between two sandwiched layers.
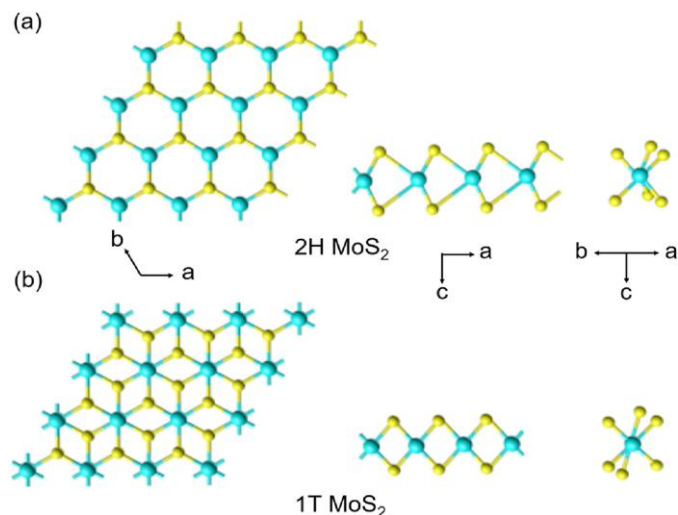
Figure 2.5 Top and side views of the a) 2H and b) 1T arrangement of MoS_2 (Gupta et al. 2020)

The MoS_2 layers get reduced and transform into 1T phase with octahedrally coordinated Mo atoms. The 2H phase exhibits a semiconductor nature whereas the 1T phase exhibits metallic nature. This 1T phase exits along with the 2H phase in the Li intercalated MoS_2 sheets.

In this process, there is a necessity to take precautionary measures during the handling of n-butyl lithium. This reacts violently with the water and needs to be stored under the inert gas atmosphere to prevent activity loss.

2.4.7.5 Solvent aid or liquid exfoliation

Coleman et al. (2011) separated individual MoS_2 sheets with the assistantce of organic solvent, N- methyl-pyrrolidone (NMP). The bulk MoS_2 powder was dispersed in the solvent. This dispersion was ultrasonicated to exfoliate the MoS_2 nanosheets. Then the resultant dispersion was centrifuged and the supernatant was collected. This final supernatant dispersion contained mixed mono-, bi-layer and few layer MoS_2 sheets.

Anbazhagan et al. (2014) used thioglycolic acid to exfoliate MoS_2 sheets from the bulk MoS_2 powder. Li et al. (2014) reported MoS_2 exfoliation using 45% ethanol-water mixture as the solvent. Narayanan et al. (2014) used dimethylformamide (DMF) as the solvent. Mishra et al. (2015) used a mixture of DM water and soup detergent as the

solvent. Weng et al. (2015) used NMP as the solvent to exfoliate the bulk MoS_2 powder into mono or few layer thick MoS_2 sheets.

2.4.7.6 Hydrothermal method

Huang et al. (2014a) synthesised MoS_2 nanosheets with sodium molybdate as the molybdenum source and L-cysteine as the sulfur source. The source materials were dissolved in DM water and ultrasonicated. Then it was transferred to a Teflon-lined autoclave. The autoclave was subjected to heat at 180 °C for 48 hours. The product was washed several times with water and ethanol, then vacuum dried at 80 °C for 12 hours.

Ren et al. (2015) used dibenzyl disulfide as the sulfur source instead of L-cysteine to synthesis MoS_2 nanosheets. The mixture of sodium molybdate in water and dibenzyl disulfide in ethanol was ultrasonicated. Then the mixture was transferred to a Teflon-lined autoclave and heated at 220 °C for 18 hours. The resultant suspension was centrifuged and the supernatant containing the MoS_2 sheets were collected.

Critical review on MoS₂ nanosheets

The liquid phase exfoliation of MoS_2 nanosheets is a simple and high yield route. The MoS_2 nanosheets have high mechanical strength and flexibility and excellent electrochemical stability. They are ideal materials to be used for energy storage applications like supercapacitors and batteries. It is reported that the electrochemical performance of the supercapacitors based on metal oxides like SnO_2, Mn_2O_3 and Co_3O_4 can be enhanced by composite them with the MoS_2 nanosheets.

2.5 Objectives of the Study

Silver nanowires could be synthesised with the presence of an alternative oxygen scavenger, other than Cu/Fe, to improve the aspect ratio of the silver nanowires. The manganese (Mn) ions have not been explored as the oxygen scavenger till now. The characteristics of manganese, such as (i) tendency to remove more oxygen owing to its high negative free energy for oxidation; (ii) large number of oxidation states (2, +3, +4, +5, +6 and +7) compared to that of Cu (+1 and +2) and Fe (+2 and +3) are expected to help in removing the oxygen effectively from the surface of silver seed particles.

The high solubility of the Zn/ZnO anode in the alkaline electrolyte could be controlled by changing the morphology into one-dimensional rod-like structures from the conventional cubic, prism-like structure. The hydrogen gas evolution and corrosion problems could be minimized by adding SnO_2 nanoparticles and two-dimensional MoS_2 nanosheets as additives to the anode material. The SnO_2 is an effective additive to Zn/ZnO anode in suppressing the hydrogen gas evolution and enhancing the conductivity. The MoS_2 nanosheets offer a large specific surface area similar to graphene. They can improve the interaction between the electrode and the electrolyte and facilitate charge transfer. The MoS_2 nanosheets can act as the conductive bridge between the individual ZnO and SnO_2 particles. The use of both MoS_2 nanosheets and SnO_2 nanoparticles together as an additive to Zn/ZnO anode is rarely explored. The composite of MoS_2-SnO_2 as an additive would bring the benefits from these materials for the betterment of zinc-based anode in alkaline batteries.

Hence, the following objectives are formulated.

1. **Fabrication of transparent conductive film of the silver nanowires synthesised in the presence of different chloride salts**
   - Synthesis and characterization of the silver nanowires with the presence of NaCl, $CuCl_2$ and $MnCl_2$
   - Preparation and characterization of the transparent conductive Ag NWs film made using spray coating
   - Testing of silver nanowires film for transparent heater application

2. **Synthesis and characterization of MoS_2 nanosheets**
   - Analysing the nature and purity of the synthesised MoS_2 nanosheets

3. **Preparation of MoS_2-SnO_2 nanocomposite for supercapacitor applications**
   - Preparation of nanocomposite of MoS_2 nanosheets and SnO_2 nanoparticles and its electrochemical characterization for supercapacitor application

4. **Preparation of hybrid MoS_2-SnO_2/ZnO anode for zinc alkaline battery application**
   - Synthesis of ZnO microrods, nanorods and their electrochemical characterization in the alkaline electrolyte (KOH)

- Electrochemical characterization of the MoS_2-SnO_2/ZnO hybrid electrode in the alkaline electrolyte (KOH)

2.6 Scope of the study

The study will help to understand the importance of oxygen scavengers during the synthesis of silver nanowires used to fabricate the flexible transparent conductive silver nanowires films. The study will help to realize the significance of appropriate additives and morphology of the electrode material in enhancing their electrochemical performance for the energy storage applications such as supercapacitors and alkaline batteries.

CHAPTER 3

MATERIALS AND METHODOLOGY

This chapter presents the details on the materials preparation and their various characterizations. The present chapter has three sections. They are 1. Fabrication of flexible transparent conductive silver nanowire films and their characterizations; 2. Preparation of MoS_2-SnO_2 nanocomposite and its characterizations; 3. Preparation of ZnO hybrid electrodes and their electrochemical characterizations.

3.1 Flexible Transparent Conductive Silver Nanowires Film

The fabrication of flexible transparent conductive silver nanowires films involves the synthesis of silver nanowires, purification process to separate the nanowires from by-products, coating silver nanowires on the desired substrate and post-film treatment to improve its properties.

3.1.1 Synthesis of silver nanowires

The silver nanowires were synthesised by the polyol method (Coskun et al. 2011). The materials used for the synthesis process are silver nitrate (SRL Laboratories, 99.9%), polyvinylpyrrolidone (Molychem), NaCl (TCI chemicals, >99.5%), $CuCl_2.5H_2O$ (SRL Laboratories, 98%), $MnCl_2.4H_2O$ (Nice chemicals, 95%) and ethylene glycol (Nice chemicals, 99%). The concentrations of the chemicals were optimized as follows.

First, the solutions of silver nitrate ($AgNO_3$), polyvinylpyrrolidone (PVP, M.W.=40,000), NaCl (44.5 mM), $CuCl_2.5H_2O$ (22 mM) and $MnCl_2.4H_2O$ (22 mM, 40 mM and 65 mM) were prepared by using ethylene glycol (EG) as solvent. A flask containing 15 ml solution of 0.147 M PVP was heated for 45 minutes at 170 °C in an oil bath under magnetic stirring. Then, 75 µL of chloride solution (NaCl or $CuCl_2.5H_2O$ or $MnCl_2.4H_2O$) was added to the flask. After three minutes, 3 ml $AgNO_3$ (0.153 M) solution was added to the flask. Upon adding $AgNO_3$, the solution was continued to be heated for another 2 hours for the growth of nanowires. After 2 hours of heating, the solution was removed from the oil bath and allowed to cool in the air. Finally, the as-synthesised product was washed with acetone and isopropyl alcohol.

3.1.2 Purification of silver nanowires

Two methods were explored to separate the silver nanowires and the particles produced from the synthesis step as by-products. Conventional centrifugation was the first method employed to remove undesirable silver particles (Jarrett and Crook 2016).
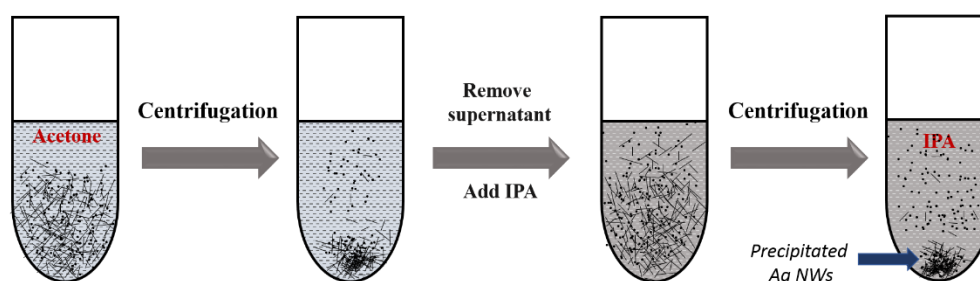
Figure 3.1 Purification of Ag nanowires by centrifugation process

In this method, as shown in Fig. 3.1, the silver product synthesised with the presence of Cu(II) ions was mixed with acetone and centrifuged at 4000 rpm for 20 minutes. After the completion of centrifugation, the supernatant was removed. Then, the isopropyl alcohol (IPA) was added to the precipitation settled at the bottom of the centrifuge tube. Now, the dispersion in IPA was centrifuged at 3000 rpm for 20 minutes. The supernatant in the tube was removed again. This step was repeated two more times. At last, the product settled at the tube bottom was dispersed in IPA and kept for storing.

The second method was the decantation and solvent-aid purification process. The as-synthesised silver product, synthesised with the presence of Cu(II) ions (and Mn(II) ions), was kept for settling for 12 hours. The product which remained as the supernatant was removed out from the flask (decantation). Next, acetone was added to the flask. The mixture was ultrasonicated for 2 minutes. This led the mixture to coagulate and settle at the bottom. The remained supernatant at this stage was removed. Now, the IPA solvent was added into the settled precipitation. The added IPA dispersed the precipitate. Next, the dispersed products were allowed to settle down slowly. After 15 minutes of time, the top half of the dispersion was removed, leaving the half-settled product in the flask itself. Both the supernatant and settled products at this stage were used for further characterization. Various stages involved in this purification method are schematically presented in Fig. 3.2.
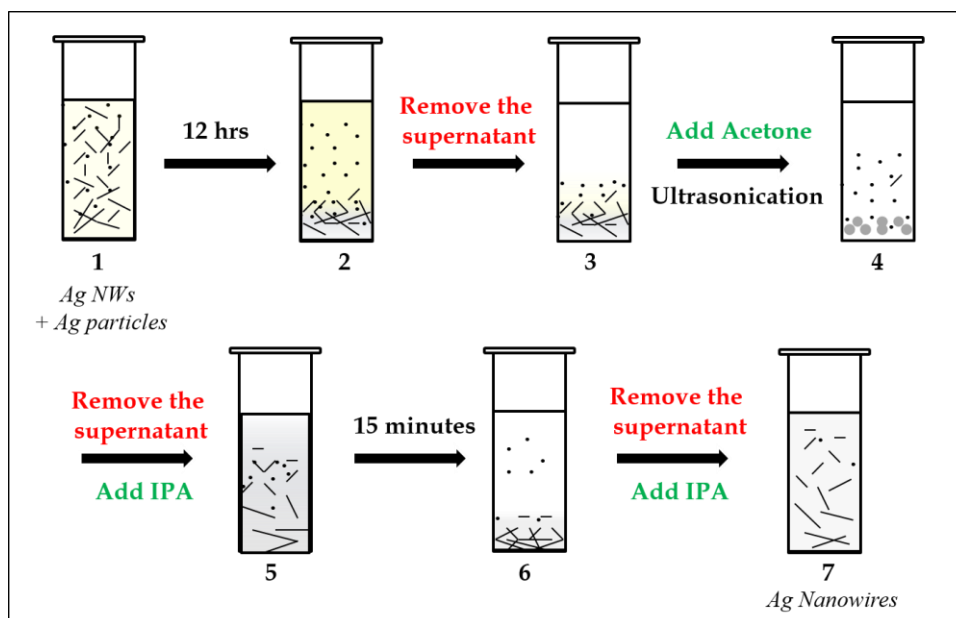
Figure 3.2 Schematic representation of the decantation and solvent-aid purification process

3.1.3 Coating transparent conductive silver nanowires film
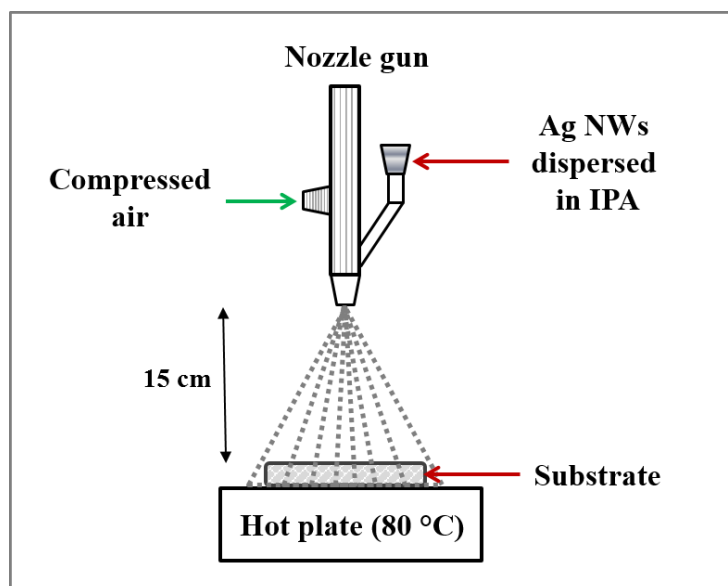
Figure 3.3 Spray coating of silver nanowires films

The silver nanowires films were prepared by spray coating technique. The silver nanowires dispersed in IPA were loaded into a commercial airbrush kit and spray-coated on the glass or plastic film substrate kept on a hot plate at 80 °C. The air pressure

used was 68.9 kPa (10 psi). The distance between the spray gun and the substrate was 15 cm. Later, the prepared silver nanowires films were subjected to annealing at 165 °C for 30 minutes to reduce the sheet resistance.

3.1.4 Characterization of silver nanowires and film

The prepared silver nanowires and silver nanowires films were subjected to various characterizations to analyse the growth, morphology, dimensions (length and diameter), stability under mechanical bending movements, electrical and optical properties which are essential to be used for transparent conductive applications (Langley et al. 2013).

3.1.4.1 X-ray diffractometry

The structural characterizations, such as phase identification and crystal growth direction of the synthesised silver nanowires were performed by using X-ray diffractometer (XRD; JDX 8P, JEOL) with Cu Kα (λ=0.154 nm) radiation. The XRD pattern was obtained in the 2θ range from 30° to 70° at the scan rate of 2°/min and step size of 0.02°. The sample was prepared by drop-casting the purified silver nanowires dispersed in IPA on a glass substrate. The collected XRD data was analysed by comparing it with the standard ICDD files.

3.1.4.2 Scanning electron microscopy

The morphological studies of the synthesised materials were carried by using scanning electron microscope (SEM) (JSM-6380LA, JEOL) and field emission scanning electron microscopy (FESEM; Carl Zeiss Sigma). The dimensions of the synthesised products were measured from the SEM/FESEM micrographs by using ImageJ software.

3.1.4.3 Transmission electron microscopy

The detailed morphological analysis of synthesised materials and selected-area electron diffraction (SAED) were obtained by using transmission electron microscope (TEM) (JEM-2100, JEOL). The samples for TEM analysis were prepared by diluting the synthesised materials with IPA and ultrasonicate them for 10 minutes. This step was essential to avoid the agglomeration of the synthesised materials. Then, one or two drops were taken from the middle of the dispersion and drop-casted on the 3 mm

diameter carbon-coated copper grid. The samples deposited on the copper grid were dried in order to remove the moisture from the samples.

3.1.4.4 UV-VIS spectroscopy

The optical absorption and transmittance spectra of the synthesised silver nanoparticles, silver nanowires and silver nanowires films were obtained by using UV-VIS spectrometer (SD2000, Ocean Optics). All the samples were dispersed in isopropyl alcohol solvent for the absorption spectra measurement. Isopropyl alcohol was used as the reference liquid for this measurement.

3.1.4.5 Electrical resistance test

The sheet resistance (R_s) of the coated silver nanowires films was measured by using four-probe measurement setup (SES instruments, India). The change in sheet resistance of the film subjected to the mechanical flexibility test was measured by the two-probe method using Fluke 15b+ multimeter. The silver paste was used to make electrical contacts at the two ends of the films for this purpose. A silver nanowires film of 2.5x2.5 cm coated on the plastic substrate was used as the sample. The width of the silver contacts was 3 mm.

3.1.4.6 Mechanical flexibility test

The silver nanowires film was spray-coated on a flexible plastic film to test the mechanical flexibility of the synthesised silver nanowires. The prepared film was bent to a curvature of 4.5 mm radius for 500 bending cycles. An ITO coated PET film was also subjected to this bending test for comparison purpose. The change in sheet resistance of silver nanowires film and ITO/PET was measured after every ten bending cycles.
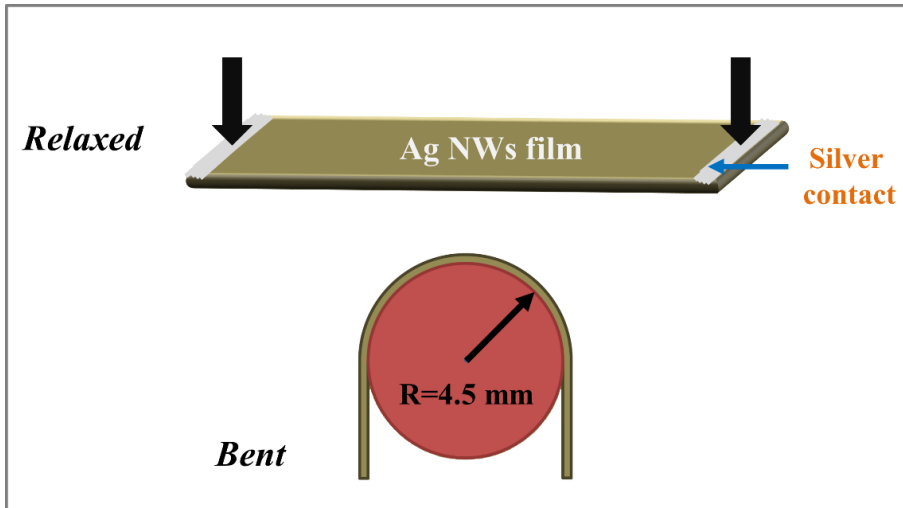
Figure 3.4 Bending test to examine the mechanical flexibility of the film

3.1.4.7 Transparent heater test

Electrical contacts were made at the two ends of the silver nanowires film by using the silver paste. The setup to test the heater performance of the silver nanowires film is shown in Fig. 3.5.
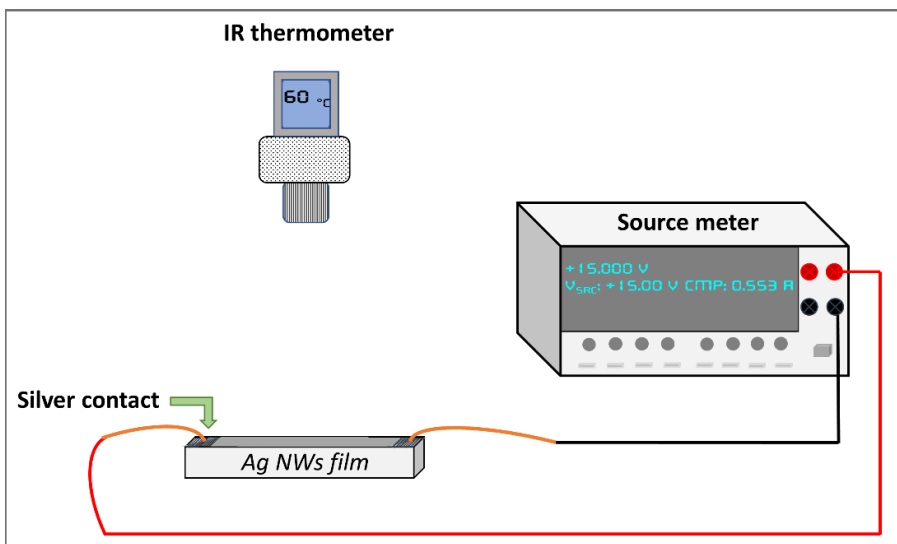
Figure 3.5 Silver nanowires film heater testing setup

The heater test was performed by applying the electrical potential between two electrical contacts made on the silver nanowires film using Keithley 2400 source meter. The heater test was conducted with different the applied voltages: 5, 7 and 10 V. The

temperature generated on the film in response to the applied potential was measured by using an infrared thermometer (HT-826; Temp. resolution= 0.1 °C).

3.2 MoS$_2$-SnO$_2$ Nanocomposite for Energy Storage Applications

The MoS$_2$ nanosheets are an excellent additive material to improve the performance of the metal oxides for electrochemical energy storage applications such as supercapacitors and batteries (Wang et al. 2016a) (Pan et al. 2016). The present work demonstrates the enhancement of electrochemical performance and stability of the SnO$_2$ nanoparticles by functionalizing them on the MoS$_2$ nanosheets.

3.2.1 Synthesis of MoS$_2$ nanosheets

The MoS$_2$ nanosheets were prepared by the ultrasonication-assisted liquid-phase exfoliation method (Liu et al. 2012). First, 150 mg of polyvinylpyrrolidone (PVP, MW~40,000) was dissolved in 10 ml ethanol. Next, 30 mg of bulk MoS$_2$ powder (Alfa Aesar, 325 mesh) was added to the above-prepared PVP solution. The mixture of MoS$_2$ and PVP in ethanol was ultrasonicated (Power= 50 W, f=33 kHz) for 4 hours to exfoliate the MoS$_2$ nanosheets.
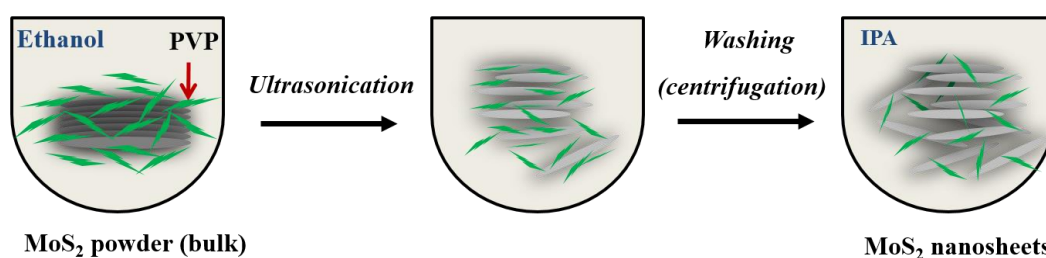
Figure 3.6 Exfoliation of MoS$_2$ nanosheets

After the exfoliation process, the exfoliated MoS$_2$ sheets which remained on top of the solution were transferred to the centrifugal tubes for washing. The product was mixed with acetone and centrifuged at 7000 rpm for 20 minutes. After removing the supernatant, isopropyl alcohol (IPA) was added to the precipitation settled at the bottom of the centrifugal tube. This exfoliated MoS$_2$ dispersion was again centrifuged at 8000 rpm for 20 minutes. Finally, the washed product was collected and suspended in IPA for storing.

3.2.2 Synthesis of SnO$_2$ nanoparticles

The SnO$_2$ nanoparticles were synthesised by following the work reported in the literature (Bob et al. 2016). First, 1 g of tin chloride pentahydrate (SnCl$_4$.5H$_2$O) was dissolved in 10 ml of ethylene glycol (EG). It was followed by the addition of 250 mg of ammonium chloride, 250 mg of ammonium acetate and 30 ml de-mineralized (DM) water in a round bottom flask. Then, the flask was heated to 90 °C in the oil bath for 2 hours. Upon heating, the synthesised product was washed with DM water and ethanol. Finally, the washed SnO$_2$ nanoparticles were dispersed in ethanol.

3.2.3 Functionalization of MoS$_2$ nanosheets with SnO$_2$ nanoparticles

The known density of MoS$_2$ nanosheets dispersion was added into a vial containing the known weight of SnO$_2$ nanoparticles dispersion. Then the two materials were well dispersed together by using ultrasonication bath. After the ultrasonication, the materials were allowed to get settled at the bottom of the vial. Then the supernatant liquid was removed and the materials settled at the bottom were used for our study. Likewise, five different compositions of MoS$_2$-SnO$_2$ nanocomposites were prepared with varying the weight ratio of MoS$_2$ nanosheets (0.5%, 1%, 2.5%, 5% and 10%) to SnO$_2$ nanoparticles. The camera images of each step involved in this preparation process are shown in Fig. 3.7.
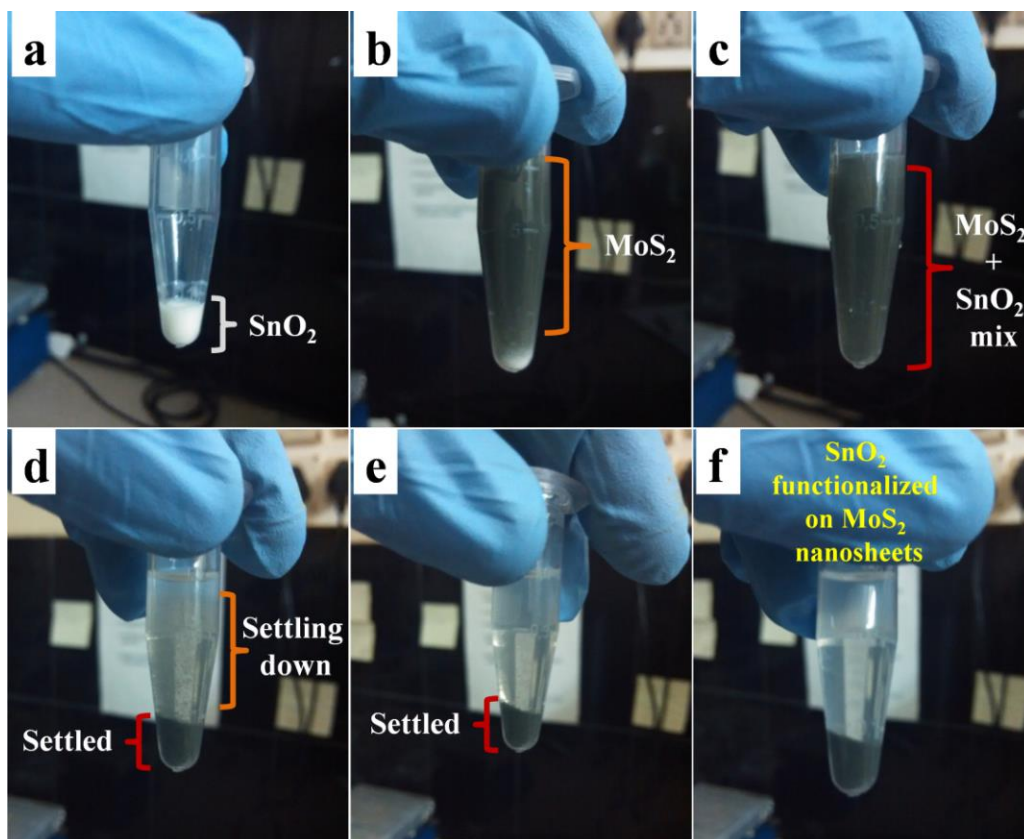
Figure 3.7 Camera images show the steps involved in the preparation of MoS_2-SnO_2 nanocomposite

3.2.4 Characterization of MoS_2-SnO_2 nanocomposite

3.2.4.1 X-ray diffractometry

The structural characterization and phase identification of the synthesised materials were performed by using X-ray diffractometer (XRD; JEOL, JDX 8) with Cu Kα (λ=0.154 nm) radiation at the scan rate of 1°/min and step size of 0.02°. The XRD patterns were collected in the 2θ range from 10° to 60°. The MoS_2 nanosheets, SnO_2 nanoparticles and MoS_2-SnO_2 nanocomposite were drop-casted on the glass substrate and used as the samples. The collected XRD data were analysed by comparing it with the standard ICDD files.

3.2.4.2 Scanning electron microscopy

The morphological studies of the synthesised materials were carried by using field emission scanning electron microscopy (FESEM; Carl Zeiss Sigma). The sample preparation for FESEM analysis was done by drop casting the dispersion of MoS_2 nanosheets and MoS_2-SnO_2 nanocomposite on a glass slide. Upon drying, the samples deposited on the glass slide were sputter-coated with thin gold layer before used for the FESEM analysis.

3.2.4.3 Transmission electron microscopy

The detailed morphology of the synthesised materials and selected-area electron diffraction (SAED) were analysed by using transmission electron microscope (TEM) (JEM-2100, JEOL make). The samples were drop cast on a 3 mm diameter carbon-coated copper grid.

3.2.4.4 Raman spectroscopy

The Raman spectra of bulk and exfoliated MoS_2 were obtained by using Raman spectrometer (Horiba Jobin-Yvon, labRAM HR) with an excitation wavelength of 532 nm.

3.2.4.5 X-ray photoelectron spectroscopy

The X-ray photoelectron spectrometer (XPS) was performed to analyse the nature of materials by determining their present oxidation states from their binding energy peaks. The surface chemistry of the materials was analysed by using X-ray photoelectron spectrometer (XPS; Thermo scientific, Multilab 2000) instrument (Mg Kα X-ray, 200 W excitation source).

3.2.4.6 Particle size analysis

The particle size of SnO_2 nanoparticles was determined by using particle size analyser (Malvern Zeta Sizer, NanoZS). The particle size distribution obtained from this study was used to compare it to the average particle size measured from the electron microscopic study.

3.2.4.7 Surface area analysis

The specific surface area and pore size distribution of MoS_2 nanosheets were analysed by Brunauer–Emmett–Teller (BET) and Barrett–Joyner–Halenda (BJH) method using surface area analyser (Microtrac, BELSORP Max). It was necessary to measure the specific surface area of the MoS_2 nanosheets as the charge transfers during the electrochemical cycles are facilitated through the surface of MoS_2 nanosheets.

3.2.4.8 Electrochemical characterization

Electrochemical studies were carried out with a standard three-electrode cell using SP-150 electrochemical workstation (BioLogic, France). Platinum wire and saturated calomel electrode (SCE) were used as the counter electrode and reference electrode, respectively. The working electrode was prepared as follows: 4.5 mg of nanocomposite was added into 250 µL water/ethanol (2:1 v/v) solution containing 15 µL Nafion (5 wt%). The above mixture was ultrasonicated for 15 minutes to obtain a homogeneous mixture. 50 µL of the prepared mixture was drop cast on a graphite electrode (10 mm diameter rod). The calculated mass of the active electrode material was 1.1 mg cm^{-2}. The aqueous solution of 2 M KOH dissolved in DM water was used as the electrolyte.

3.3 Electrochemical Performance of ZnO Hybrid Electrode in Alkaline Electrolyte

The ZnO is used as the anode material in zinc batteries that use alkaline electrolytes. The performance, life cycle and rechargeability of these batteries depend on the stability of the anode. Morphological changes, solubility in the electrolyte and H_2 gas evolution at the anode are the important factors to be considered to achieve a good battery performance (Zhang et al. 2018b). The present work deals with the mentioned factors by engineering the morphology of the anode material and additives added to the anode material.

3.3.1 Synthesis of one dimensional ZnO rods

The concentrations of the precursors used were optimized to the laboratory condition. ZnO nanorods were synthesised by microwave heating. 22 g of $Zn(NO_3)_2.6H_2O$ and 4.2 g of KOH were dissolved in 100 ml de-mineralized (DM) water. Then, ammonia was

added into this solution dropwise under continuous stirring to bring the pH value to 11. After that, the prepared solution was heated in a microwave oven at 700 W for 5 min. The final product was then washed with the DM water and the ethanol for three cycles.

ZnO microrods were synthesised by the hydrothermal method. 4.5 g of $Zn(NO_3)_2.6H_2O$ and 0.850 g of KOH were dissolved in 30 ml de-mineralized (DM) water. Ammonia was added into the solution dropwise under continuous stirring to adjust the pH value to 11. Then, the entire solution was transferred to a Teflon-lined stainless autoclave. This autoclave was heated in a hot air oven at 180 °C for 48 h. Finally, the final product was washed with the DM water and the ethanol for three cycles. Commercial ZnO nanoparticles (Platonic Nanotech, India) were used in this study to compare the performance of synthesised ZnO samples.

3.3.2 MoS$_2$-SnO$_2$/ZnO preparation

The preparation of MoS$_2$-SnO$_2$ nanocomposite is explained earlier in section 3.2.3. The 5% MoS$_2$-SnO$_2$ nanocomposite powder was added as the additives to the ZnO powders (ZnO nanoparticles, ZnO nanorods and ZnO microrods). The mixtures were then added into the PVA dissolved in DM water. The PVA was serving as the binder. The weight ratio of ZnO, MoS$_2$-SnO$_2$ and PVA was maintained at 75:15:10, respectively.

3.3.3 Material characterization of ZnO and MoS$_2$-SnO$_2$/ZnO:

The structural characterization of synthesised ZnO rods and commercial ZnO nanoparticles was performed by using X-ray diffractometer (XRD; JEOL, JDX 8) with Cu Kα (λ=0.154 nm) radiation at the scan rate of 1°/min and step size of 0.02°. The collected XRD data was analysed by comparing it with the standard ICDD files. The morphological studies of the ZnO materials were carried by using field emission scanning electron microscopy (FESEM; GeminiSEM 500, Carl Zeiss).

3.3.4 Material solubility test

The solubility of ZnO materials in the alkaline electrolyte was determined. 5 mg of ZnO nanorods, ZnO microrods and commercial nanoparticles, each were added into separate vials that contained 6 M KOH in water solution. After 12 hours, the supernatant solution

was taken out from each ZnO sample vial and subjected to atomic absorption spectroscopy (AAS) analysis. The analysis was performed by using GBC 932 atomic absorption spectrometer.

3.3.5 Electrochemical measurements

The electrochemical studies of all ZnO materials were performed with the three-electrode cell setup by using Flex-OGF05A potentiostat (Origaly's, France) and OrigaFlex-OGFEIS impedance analyser (Origaly's, France). The ZnO powder (ZnO nanoparticles, ZnO nanorods and ZnO microrods) was added into the binder solution of PVA dissolved in DM water. The well-mixed slurry of ZnO was drop-casted on the glassy carbon electrode. This was used as the working electrode for electrochemical studies. The platinum wire and saturated calomel electrode were used as counter electrode and reference electrode, respectively. The 6 M KOH dissolved in water was used as the electrolyte (Yang et al. 2018).

i. Prior to all the electrochemical tests, the electrochemical cell was in open-circuit potential for 10 minutes to ensure that the cell reached a steady state.

ii. The cyclic voltammetry (CV) test was conducted in the potential range from -2 V to -0.95 V at the scan rate of 10 mV s^{-1} as the anodic and cathodic peaks of ZnO are expected to be appeared in this range (Renuka et al. 2001).

iii. Potentiodynamic polarization was used to study the corrosion behaviour of ZnO materials. The test was performed at the scan rate of 1 mV s^{-1}. The potential range was selected so that 'E_{corr}' of ZnO in KOH electrolyte fall in this range (Huang et al. 2014a). The Tafel curve was obtained by plotting the values of potential versus log I (current).

iv. Linear sweep voltammetry (LSV) was performed at the potential range from 0 V to -2.5 V at the scan rate of 5 mV s^{-1}. The wide range of potential was selected to observe the current response to study the hydrogen gas evolution in the material.

v. Electrochemical impedance spectroscopy (EIS) was carried out with the AC sine wave amplitude of 10 mV in the frequency range from 0.1 Hz to 100 kHz.

CHAPTER 4

TRANSPARENT CONDUCTIVE SILVER NANOWIRES FILM

This chapter presents the polyol synthesis of silver nanowires, fabrication of transparent conductive silver nanowires films and its performance as the transparent heater. This chapter discusses the effect of $MnCl_2$ addition on the morphology of synthesised silver nanowires. The opto-electrical characteristics of fabricated silver nanowires films are discussed in detail.

4.1 Synthesis and Purification of Silver Nanowires

The SEM micrograph of silver nanowires synthesised with the addition of $CuCl_2.5H_2O$ after the centrifugation process is shown in Fig. 4.1. It is observed that there are still many nanoparticles and microrods present along with the nanowires. In order to use these silver nanowires for transparent conductive electrode (TCE) application, these particles have to be removed. Thus, it was convinced that the centrifugation process alone was not enough to separate silver nanowires (Ag NWs) from the undesired silver particles.
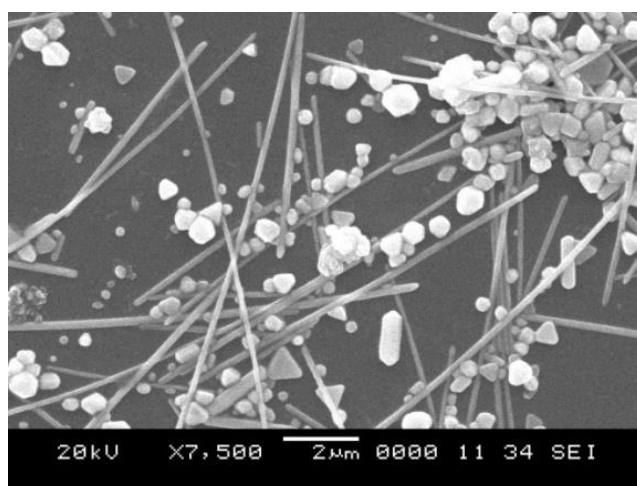
Figure 4.1 SEM micrograph of the synthesised silver product after the centrifugation process

The proposed alternative method, 'decantation and solvent-aid purification process' shown in Fig. 3.2, is explained in the following steps. The as-synthesised solution was kept undisturbed overnight for the synthesised products to settle down at the bottom of the flask. This leaves the excess ethylene glycol (EG) and polyvinylpyrrolidone (PVP) along with the small nanoparticles in the supernatant. After removing the supernatant from the flask, the precipitate (sediment) at the bottom of the flask contained only nanowires, nanoparticles and micrometer length rods (Fig. 3.2; Stage 3). In the next step, acetone was added to the precipitate in the flask and ultrasonicated for two minutes. The surface of the silver products (nanowires, particles, rods) was covered by the capping agent, PVP. But the PVP is insoluble in acetone. So, the synthesised nanowires were allowed to settle down like precipitates at the bottom of the flask when acetone was added to it (Fig. 3.2; Stage 4). Due to the lower weight, the nanoparticles were still in the supernatant. When the supernatant was removed between stages 3 and 4, these nanoparticles were separated out from the solution. This was confirmed from the SEM micrograph of the supernatant shown in Fig. 4.2
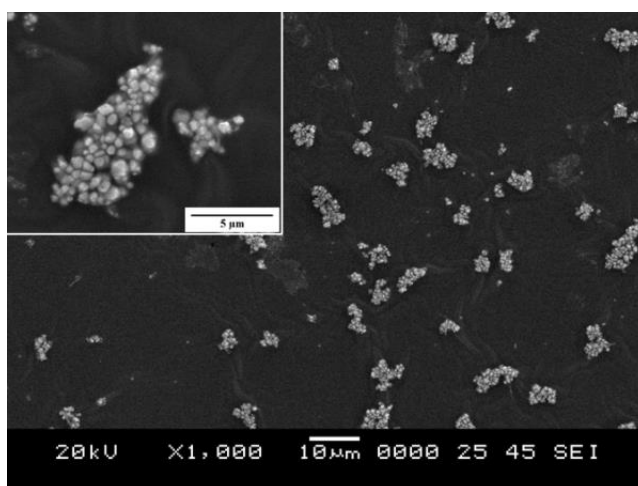
Figure 4.2 SEM micrograph of supernatant: after the addition of acetone (between stages 3-4, of purification process explained in Fig. 3.2)

Then, isopropyl alcohol (IPA) was added to this precipitate (containing nanowires, rods and large particles) and mixed properly. The PVP molecules are soluble in IPA. So, the precipitates at this stage got dispersed entirely in the IPA solvent. With a holding period, the metallic silver got settled down due to its mass. For the same reason, the

silver nanowires got settled faster than the silver particles. After 15 minutes, the top half of the dispersion was removed, leaving the bottom half in the flask. The top half solution was analysed by SEM and the corresponding micrograph is shown in Fig. 4.3.
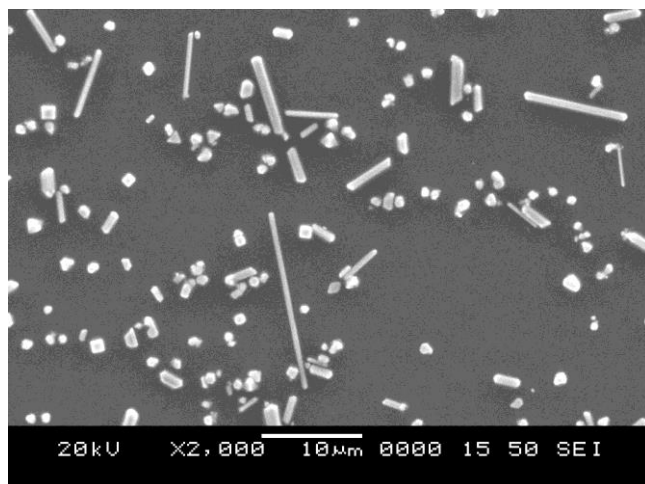
Figure 4.3 SEM micrograph of supernatant: after the addition of IPA (between stages 6-7, of purification process explained in Fig. 3.2)

It was observed that the supernatant removed after the addition of IPA (between stages 6-7) contained particles in the size of nanometers and micrometers. Few short rods were also present.
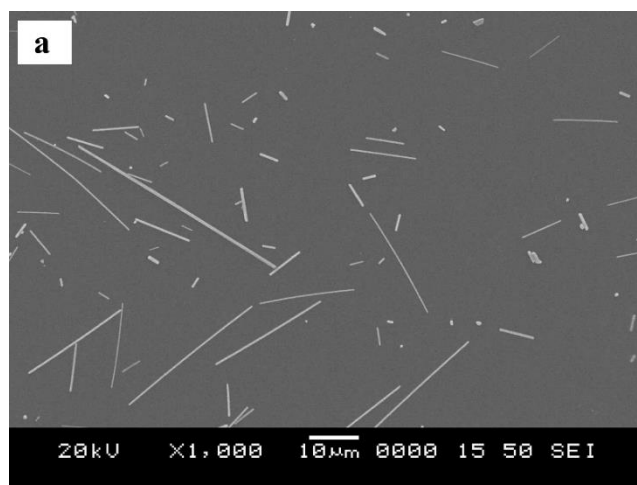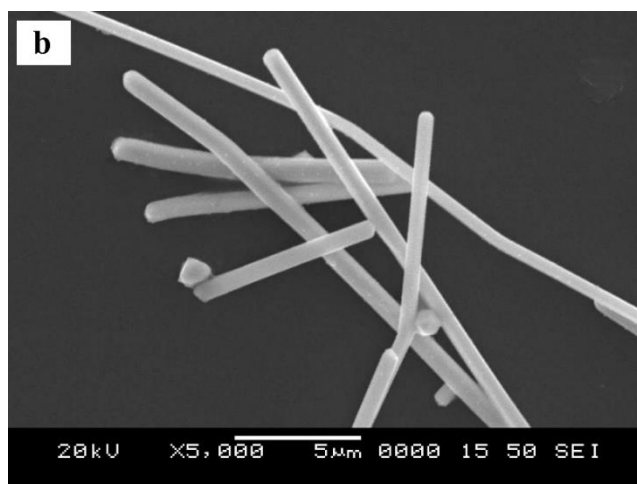
Figure 4.4 a), b) SEM micrographs of silver nanowires after decantation and solvent-aid purification

The bottom half dispersion at the last stage was analysed by SEM and shown in Fig. 4.4. The final product contained nanowires of length 5-20 µm, few particles and short nanowires. By comparing the centrifugation method and the 'decantation & solvent-aid purification' method, the second method was more effective in the purification of silver nanowires from the undesired particles. This method was followed for the purification of silver nanowires synthesised with other chloride conditions as well. The yield of silver nanowires was estimated as 72% while the undesired silver nanostructures was 28%.

4.2 Effect of Chloride Salts on the Growth of Silver Nanowires

The change in the morphology of the synthesised silver products with respect to four different types of chloride solutions is given with the help of FESEM micrographs. The four chloride conditions are, i) without any chloride salt; ii) with the addition of NaCl; iii) with the addition of $CuCl_2$ and iv) with the addition of $MnCl_2$.

Figure 4.5 shows the FESEM micrographs of silver products synthesised without any chloride salt. The product synthesised without the addition of any chloride lead to the growth of silver spherical-like particles. The size of the particles was measured to be in the range of 110 nm to 1 µm, with an average size of 330 nm. The dimensions of the silver nanowires were measured with the help of ImageJ software.

63
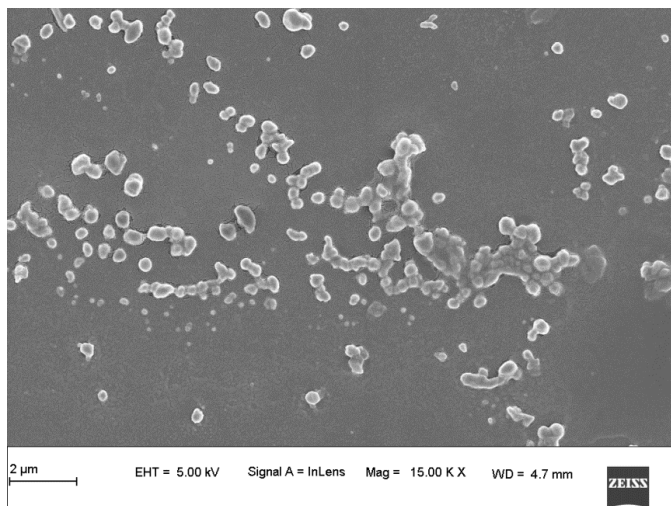
Figure 4.5 FESEM micrograph of the silver particles synthesised without the addition of any chloride salt

The rapid reduction of Ag^+ ions from $AgNO_3$ to Ag^0 during the synthesis process was the reason behind the formation of the silver particles. The reduction reaction of Ag^+ ions to Ag^0 is so fast that the reduced silver cannot grow as multi-twin particles. The absence of twins which serve as seeds for nanowires, resulted in the growth of silver particles instead of nanowires. These silver particles subsequently grew into larger particles via Oswald ripening process (Coskun et al. 2011).
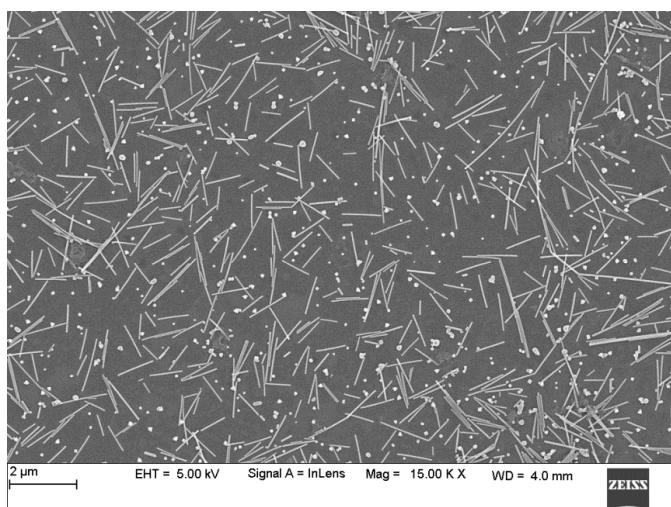
Figure 4.6 FESEM micrograph of the silver products synthesised with the addition of NaCl

Figure 4.6 shows the FESEM micrograph of silver product synthesised with the addition of NaCl during the synthesis process. The micrograph shown in Fig. 4.6 reveals that the addition of NaCl promoted the one-dimensional growth of silver that resulted in silver nanorods. It is observed that there are other structures, such as cubes (avg. size= 74 nm) and pyramid (avg. size= 119 nm) particles also produced along with the nanorods. The addition of NaCl prevented the rapid reduction of Ag^+ ions to Ag^0 by the formation of AgCl. The AgCl acted as a buffer phase. It ensured the controlled release of silver into the reaction for the one-dimensional growth (Coskun et al. 2011). Hence, the presence of Cl^- ions during the synthesis process is important to prevent the formation of silver particles and to promote the one-dimensional growth of silver nanostructures.
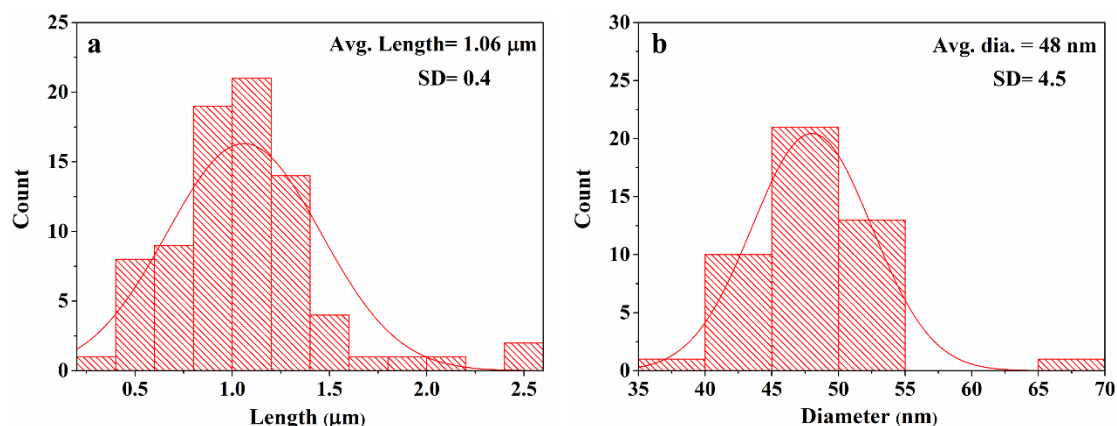
Figure 4.7 a), b) Length and diameter distribution of Ag nanorods synthesised with the addition of NaCl

The mean length and diameter of the silver nanorods are 1 µm and 48 nm, respectively (Fig. 4.7). These silver nanowires are very short in length to be used for the TCE application. The film fabricated from these silver nanorods would have more sheet resistance and less optical transparency. The growth of short silver nanorods was the result of oxygen etching of silver twinned particles. During the synthesis, the atomic oxygen (O_a) present in the reaction solution tends to etch away the twinned particles that otherwise serve as the seeds for silver nanowires growth. The etching of twinned seed particles leads to short nanowires or nanorods (Wiley et al. 2004).

Figure 4.8 FESEM micrograph of the silver nanowires synthesised with the addition of CuCl$_2$
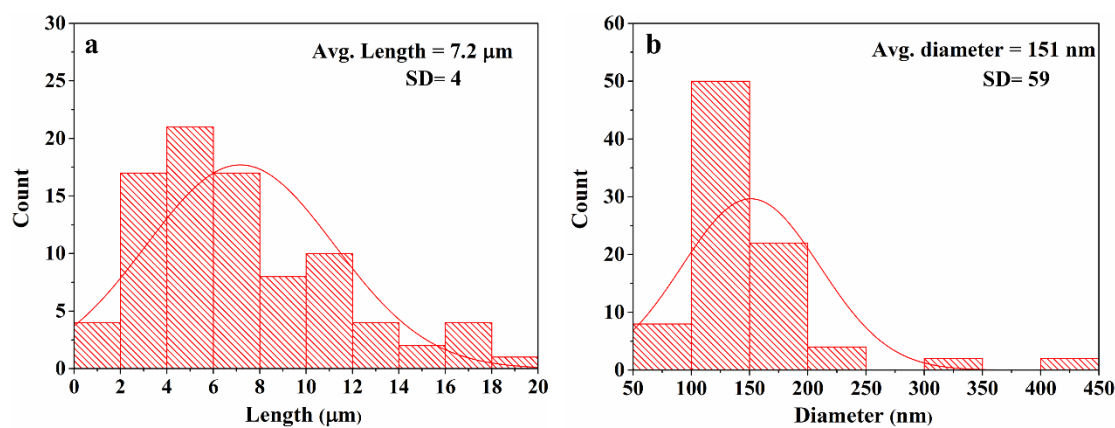
Figure 4.9 a), b) Length and diameter distribution of silver nanowires synthesised with the addition of CuCl$_2$

Figure 4.8 shows the FESEM micrograph of silver nanowires synthesised with the addition of CuCl$_2$.5H$_2$O during the synthesis process. The synthesis of silver nanowires with the addition of CuCl$_2$ produced nanowires along with a few short rods and particles. The addition of copper chloride in place of NaCl is a proven approach to act against the oxygen etching of twinned particles. The mean length of these silver nanowires was enhanced up to 7.2 µm with the maximum length up to 20 µm (Fig. 4.9a) when NaCl is replaced with the copper chloride. The introduction of copper ions into the reaction through copper chloride avoided the aggregation of the silver particles.

In addition to that, the copper ions prevented the oxygen etching of twins by scavenging the atomic oxygen from the surface of the twinned silver particles (Korte et al. 2008). But there is a concern with the diameter of the nanowires. The average diameter of the nanowires synthesised with the addition of copper ions was measured as 151 nm (Fig. 4.9b). Although the addition of copper ions helped to enhance the length of the silver nanowires, it also increases the diameter of the nanowires as well. The production of large diameter (125 to 250 nm) silver nanowires synthesised with copper ions is already reported (Bob et al. 2016).

The large diameter silver nanowires would block more light when it is used to fabricate a transparent conductive electrode (TCE) film. As a result, the optical transparency of the film is expected to reduce. Many efforts were taken in recent times to decrease the diameter of the silver nanowires by optimizing the other parameters, like the use of longer chain length PVP molecules Da Silva et al. (2016) or use of Br$^-$ ions (Zhang et al. 2018a), introducing benzoin-derived radicals Niu et al. (2018), high pressure (Jang et al. 2017) and N_2 gas environment synthesis Azani and Hassanpour (2019). The present work has explored manganese ions as the alternate oxygen scavenger to copper and iron ions without changing any other synthesis parameters.

4.3 Influence of Mn(II) Ions on the Growth of Silver Nanowires

The Mn(II) ions are added during the synthesis of silver nanowires as the oxygen scavengers in place of copper ions to prevent the etching of twinned seed particles. It removes the atomic oxygen adsorbed on the surface of the silver seed particles. The effect of Mn(II) ions with a different concentration on the growth of silver nanowires is given in detail in this section.

Figure 4.10 a), b) show the FESEM micrograph of silver nanowires synthesised with the addition of 22 mM $MnCl_2$. From the FESEM micrographs, it is observed that the synthesised products contained nanowires and very few particles. The average length of the nanowires was measured as 5.2 µm with the maximum length of 16 µm (Fig. 4.11). The average diameter of the nanowires was measured as 60 nm.

Figure 4.10 a), b) FESEM micrographs of the silver nanowires synthesised with the addition of 22 mM MnCl$_2$
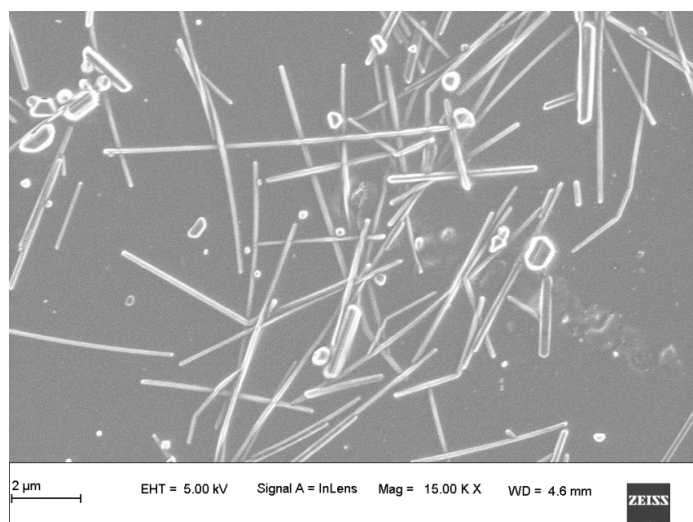

Figure 4.11 a), b) Length and diameter distribution of silver nanowires synthesised with the addition of 22 mM MnCl$_2$

68

The average diameter of these nanowires is significantly smaller than the average diameter of nanowires (151 nm) synthesised with the addition of $CuCl_2$ (Fig. 4.8 and 4.9). It should also be noted that the particles produced along with the nanowires were decreased considerably compared to that synthesised with the addition of $CuCl_2$. The decrease in the number of particles and the smaller diameter nanowires would minimize the light scattering that, in turn, enhance the optical transparency of the film fabricated with these silver nanowires. Moreover, the aspect ratio of the nanowires also will increase by decreasing the diameter of the nanowires. The silver nanowires with a high aspect ratio are essential to obtain highly transparent and conductive films.

Figure 4.12 a), b) FESEM micrographs of the silver nanowires synthesised with the addition of 40 mM $MnCl_2$
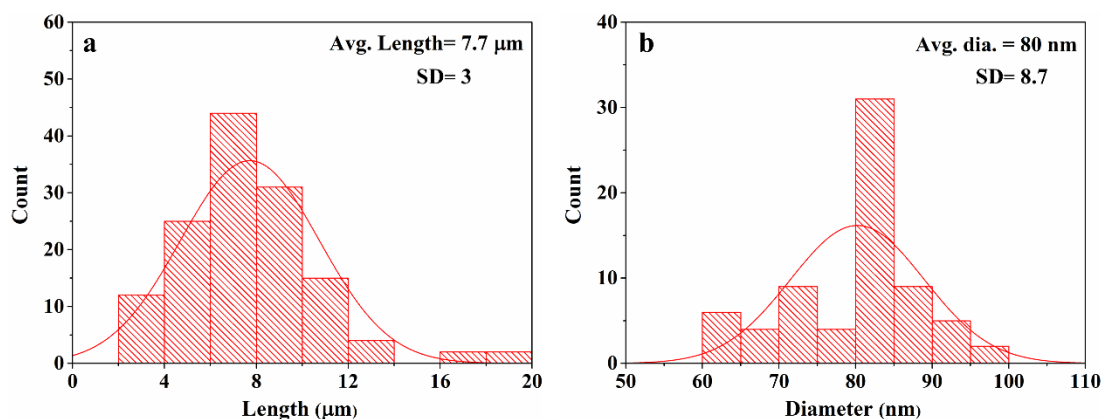
Figure 4.13 a), b) Length and diameter distribution of silver nanowires synthesised with the addition of 40 mM $MnCl_2$

Figure 4.12 shows the FESEM micrographs of silver nanowires synthesised with the addition of 40 mM concentration $MnCl_2$. The silver nanowires morphology is observed to be similar to that synthesised with the 22 mM concentration $MnCl_2$. However, it should be noted that the increased concentration of $MnCl_2$ enlarged the length and diameter of the silver nanowires. The average length of 40 mM $MnCl_2$ silver nanowires was measured as 7.7 µm which is longer compared to 5.2 µm (22 mM $MnCl_2$ Ag NWs). The silver nanowires have grown up to the maximum length of 20 µm. The length distribution of the nanowires is shown in Fig. 4.13a. Likewise, the corresponding diameter distribution is shown in Fig. 4.13b. It is observed that the average diameter of the 40 mM $MnCl_2$ silver nanowires was measured as 80 nm which is relatively larger compared to that synthesised with the addition of 22 mM $MnCl_2$.

The FESEM micrographs of silver nanowires synthesised with the addition of 65 mM $MnCl_2$ are shown in Fig. 4.14. When the concentration of the $MnCl_2$ was increased from 40 mM to 65 mM, the length and diameter of the synthesised silver nanowires were reduced (Fig. 4.15).
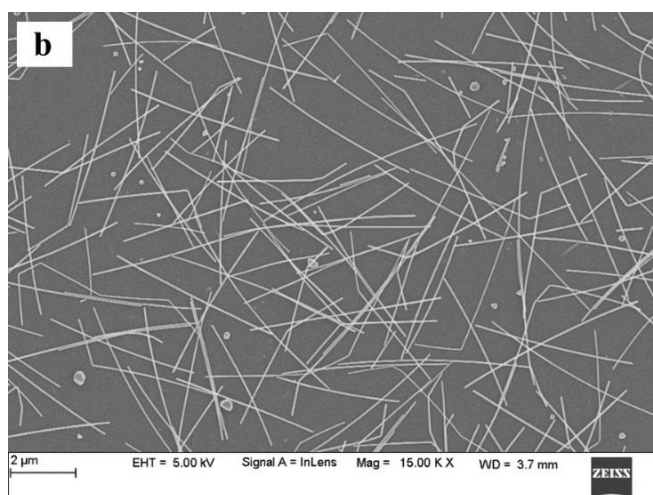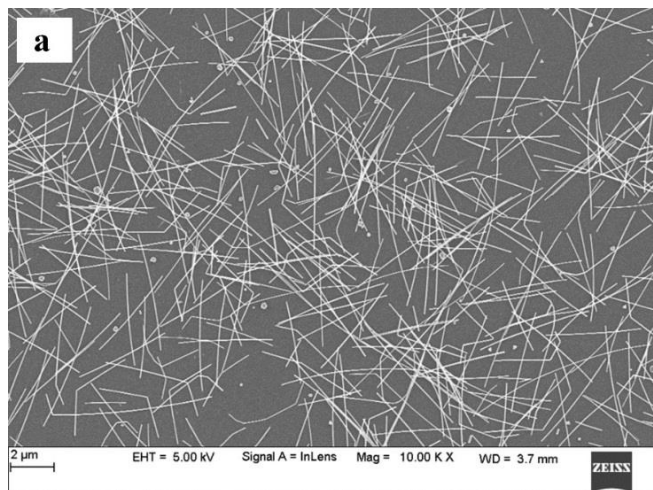
70
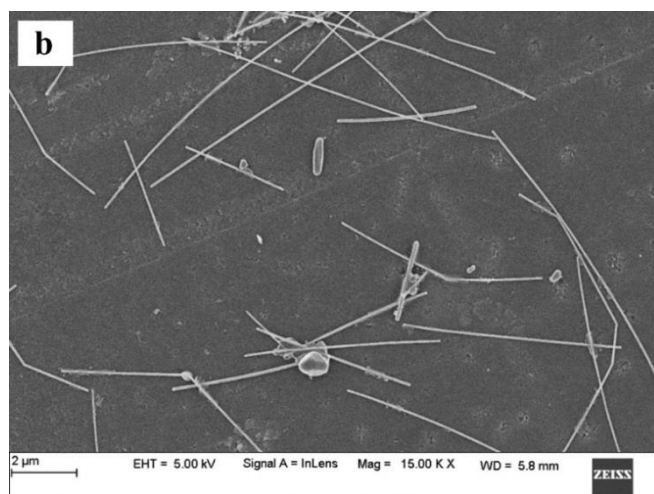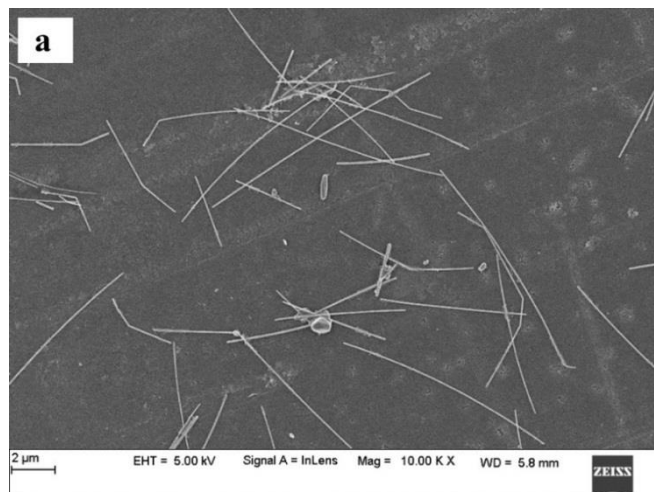
Figure 4.14 a), b) FESEM micrographs of the silver nanowires synthesised with the addition of 65 mM MnCl$_2$
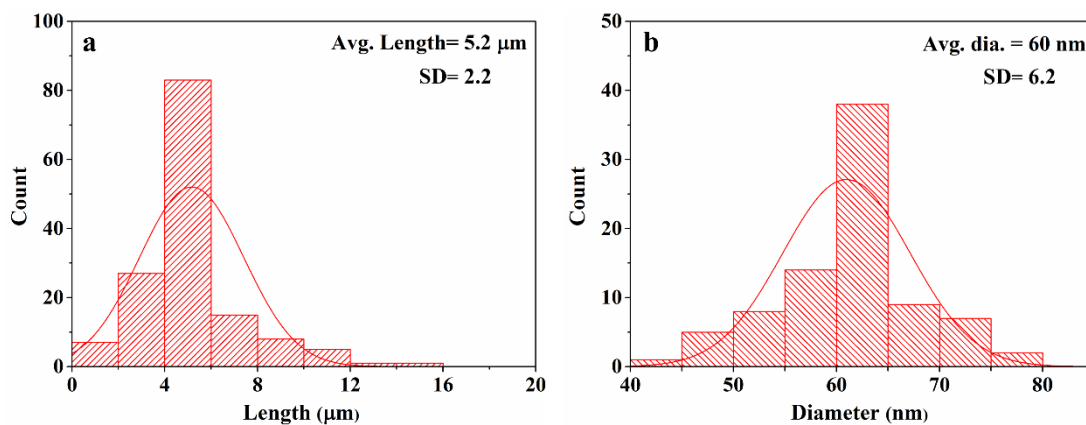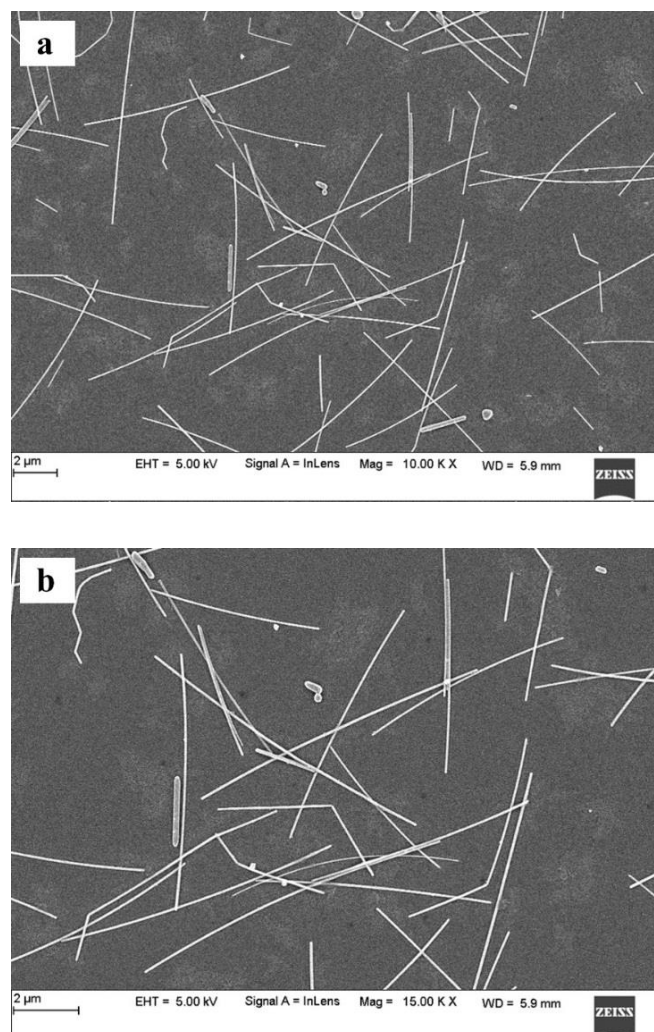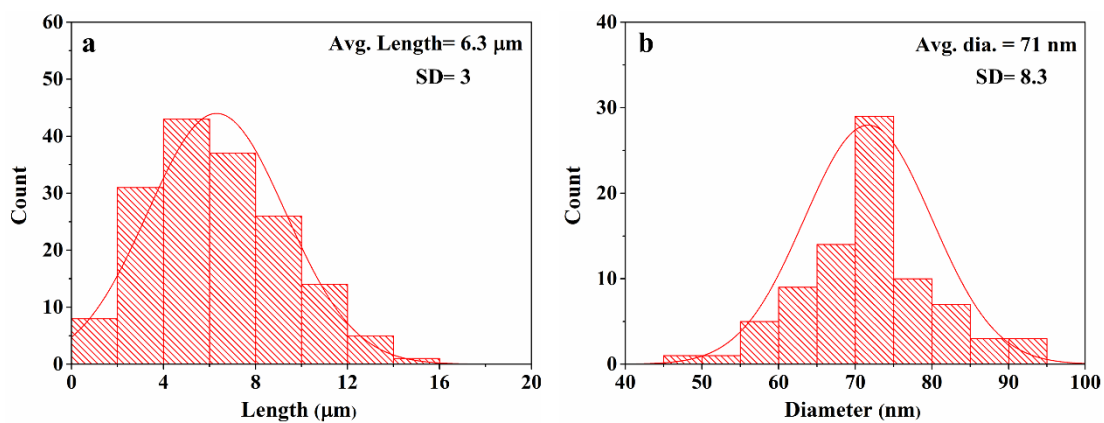

Figure 4.15 a), b) Length and diameter distribution of silver nanowires synthesised with the addition of 65 mM MnCl$_2$

The measured average length of the silver nanowires obtained from length distribution (Fig. 4.15a) was 6.3 µm with a maximum length of 16 µm. It is inferred that the further increase in the concentration of $MnCl_2$ did not enhance the growth of the nanowires. The measured average diameter of the 65 mM $MnCl_2$ silver nanowires was 71 nm (Fig. 4.15b).

In brief, the average diameter of the synthesised silver nanowires was measured as 60 nm, 80 nm and 71 nm for the $MnCl_2$ concentration of 22 mM, 40 mM and 65 mM, respectively. Though the 40 mM sample is reported to have large diameter, its corresponding length is longer compared to other silver nanowires samples. The significance of the length and diameter of the silver nanowires can be well understood when they are shown in terms of aspect ratio (length to diameter).
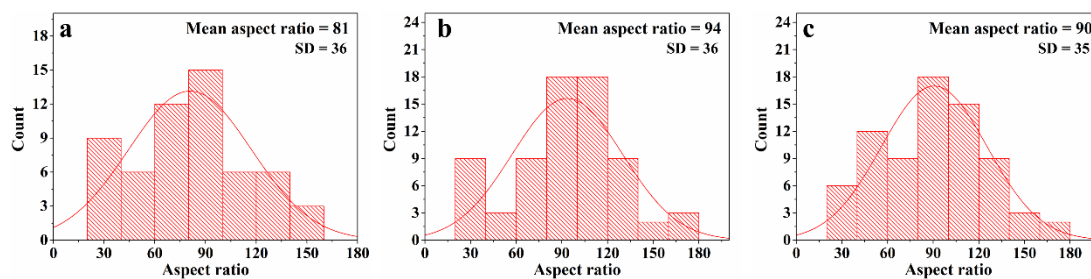
Figure 4.16 Aspect ratio distributions of silver nanowires synthesised with the addition of $MnCl_2$ of concentration a) 22 mM, b) 40 mM and c) 65 mM

The aspect ratio was calculated for the silver nanowires synthesised with the addition of three different $MnCl_2$ concentration samples (Fig. 4.16). The calculated aspect ratio for silver nanowires synthesised with 22 mM, 40 mM and 65 mM $MnCl_2$ was 81, 94 and 90, respectively. The mean aspect ratio of 40 mM concentration sample was the highest among all the silver nanowires samples. The high aspect ratio of silver nanowires will be beneficial to improve the percolation path, which in turn will increase the electrical conductivity of the silver nanowires film fabricated from this silver nanowires sample (Mutiso et al. 2013) (Jang et al. 2017). As the electrical percolation is achieved with the minimum number of silver nanowires, that would help to increase the optical transparency of the film (Jang et al. 2017).
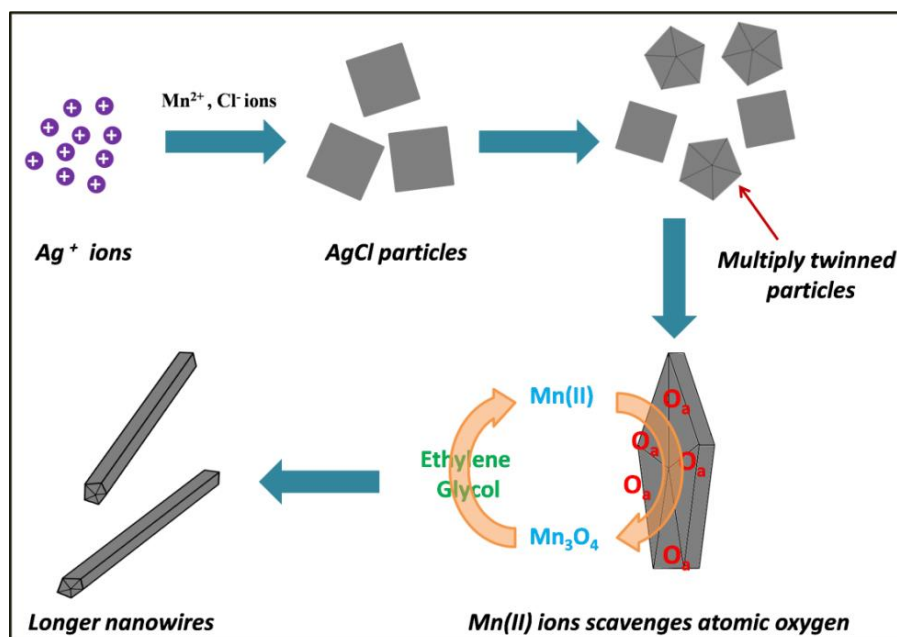
Figure 4.17 Schematic shows the role of Mn(II) ions as the oxygen scavenger in preventing oxidative etching of the silver seeds

The schematic shown in Fig. 4.17 explains the influence of Mn(II) ions on the growth of the silver nanowires. During the synthesis, when Ag^+ ions are reduced to Ag^0 to form nuclei, the twins are formed due to thermal energy availability (Coskun et al. 2011). Multiply-twinned decahedra twins are the most stable and more favourable one to form. These multiply twinned particles (MTP) acts as the seeds for silver nanowires growth (Wiley et al. 2004). But this growth is often affected by the atomic oxygen, dissociated molecular oxygen from EG, adsorbed on these seed particles. The adsorbed oxygen would etch away the twinned seed particles. Also, it would block the surface of seed particles for the addition of new silver species (Wiley et al. 2004). This oxygen etching effect eventually results in the formation of nanocubes or short nanorods instead of nanowires (Wiley et al. 2004). When Mn(II) ions are introduced into the reaction through $MnCl_2$, the Mn(II) ions get oxidized to a higher oxidation state by absorbing the atomic oxygen from the surfaces of the seed particles. The oxidized manganese ions are subsequently reduced back to Mn(II) state by the ethylene glycol (Larcher et al. 2000). This oxidation and reduction process of Mn ions is continued to remove or scavenge the oxygen to prevent the etching of twinned particles. Thus, the twinned seed particles with active {111} sites remain available for the addition of new silver species.

73

When the Mn(II) ions absorb oxygen from the surface of silver seed particles, the following are the possible compounds to be formed, namely, Mn_3O_4, Mn_2O_3 and MnO_2. Among the oxides of Mn, the Gibbs free energy of formation ($\Delta G_f°$) for Mn_3O_4 is more negative than other manganese oxide compounds. In the case of $CuCl_2$, the Cu(II) ions were first reduced to Cu(I) by ethylene glycol. Then it will move up to Cu(II) state by absorbing the atomic oxygen. Here, the CuO is the expected compound to be formed. The $\Delta G_f°$ for Mn_3O_4 is -1288.23 $kJ.mol^{-1}$, whereas $\Delta G_f°$ for CuO is -129.7 $kJ.mol^{-1}$. Here, the $MnCl_2$ and $CuCl_2$ are the reactants, Mn_3O_4 and CuO are their corresponding products. The $\Delta G_f°$ for oxygen scavenging is calculated as,

$\Delta G_f°$ of ($MnCl_2 \rightarrow Mn_3O_4$) = -1288.23 $kJ.mol^{-1}$ - (-440.53 $kJ.mol^{-1}$) = -847.7 $kJ.mol^{-1}$

$\Delta G_f°$ of ($CuCl_2 \rightarrow CuO$) = -129.704 $kJ.mol^{-1}$ - (- 161.92 $kJ.mol^{-1}$) = 32.216 $kJ.mol^{-1}$

The more negative of $\Delta G_f°$ of ($MnCl_2 \rightarrow Mn_3O_4$) indicates that the process of oxygen scavenging is more spontaneous than that observed by using Cu(II) ions. In other words, the tendency to absorb oxygen from the surface of silver seed particles is higher for the Mn(II) ions compared to the Cu(I) ions.

4.4 UV-VIS Absorption Spectroscopy of Synthesised Silver Products
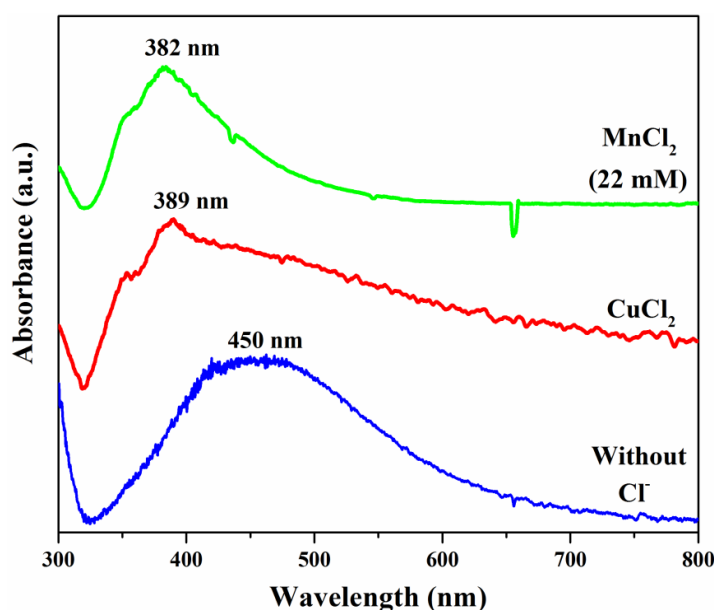
Figure 4.18 UV-VIS absorption spectra of silver products synthesised with three different chloride conditions

Figure 4.18 shows the UV-VIS absorption spectra of the silver particles synthesised without any chloride salt, silver nanowires synthesised with the addition of $CuCl_2$ (22 mM) and $MnCl_2$ (22 mM). The absorption spectrum of silver particles showed a broad absorption peak at 450 nm. The silver nanowires exhibited a predominant peak along with a low-intensity peak. The $CuCl_2$ sample showed maximum absorption at 389 nm while the $MnCl_2$ sample exhibited the maximum absorption at 382 nm. The existence of these observed peaks was due to the surface plasmon resonance (SPR) of silver nanostructures (Ma and Zhan 2014). The SPR peak at 450 nm is attributed to the large particle size of silver (Wiley et al. 2005). However, the maximum absorption was blue-shifted for the nanowires. This is because the surface plasmon resonance becomes dominant in the transverse direction (Ma and Zhan 2014). The blue-shift from 389 nm to 382 nm is attributed to the decrease in the diameter of nanowires from 151 nm to 60 nm (Niu et al. 2018).
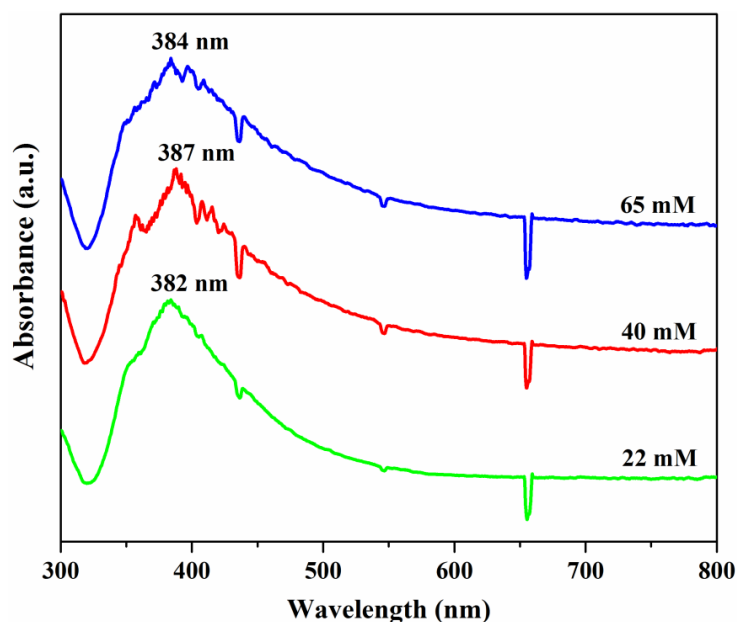
Figure 4.19 UV-VIS absorption spectra of silver nanowires synthesised with the addition of different concentrations of $MnCl_2$

The absorption peak shift was also observed for the silver nanowires synthesised with different $MnCl_2$ concentrations (Fig. 4.19). The 22 mM sample with a mean diameter of 60 nm exhibited the absorption peak at 382 nm. But the absorption was red-shifted to 387 nm for the 40 mM sample because of its larger diameter of 80 nm. This red-shift

of SPR peak with respect to increased diameter was attributed to the inhomogeneous polarization caused by multipolar oscillations in silver nanowires due to the large diameter (Ma and Zhan 2014) (Amendola et al. 2017). The absorption peak was blue-shifted to 384 nm for the 65 mM sample due to decrease in the diameter to 71 nm from 80 nm. The change in the absorption wavelength corresponding to the concentration of the $MnCl_2$ again confirms the influence of Mn(II) ions on the diameter of the silver nanowires (Ma and Zhan 2014) (Niu et al. 2018).

4.5 Transmission electron microscopy of synthesised silver products
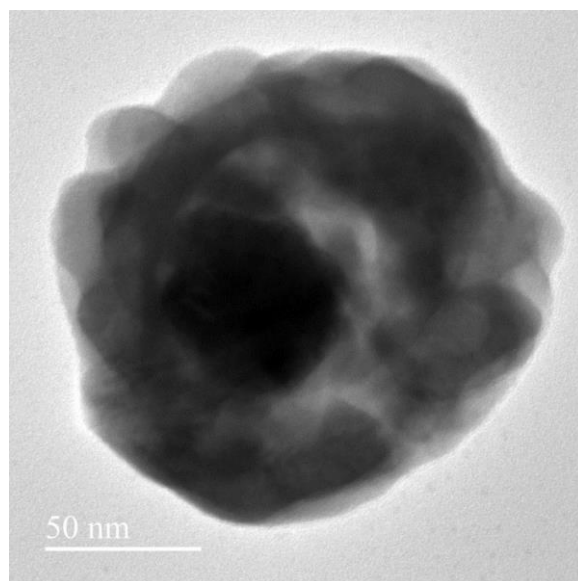
Figure 4.20 TEM micrograph of the Ag nanoparticles synthesised with the addition of no chloride salt

The TEM micrograph of silver nanoparticle synthesised without any chloride addition is shown in Fig. 4.20. The micrograph reveals the spherical-like morphology of this silver nanoparticle. This nanoparticle is, in fact, the aggregation of small silver nanoparticles. The measured size of this aggregated nanoparticle is 160 nm. The TEM result complements the FESEM result to confirm the growth of silver nanoparticles when it was synthesised without the presence of any chloride salts. As mentioned earlier, the rapid reduction of Ag^+ ions to Ag^0 without any buffer phase for the controlled release of silver was the reason behind the growth of silver particles (Coskun et al. 2011).
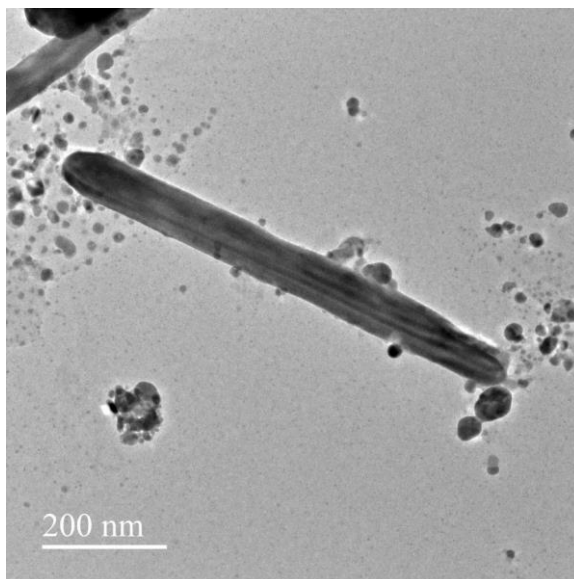
Figure 4.21 TEM micrograph of silver nanorod synthesised with the addition of NaCl
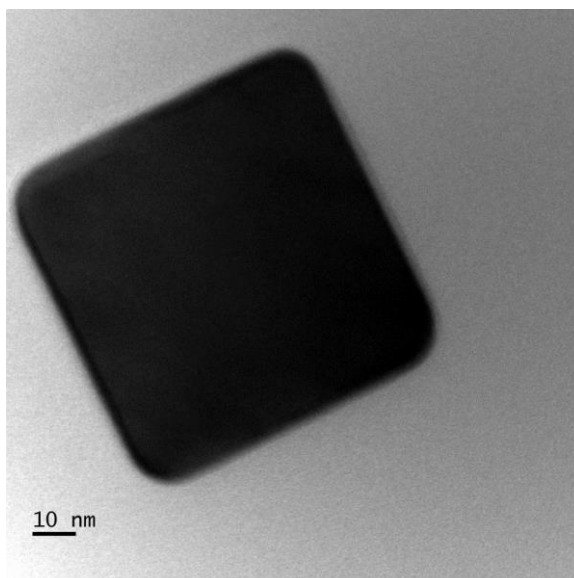
Figure 4.22 TEM micrograph of silver nanocube synthesised with the addition of NaCl
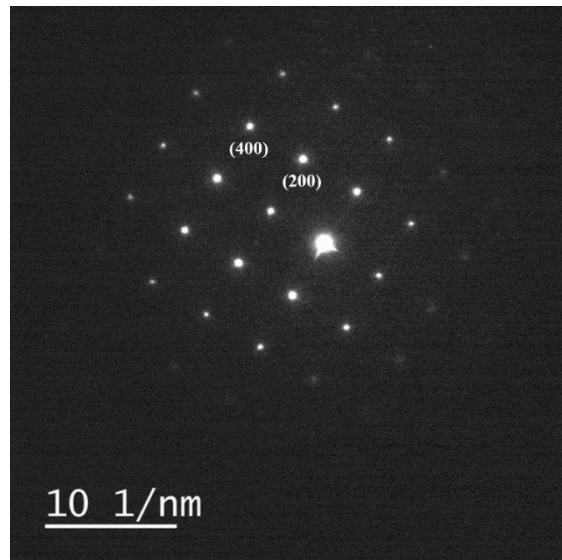
Figure 4.23 The SAED pattern of silver nanocube synthesised with the addition of NaCl

Figure 4.21 shows the TEM micrograph of silver nanorod synthesised with the addition of NaCl. The length and diameter of the nanorods were measured as 790 nm and 77 nm, respectively. The presence of twin boundaries in the nanorod is seen parallel to its axis. When Cl^- ions were introduced through the addition of NaCl, they prevented the formation of aggregated particles and promoted one-dimensional growth (Coskun et al. 2011). But the presence of atomic oxygen hindered the growth of the one-dimensional growth as mentioned earlier. It resulted in the short nanorods. Figure 4.22 shows the TEM micrograph of nanocube produced along with the silver nanorod as a by-product during the synthesis process. It is observed that this nanocube does not show any evidence for the presence of the twins in its structure (Wiley et al. 2005). The corresponding SAED pattern of this nanocube (Fig. 4.23) confirms the absence of twins. From the above observation, it is concluded that the oxidative etching of the twins was the reason for the growth of short nanorods and nanocubes.
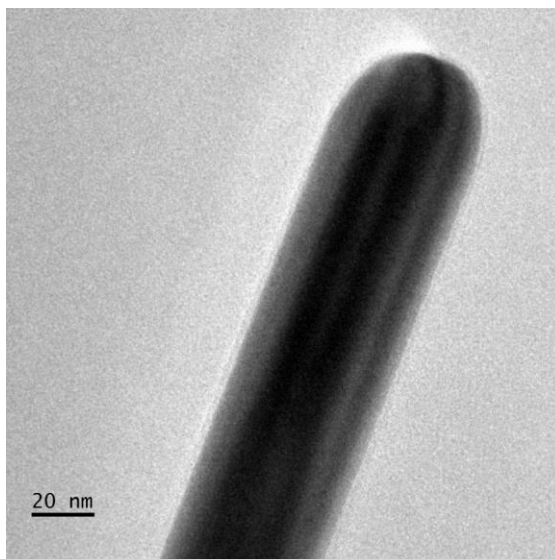
Figure 4.24 TEM micrograph of silver nanowire synthesised with 22 mM of MnCl$_2$
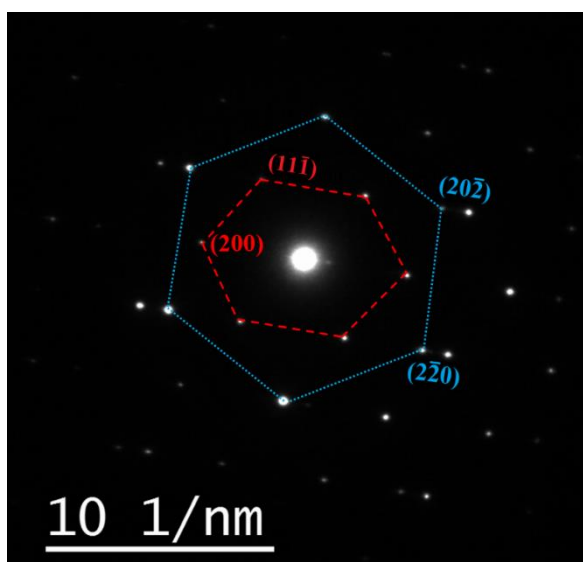
Figure 4.25 The SAED pattern of silver nanowire synthesised with 22 mM of MnCl$_2$

Fig. 4.24 shows the TEM micrograph of silver nanowire synthesised with the addition of 22 mM MnCl$_2$. The diameter of the nanowire was measured as 50 nm. The micrograph reveals the presence of the twin boundaries along the longitudinal axis of the nanowire. These twin boundaries are the highest energy sites that attract the new incoming silver species to grow on them during the synthesis process. This selective growth of silver on the twin boundaries leads to one-dimensionally grown nanowires.

The selected area electron diffraction (SAED) pattern shown in Fig. 4.25 also confirmed the presence of twins in the silver nanowire. Two different sets of diffraction patterns with the zone axis of [011] and [111] were observed. The existence of two sets of diffraction in the SAED pattern is supported by the previous literatures Wang et al. (2016b).

4.6 X-Ray Diffraction Study
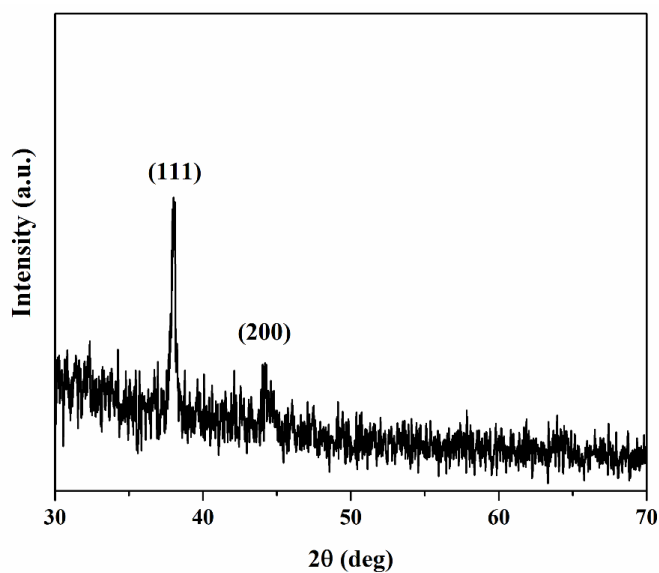
Figure 4.26 XRD pattern of silver nanoparticles synthesised without any chloride salt

Figure 4.26 shows the XRD pattern of silver nanoparticles synthesised without any chloride salt during the synthesis process. The XRD pattern exhibit two peaks which are corresponding to (111) and (200) planes of silver (ICDD 04-0783).
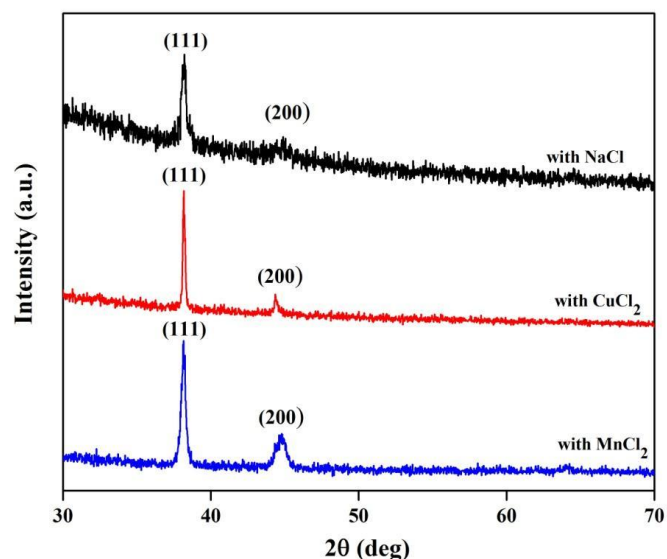
Figure 4.27 XRD pattern of silver nanowires synthesised with the addition of different chloride salts

The XRD patterns of silver nanowires synthesised with the addition of NaCl, CuCl$_2$ and MnCl$_2$ are shown in Fig. 4.27. The XRD patterns of the mentioned three samples show peaks corresponding to (111), (200) planes of silver (ICDD 04-0783). The highest peak intensity of the (111) plane is attributed to the preferred (111) plane growth of silver nanowires.

4.7 Opto-Electric Properties of Silver Nanowires Films

The network of silver nanowires in the fabricated silver nanowires film forms a percolation path for electrical conductivity through the junctions of nanowires. Although the wire-wire junctions help to form the percolation path, the electrical conductivity of the silver nanowires film is dropped by the resistance at the wire-wire junctions (Langley et al. 2014). In other words, the sheet resistance of the film is increased with the increase in wire-wire junctions. This is the reason for the importance of using longer silver nanowires with a high aspect ratio. The electrical percolation is achieved with fewer wire-wire junctions by using longer nanowires (Madeira et al. 2020). Thus, the sheet resistance of the film can be reduced. The encapsulation of silver nanowires with PVP molecules is another factor that increases the sheet resistance (Langley et al. 2014). The above two problems could be resolved by annealing the

fabricated silver nanowires film. Annealing the films below the fragmentation temperature of silver nanowires leads to melting of PVP molecules from the surface of the silver nanowires and fusing of nanowires at the wire-wire junctions. The resistance at wire-wire junctions is reduced by fusion of nanowires that would reduce the overall sheet resistance of nanowires film (Langley et al. 2014).

The sheet resistance of films fabricated from silver nanowires synthesised with the addition of $MnCl_2$ was measured before and after the annealing process. The fabricated films were subjected to annealing at 165 °C for 30 minutes. The sheet resistance values of the films determined from the four-probe measurement are given in Table 4.1. It is observed that the sheet resistance of the silver nanowires film was reduced significantly after the annealing process.

Table 4.1 Sheet resistance of silver nanowires film: before and after annealing treatment

No. of coating layers	Ag NWs film (22 mM $MnCl_2$)		Ag NWs film (40 mM $MnCl_2$)		Ag NWs film (65 mM $MnCl_2$)	
	R_s (before annealing) Ω/sq	R_s (after annealing) Ω/sq	R_s (before annealing) Ω/sq	R_s (after annealing) Ω/sq	R_s (before annealing), Ω/sq	R_s (after annealing) Ω/sq
4L	2700	485	1900	332	2180	395
5L	55	40	42	29	48	34
6L	38	20	23	11	31	15
7L	22	16	12	7.5	17	11
8L	14	7	10	4	10	5

As high optical transparency and high electrical conductivity are the desirable characteristics of a good transparent conductive electrode, it is imperative to correlate these two factors. The desirable silver nanowires film should have high optical

transmittance at the wavelength of 550 nm ($\%T_{550nm}$) with low sheet resistance (R_s). The '$\%T_{550nm}$' and 'R_s' of the films are changed with the number of silver nanowires coating layers.

Figure 4.28, 4.29 and 4.30 show the UV-VIS transmittance spectra of the films prepared using silver nanowires synthesised with three different concentrations of $MnCl_2$ (22 mM, 40 mM and 65 mM, respectively). The films prepared by using 22 mM, 40 mM and 65 mM samples are named as M22, M40 and M65 respectively. The spray coating method was followed to prepare the multilayer (4L, 5L, 6L, 7L and 8L) silver nanowires films. The density of the silver nanowires in the film was increased with respect to the number of spray-coated silver nanowires layers. It is observed that the optical transparency of the film was decreased with the number of coating layers. The increase in nanowires density in the film caused to decrease in the light transmittance through the films. Nevertheless, the increase in density of nanowires improved the electrical percolation in the film. It is evident from the reduction in sheet resistance of the film with the increasing the number of coating layers of silver nanowires.
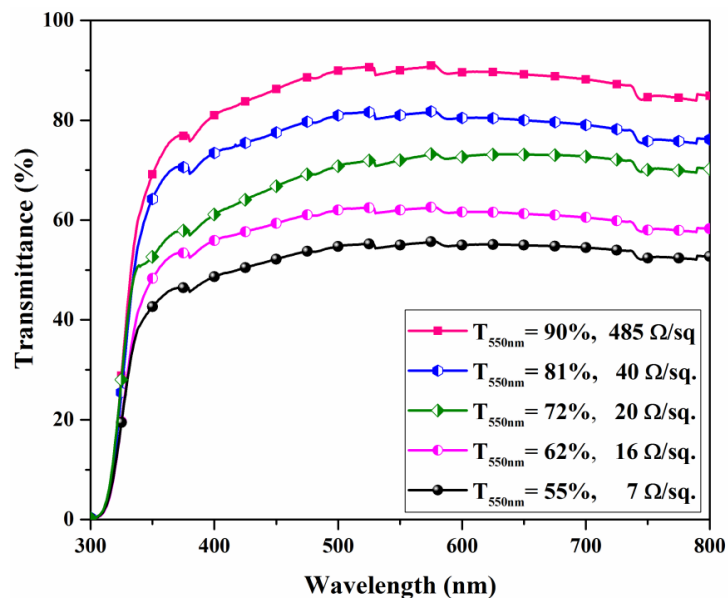
Figure 4.28 Optical transmittance and sheet resistance of M22 silver nanowires films

Figure 4.28 shows the transmittance spectra of M22 silver nanowires films with their corresponding sheet resistance (R_s) values. The transmittance at $\lambda=550$ nm ($\%T_{550 nm}$) and R_s values of 4L, 5L, 6L, 7L and 8L films were determined as 90%, 81%, 72%, 62%,

55% and 485, 40, 20, 16 and 7 Ω/sq, respectively. With high R_s (4L film) of 485 Ω/sq and low %$T_{550\,nm}$ of less than 75%, the films other than 5L are not suitable to be used as TCE. The 5L film is the best TCE among M22 silver nanowires films with the optical transmittance (%$T_{550\,nm}$) of 81% and sheet resistance of 40 Ω/sq.
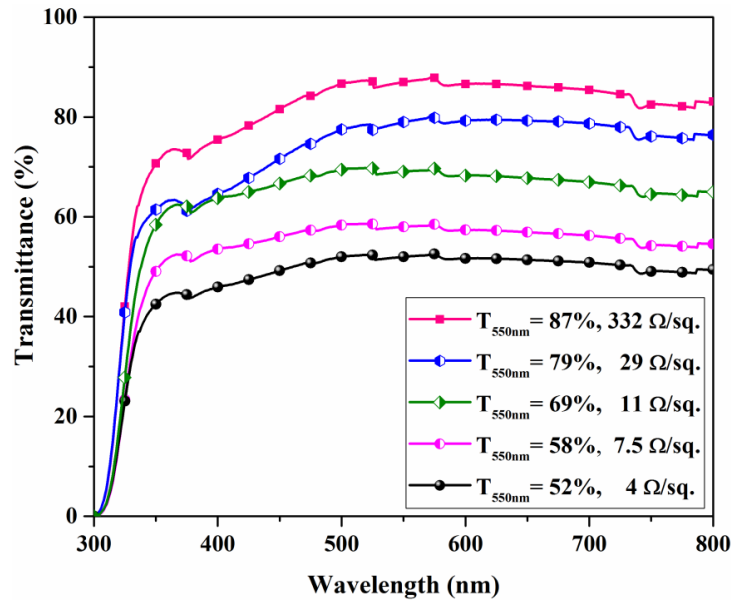
Figure 4.29 Optical transmittance and sheet resistance of M40 silver nanowires films

Fig. 4.29 shows the opto-electrical characteristics of M40 (40 mM MnCl$_2$) silver nanowires films. The %$T_{550\,nm}$ and R_s values of 4L, 5L, 6L, 7L and 8L films were determined as 87%, 79%, 69%, 58%, 52% and 332, 29, 11, 7.5 and 4 Ω/sq, respectively. Among all M40 silver nanowires films (4L, 5L, 6L, 7L and 8L), 5L silver nanowires film with %T_{550} =79% and R_s=29 Ω/sq. was acceptable with the balanced transmittance and sheet resistance values.
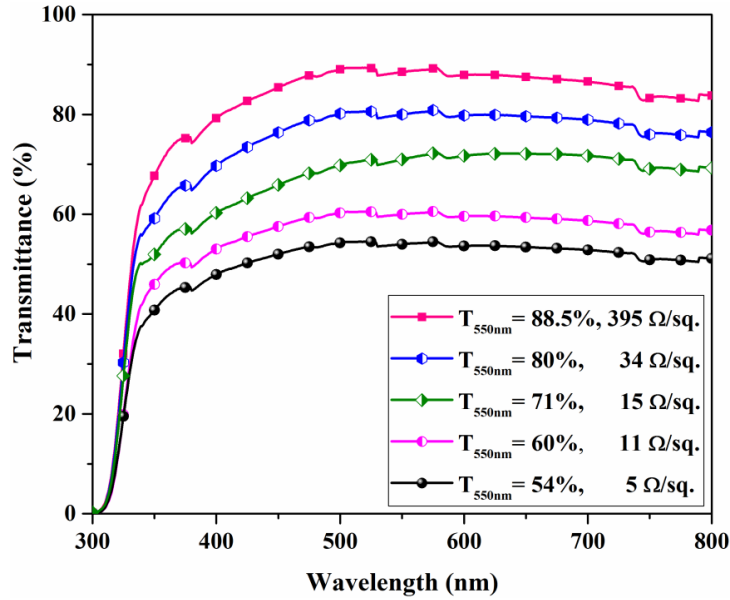
Figure 4.30 Optical transmittance and sheet resistance of M65 silver nanowires films

Fig. 4.30 shows the optical transmittance spectra of M65 silver nanowires film with their corresponding sheet resistance. The $\%T_{550\ nm}$ and R_s values of 4L, 5L, 6L, 7L and 8L films were found to be 88.5%, 80%, 71%, 60%, 54% and 395, 34, 15, 11 and 5 Ω/sq, respectively. Among these films, the 5L silver nanowires film showed acceptable transmittance and sheet resistance values of $\%T_{550\ nm}$=80% and R_s= 34 Ω/sq.

The figure-of-merit (FOM) is the widely accepted quantitative expression that defines the quality of a transparent conductive electrode film. The figure-of-merits (φ_{TC}) is calculated by using the formula given by Haacke (Haacke 1976),

$$\varphi_{TC} = T^{10}/R_s \qquad\qquad (3)$$

The term 'T' and 'R_s' denote the optical transmittance and the sheet resistance of the film, respectively. The FOM values of 5L films from each set of films (M22, M40 and M65) were calculated by using the above formula (1). The calculated FOM values are plotted against their corresponding $\%T_{550nm}$, in Fig. 4.31.

85
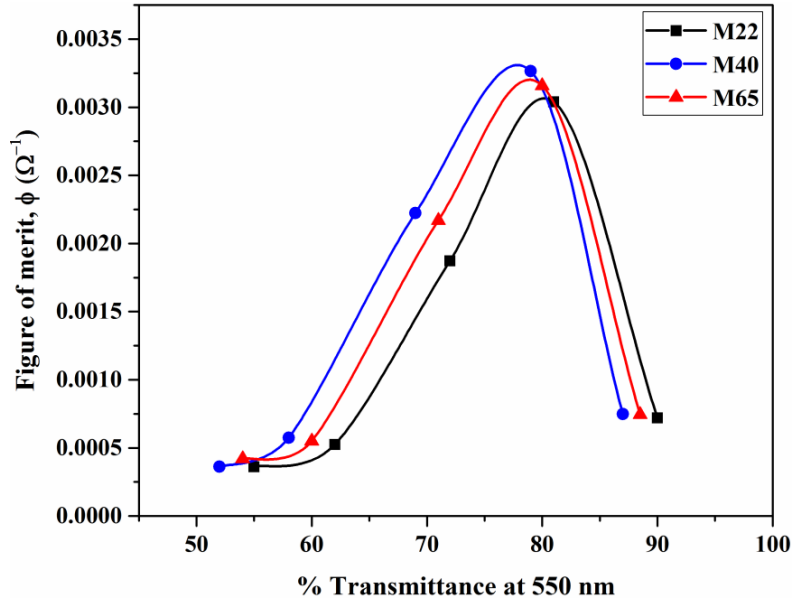
Figure 4.31 Figure of merits of M22, M40 and M65 silver nanowires films

The maximum value of 0.00327 Ω^{-1} was reported for the 5L-M40 film. The FOM value of 5L-M65 and 5L-M22 were reported as 0.00316 Ω^{-1} and 0.00304 Ω^{-1}, respectively. The figure of merit is also represented as the ratio of electrical to optical conductivity (σ_{DC}/σ_{OP}). The σ_{DC}/σ_{OP} ratio was calculated using the formula (Sepulveda-Mora and Cloutier 2012),

$$T = (1 + [188.5/R_s] \cdot (\sigma_{OP}/\sigma_{DC}))^{-2} \qquad (4)$$

The calculated σ_{DC}/σ_{OP} ratio for 5L-M22, 5L-M40 and 5L-M65 are 42.4 Ω^{-1}, 52 Ω^{-1} and 47 Ω^{-1}, respectively. The maximum FOM values calculated from the above two formula belonged to the 5L-M40 film. Although the large diameter factor of silver nanowires (40 mM sample) caused a reduction in the optical transmittance of the M40 sample to 79%, the lowest sheet resistance of 29 Ω/sq was obtained due to the increased length of nanowires. The use of longer silver nanowires improved the percolation path while reducing the wire to wire contact resistance in the film. That eventually leads to high FOM value.
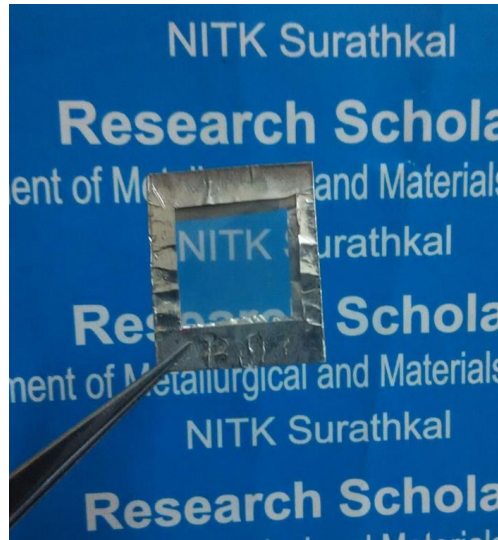
Figure 4.32 Camera image of the silver nanowires film (5L-M40) deposited on a plastic sheet

The camera captured image of the 5L layers coated silver nanowires films (M40) spray-coated on a plastic substrate is shown in Fig. 4.32. The optical transparency of the prepared silver nanowires film can be compared with the background of the film.

4.8 Mechanical Flexibility Study
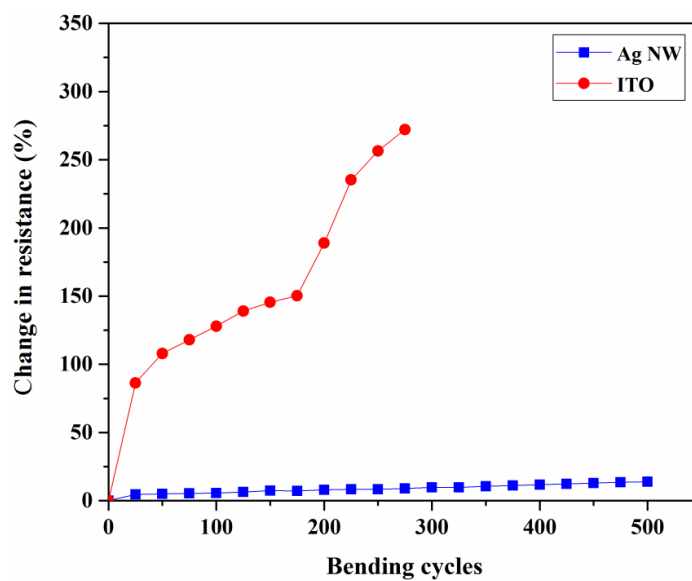
Figure 4.33 Change in the sheet resistance value of silver nanowires film and ITO film against the number of bending cycles

The mechanical flexibility and stability without losing its electrical conductivity are essential properties for a flexible transparent conductive electrode. The silver nanowires spray-coated on a plastic sheet (shown in Fig. 4.32) was subjected to a bending test. A commercial ITO coated on PET sheet (Sigma-Aldrich) was also subjected to the same bending test for the comparison purpose. The percentage change in the sheet resistance of both films with respect to the bending cycles is shown in Fig. 4.33. The sheet resistance of the ITO film was increased up to 275% from its original value after 280 numbers of bending cycles. On the other hand, the silver nanowires film showed better stability with only 14% increase in sheet resistance from its original value after 500 cycles of bending.

4.9 Heater Test

Apart from solar cells and displays, the transparent conducting electrode also finds its application as the transparent heaters. It is used to fabricate anti-fogging and anti-frost front window panels for vehicles and aircraft (Tiwari et al. 2017).

The 5L silver nanowires film of sets M22, M40 and M65 with the sheet resistance of 40, 29 and 34 Ω/sq respectively, were tested for the heater application. The heater test was conducted at the applied voltage of 5, 7 and 10 V. The temperature response to the applied voltage was recorded at the time interval of 15 seconds. The temperature vs. time profiles of M22 silver nanowires film corresponding to applied voltages is shown in Fig. 4.34.
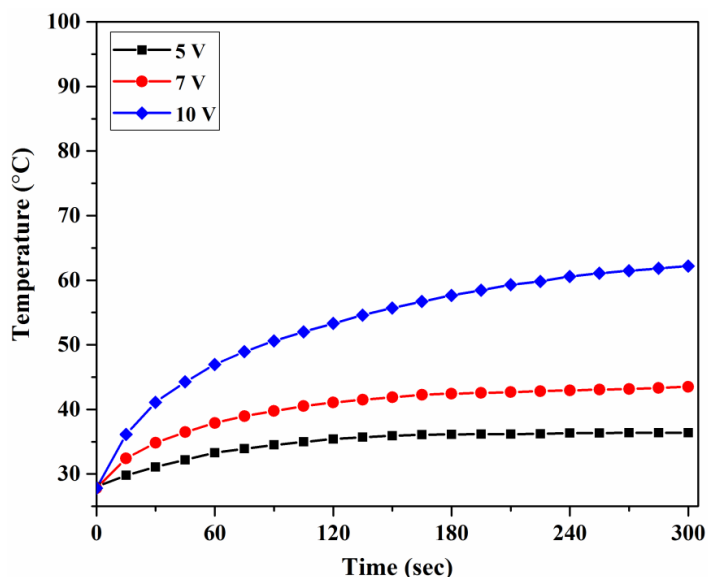
Figure 4.34 Temperature vs. time curve of silver nanowires film synthesised with 22 mM MnCl$_2$ (M22) to the applied voltage values of 5, 7 and 10 V

The 5L film of M22 silver nanowires film was tested for heater application with the applied voltage of 5, 7 and 10 V. The silver nanowires film reached the maximum temperature of 36.5 °C, 43.5 °C and 62 °C for the applied voltage of 5, 7 and 10 V, respectively.
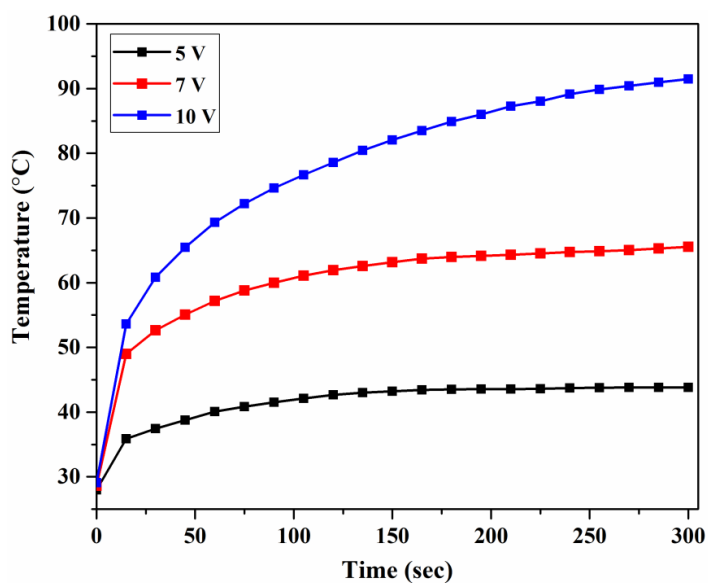
Figure 4.35 Temperature vs. time curve of silver nanowires film synthesised with 40 mM MnCl$_2$ (M40) at applied voltage values of 5, 7 and 10 V

The temperature response of the 5 L film of M40 silver nanowires to the applied voltage are shown in Fig. 4.35. The maximum temperature achieved by the silver nanowires film was 44 °C, 65.5 °C and 90 °C to the applied voltage of 5, 7 and 10 V, respectively. The enhanced heater performance of this M40 silver nanowires film compared to the M22 silver nanowires film is due to the decreased sheet resistance (29 Ω/Sq.) of the film (Park et al. 2019).
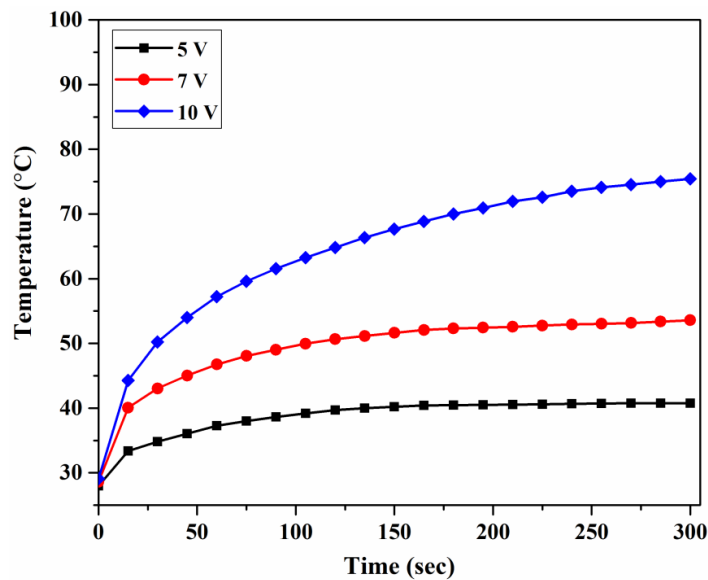
Figure 4.36 Temperature vs. time curve of silver nanowires film synthesised with 65 mM $MnCl_2$ (M65) at applied voltage values of 5, 7 and 10 V

Figure 4.36 shows the temperature response of 5L-M65 silver nanowires film to the applied voltages of 5, 7 and 10 V. The silver nanowires film with the sheet resistance of 34 Ω/sq. achieved the maximum temperature of 41 °C, 53 °C and 74 °C for the applied voltage of 5, 7 and 10 V. The maximum temperature of 74 °C is in between the temperature achieved by the M22 and M40 silver nanowires films. The intermittent sheet resistance value of this film (34 Ω/sq.) was the reason for this temperature value.

In short, the silver nanowires film of R_s=40 Ω/sq attained the maximum temperature of 62 °C in 300 seconds at the applied voltage of 10 V. While the silver nanowires film of 34 Ω/sq reached higher temperature of 74 °C for the same voltage. But the highest temperature of 90 °C was attained by the silver nanowires film of R_s=29 Ω/sq at the voltage of 10 V. It is observed that the maximum temperature achieved by the silver

nanowires film can be increased by increasing the applied voltage and time of voltage supply. Also, it is observed that the reduction in sheet resistance improves the heater performance of the film (Park et al. 2019). The influence of sheet resistance on heat energy produced is related by Joule's law as given below (Ha and Jo 2017),

$$Q = (V^2/R).t \qquad\qquad (5)$$

Where 'Q' is heat generated, 'V' represents the applied voltage value, 'R' is sheet resistance and 't' is time. The heat generated by the film is inversely proportional to the sheet resistance of the film.

4.10 Summary

The silver nanowires were synthesised by the polyol method. It is understood that the presence of chloride ions is essential to form the AgCl buffer phase that promotes the one-dimensional growth of silver nanostructures. The manganese(II) ions were used during the synthesis as the oxygen scavenger as the alternative to copper ions. It is proved that the Mn(II) ions were effective in removing the atomic oxygen from the surface of the silver to enhance the growth of nanowires. The silver nanowires synthesised with the addition of $MnCl_2$ showed a smaller diameter of 60 nm than the silver nanowires produced with $CuCl_2$ (151 nm). The optimum condition of 40 mM $MnCl_2$ yielded long silver nanowires with a small diameter compared to the $CuCl_2$ condition. The silver nanowires film fabricated using 40 mM $MnCl_2$ silver nanowires showed the optical transmittance ($\%T_{550\ nm}$) of 79% and R_s of 29 Ω/sq. The bending test result shows that the flexible transparent conductive film of silver nanowires coated on the plastic sheet is mechanically stable. Unlike commercial ITO film, the sheet resistance of the nanowires film increased little after 500 cycles of bending. The heater test showed that the silver nanowires film could reach a temperature of 90 °C for the applied voltage of 10 V.

Publications from chapter 4

1. Prabukumar, C., and Bhat, K. U. (2018). Mater. Today: Proc., 5(10), 22487-22493.

2. Prabukumar, C., and Bhat, K. U. (2020). Electron. Mater. Lett., 16(3), 264-275.

CHAPTER 5

SYNTHESIS AND CHARACTERIZATION OF MoS$_2$ NANOSHEETS

This chapter presents the exfoliation of MoS$_2$ nanosheets by ultrasonication-assisted liquid phase exfoliation method. The exfoliated nanosheets are characterized by using electron microscopy (FESEM, TEM), X-ray diffractometry, Raman spectroscopy and BET analysis.

5.1 Exfoliation of MoS$_2$ Nanosheets
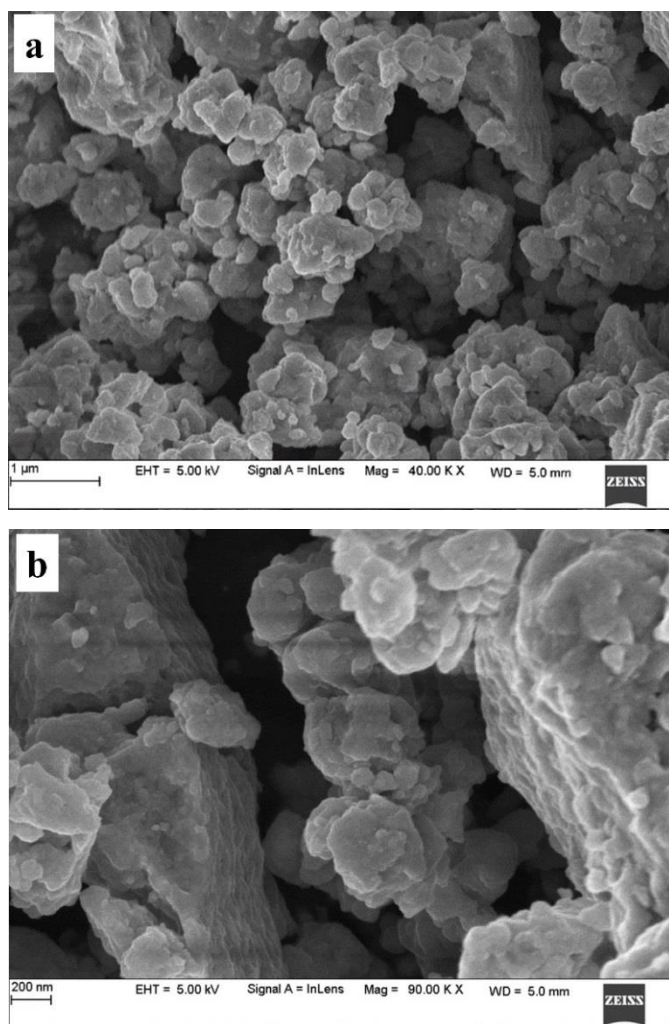
Figure 5.1 a), b) FESEM micrographs of the bulk MoS$_2$ powder

Figure 5.1 show the FESEM micrograph of the bulk MoS_2 powder. It is observed that the bulk powder consisted of several layers of the MoS_2 stacked one above the other. The size of the bulk MoS_2 powder particles was varying from 150 nm to more than 1 µm. The dimensions of the particles were measured using ImageJ software
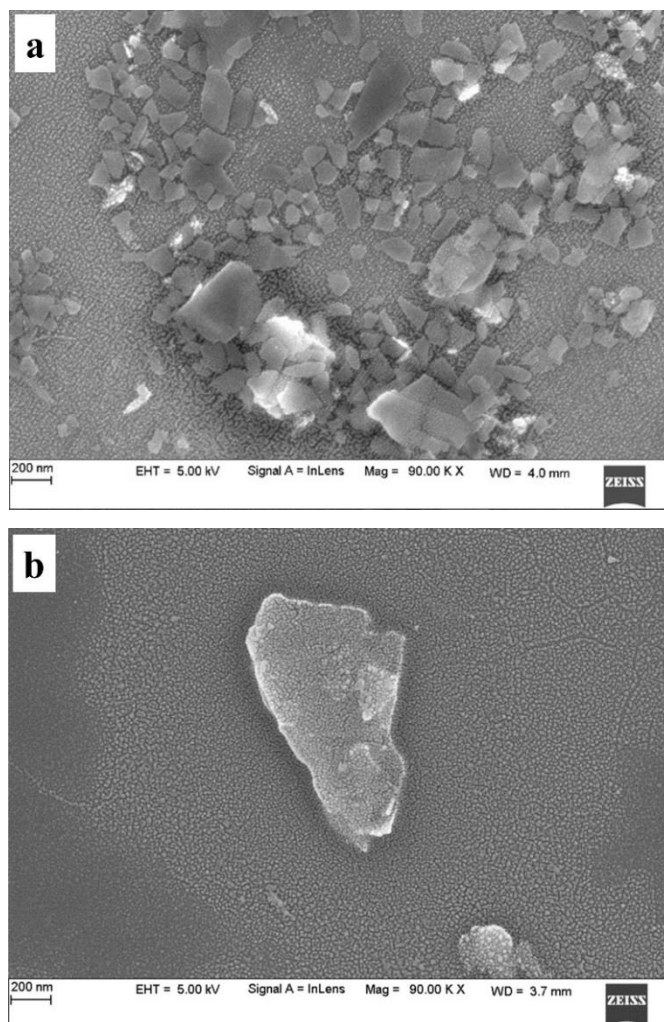
Figure 5.2 a), b) FESEM micrographs of the exfoliated MoS_2 nanosheets

Figure 5.2 show the FESEM micrographs of the exfoliated MoS_2 nanosheets. The FESEM micrograph of exfoliated nanosheets revealed that the thicker bulk MoS_2 powders were reduced into thin nanosheets. The MoS_2 layers were peeled off by the shear force induced from the ultrasonication process. The van der Waals force of interactions that held the MoS_2 layers together was overcome by this shear force (Gupta et al. 2016). That helped in the exfoliation process of MoS_2 nanosheets. The PVP

molecules played a vital role to passivate the exfoliated nanosheets to prevent them from restacking (Liu et al. 2012).
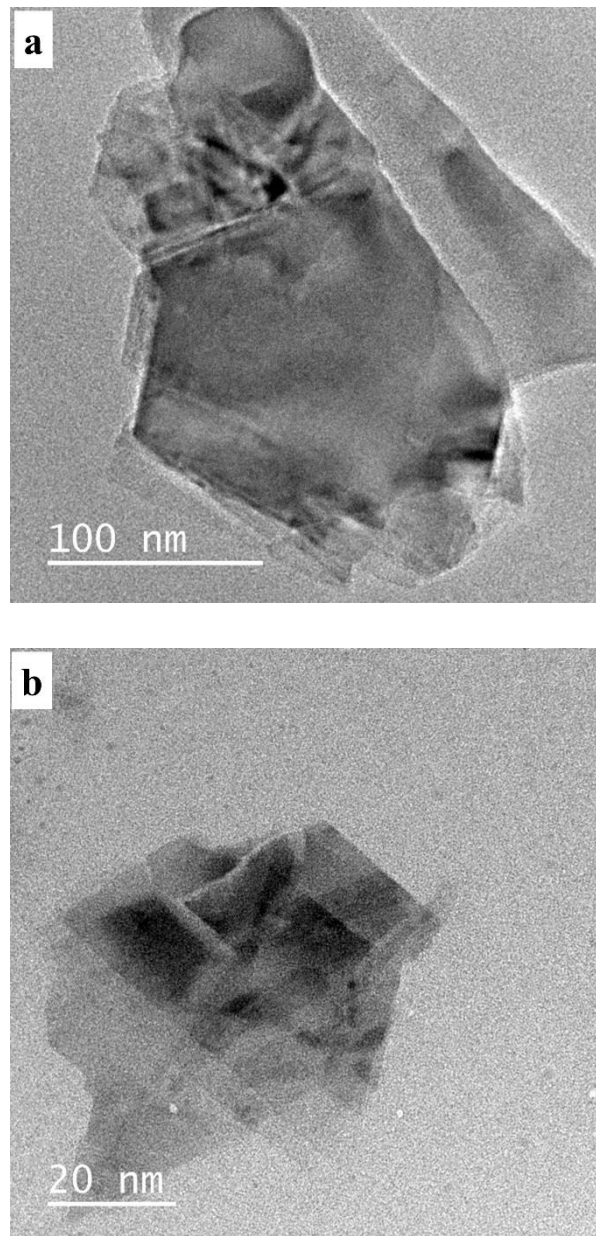
Figure 5.3 a), b) TEM micrographs of the exfoliated MoS_2 nanosheets

Figure 5.3 shows the TEM micrograph of the exfoliated MoS_2 nanosheets. It is observed that the exfoliated MoS_2 nanosheets consist of only a few layers. The size of the MoS_2 nanosheets was also reduced after the ultrasonic exfoliation. The size of the nanosheets is measured to be in the range of 60 nm to 400 nm.
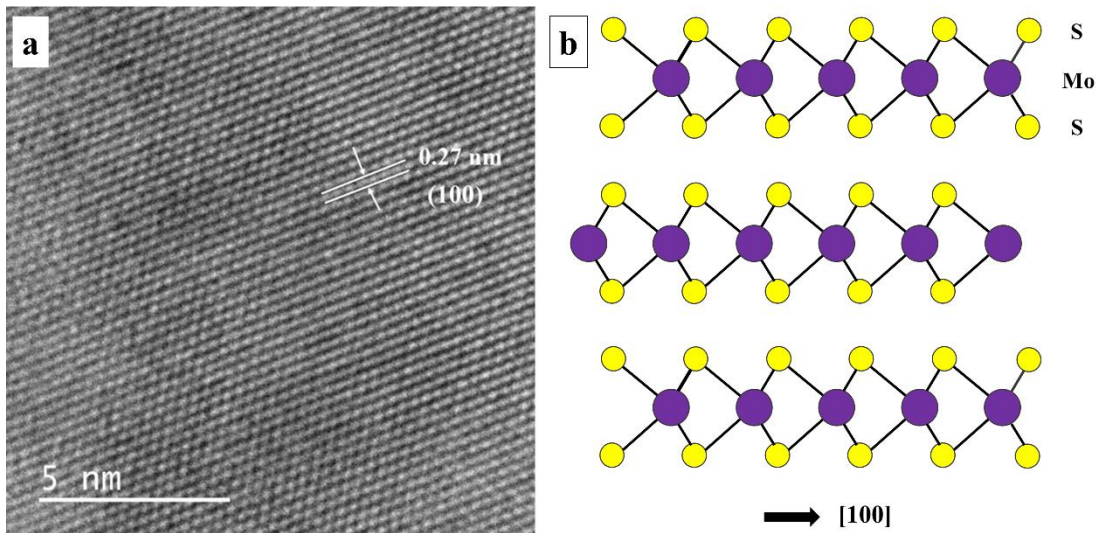
Figure 5.4 a) Lattice image of the MoS$_2$ nanosheet, b) Crystal structure of MoS$_2$
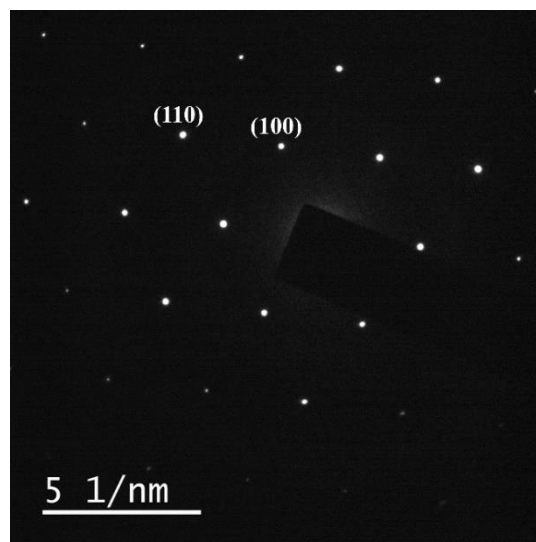
Figure 5.5 SAED pattern of the exfoliated MoS$_2$ nanosheet

The lattice distance of 0.27 nm is measured from the high-resolution TEM micrograph shown in Fig. 5.4. It is attributed to the (100) plane of MoS$_2$. Figure 5.5 shows the SAED pattern of the MoS$_2$ nanosheet. The SAED pattern reveals the hexagonal lattice structure of the MoS$_2$ nanosheets.

5.2 X-Ray Diffractrometry
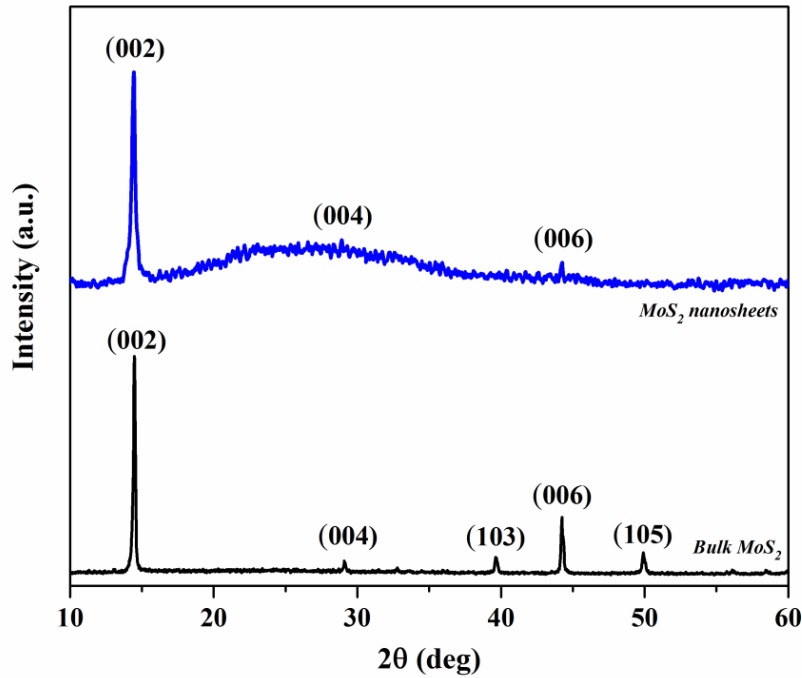
Figure 5.6 XRD patterns of the bulk MoS_2 powder and the exfoliated MoS_2 nanosheets

The XRD patterns of bulk MoS_2 powder and exfoliated MoS_2 nanosheets are shown in Fig. 5.6. The XRD pattern of both materials belongs to the Molybdenite-2H phase (ICDD #006-0097). The maximum intensity was observed for the peak belonged to the (002) plane for both materials. But the peaks of (103) and (105) planes that appeared for the bulk powder were absent for the exfoliated nanosheets. Also, the peak of (002) plane was broader for the exfoliated nanosheets compared to the bulk powder. This indicates the reduction in the crystal thickness of MoS_2 after the exfoliation process (Wang et al. 2015). The broad amorphous peak appeared between 20° to 35° was due to the glass substrate.

The texture coefficient was calculated for the bulk and exfoliated MoS_2 from their corresponding XRD data. The texture coefficient (T.C) was calculated by using the following formula (Sneha et al. 2017),

$$T.C_{(hkl)} = \frac{I_{(hkl)}}{I_{(002)} + I_{(004)} + I_{(103)} + I_{(006)} + I_{(105)}}$$

96

Here, (hkl) represents (002) or (004) or (103) or (006) or (105) planes. 'I' represents the intensity of the individual XRD peaks.
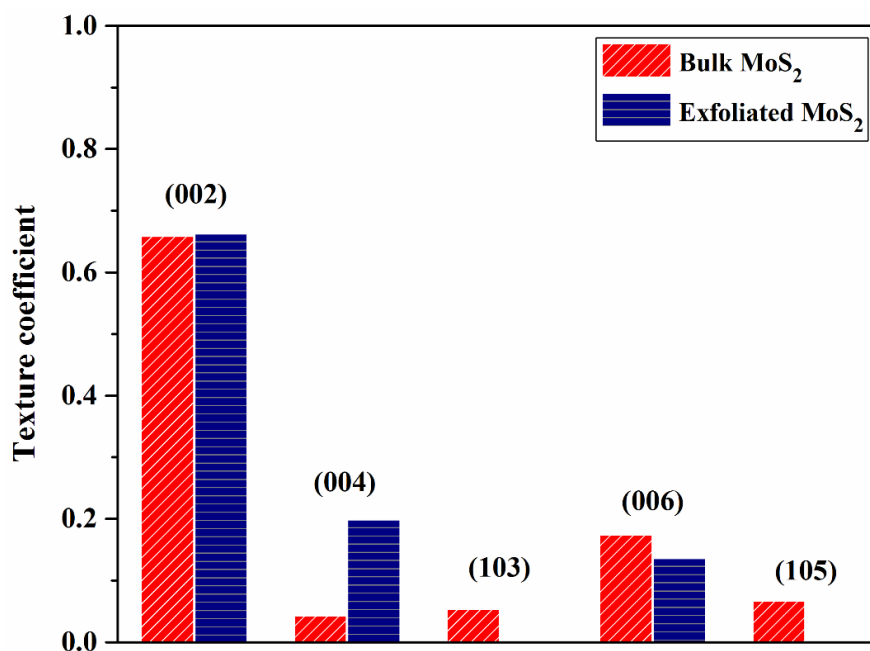
Figure 5.7 Texture coefficient of the bulk MoS_2 powder and the exfoliated MoS_2 nanosheets

Figure 5.7 shows the texture coefficient of the bulk MoS_2 powder and the exfoliated MoS_2 nanosheets. In the case of bulk MoS_2, it is noted that the texture coefficient of planes (002), (004), (103), (105) and (006) is 0.66, 0.044, 0.054, 0.175 and 0.068, respectively. For MoS_2 nanosheets, the texture coefficient for planes (002), (004) and (006) was calculated as 0.67, 0.2 and 0.14, respectively. The texture coefficient for (103) and (105) planes are negligible since the XRD peaks were not observed for these planes. The texture coefficient of (002) and (004) planes was increased after the exfoliation process. The absence of peaks belonged to (103) and (105) planes for the exfoliated MoS_2 nanosheets increased the texture coefficient values for (002) planes.

5.3 Raman Spectroscopy
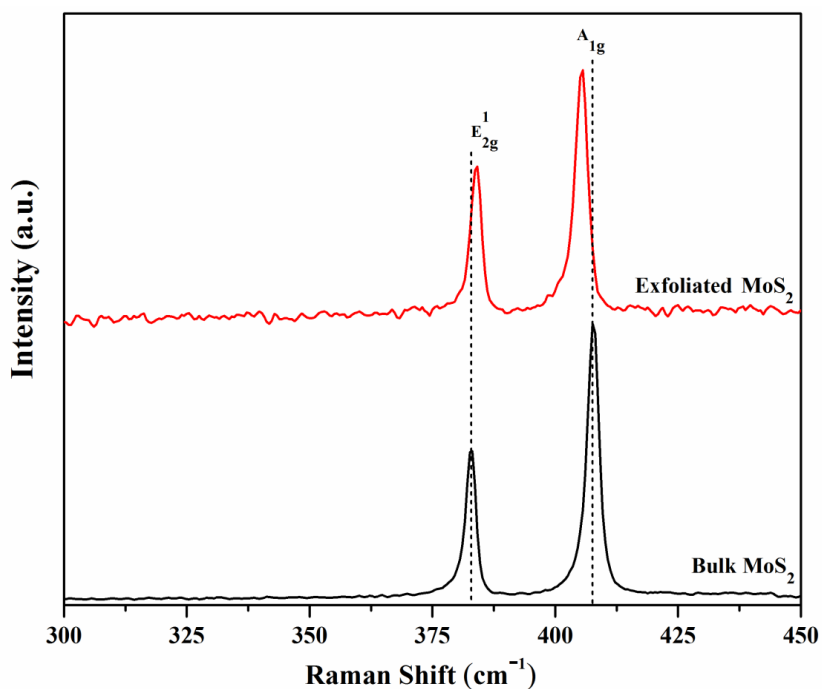
Figure 5.8 Raman spectra of bulk MoS_2 powder and exfoliated MoS_2 nanosheets

The Raman spectra of bulk MoS_2 and MoS_2 nanosheets are shown in Fig. 5.8. The characteristics Raman vibration peaks of E^1_{2g} and A_{1g} for bulk MoS_2 are observed at 383 cm^{-1} and 407 cm^{-1}, respectively (Rao et al. 2017). When the thickness of the MoS_2 sheet decreases, the E^1_{2g} peak belonged to the in-plane sulfur-molybdenum vibration shifts to a higher frequency, whereas the A_{1g} peak belonged to the out-plane sulfur vibration shifts to lower frequency (Rao et al. 2017). The exfoliated MoS_2 nanosheets exhibited E^1_{2g} and A_{1g} peaks at 384 cm^{-1} and 405.5 cm^{-1}, respectively. The frequency gap between two Raman peaks of the exfoliated MoS_2 nanosheets was reduced to 21.5 cm^{-1} from 24 cm^{-1}. This is the indication that the bulk MoS_2 was exfoliated to nanosheets with few layers thickness (Tsai et al. 2014).

5.4 Specific Surface Area Analysis
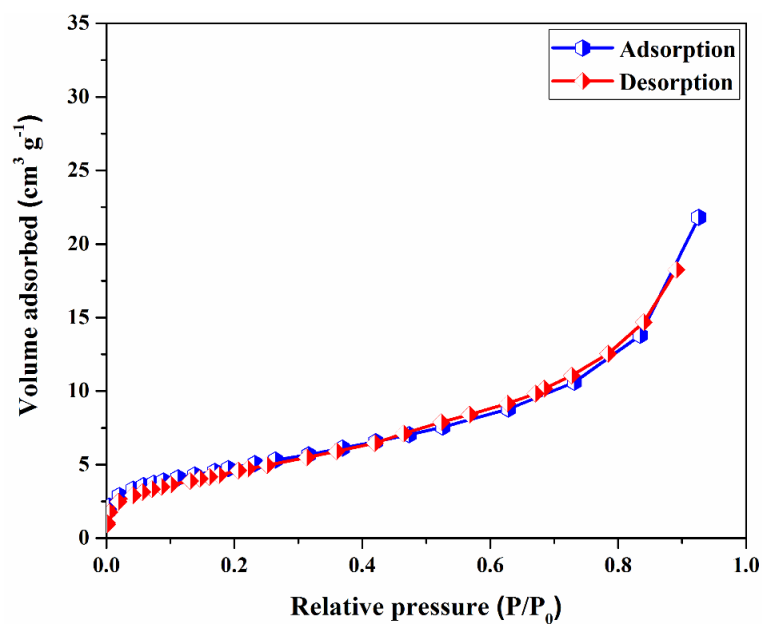
Figure 5.9 Nitrogen adsorption-desorption curve of MoS_2 nanosheets
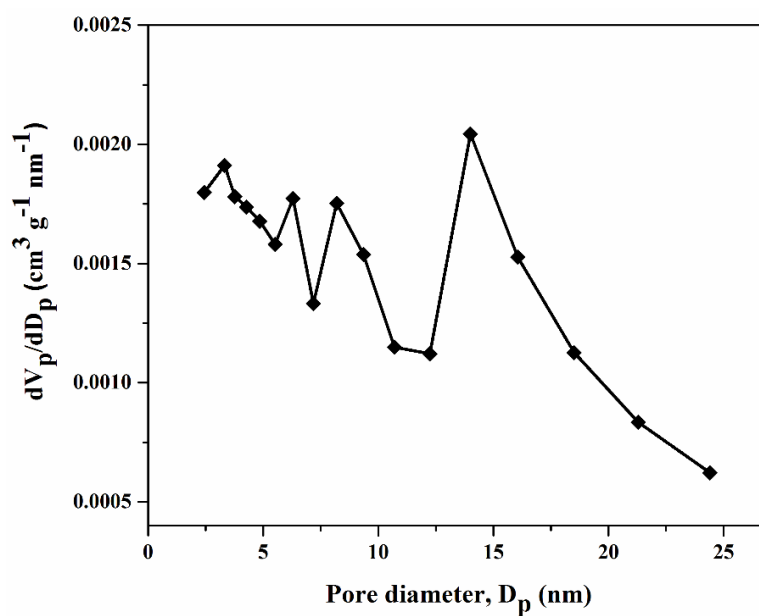
Figure 5.10 Pore size distribution of MoS_2 nanosheets

Figure 5.9 shows the Nitrogen adsorption-desorption curve of exfoliated MoS_2 nanosheets. The adsorption-desorption isotherm with a small hysteresis loop indicates that the isotherm is a type IV isotherm defined by the IUPAC (Fan et al. 2015). The

pore size distribution curve shows (Fig. 5.10) the peaks at the pore size of 6.2 nm, 8.2 nm and 14 nm with the mean pore size of 7.7 nm. This indicates the mesoporous nature of the dried MoS_2 nanosheets powder (Fan et al. 2015). The specific surface area (S_a) of the MoS_2 nanosheets measured by the BET method was 17.5 m^2 g^{-1}. This S_a value of MoS_2 nanosheets was marginally larger than the previously reported values (Fan et al. 2015) (Qiao et al. 2016). The MoS_2 nanosheets with a high specific surface area are crucial to increase the specific capacity when they are used for energy storage applications.

5.5 Summary

The MoS_2 nanosheets were exfoliated via ultrasonication-assisted liquid phase exfoliation method in the presence of PVP. The shear forces and the mechanical agitation induced by the ultrasonication peeled off the bulk MoS_2 powder into MoS_2 nanosheets. The stability of the exfoliated nanosheets were maintained by the dissolved PVP molecules. The exfoliated MoS_2 nanosheets remained suspenen in the dispersion with minimum precipitation at the bottom of the vial after a week time. The FESEM and TEM characterizations manifested that the exfoliated MoS_2 contained few layers of nanosheets. It was confirmed by the Raman spectroscopy results. The XRD analysis established the nature of the exfoliated nanosheets as MoS_2. The exfoliated MoS_2 nanosheets showed a good specific surface area of 17 m^2 g^{-1}.

CHAPTER 6

PREPARATION AND CHARACTERIZATION OF MoS$_2$-SnO$_2$ NANOCOMPOSITE FOR THE SUPERCAPACITOR APPLICATION

The present chapter discusses the synthesis of SnO$_2$ nanoparticles, preparation of MoS$_2$-SnO$_2$ nanocomposite and their various materials characterization, such as FESEM, TEM, particle size analysis, XRD and XPS. The electrochemical characterization of MoS$_2$-SnO$_2$ nanocomposite is also discussed in this chapter.

6.1 Preparation and Characterization of MoS$_2$-SnO$_2$ Nanocomposite
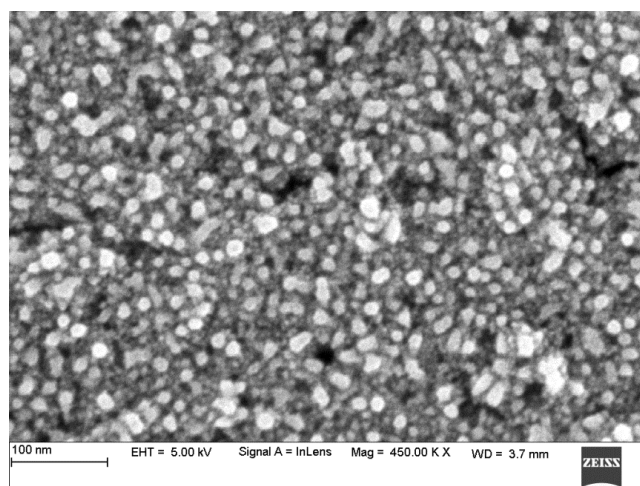
Figure 6.1 FESEM micrograph of the SnO$_2$ nanoparticles

The FESEM micrograph of synthesised SnO$_2$ nanoparticles is shown in Fig. 6.1. It is observed that the synthesised SnO$_2$ nanoparticles have spherical-like morphology. The size of the synthesised nanoparticles was in the range of 10-35 nm. The TEM micrographs of the synthesized SnO$_2$ nanoparticles showed in Fig. 6.2 affirm the spherical-like morphology of the synthesised product. The lattice distances of 0.34 nm and 0.26 nm were measured from the TEM micrograph (Fig. 6.2b). There were belonged to the (110) and (101) planes of SnO$_2$, respectively.
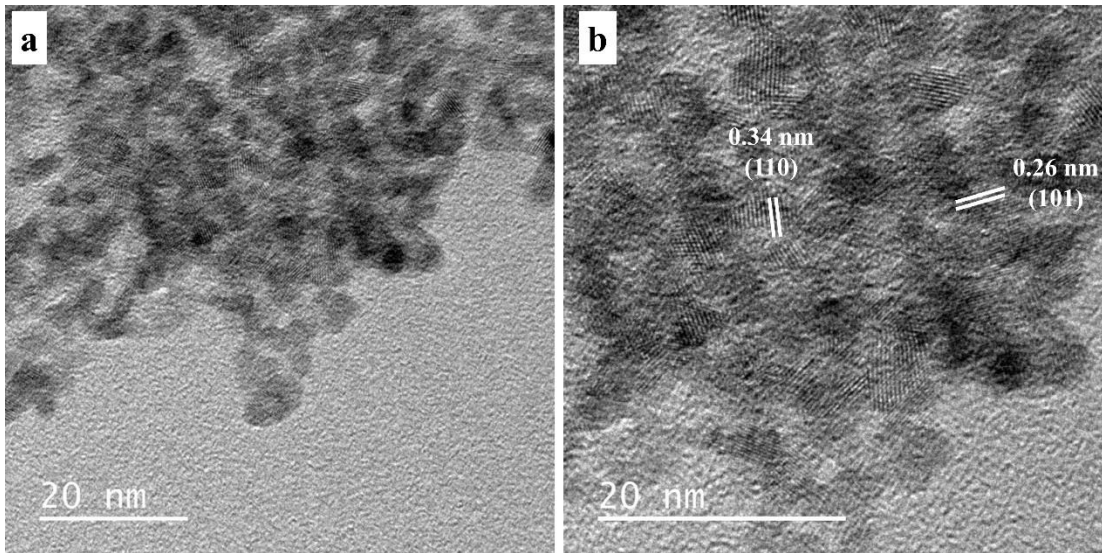
Figure 6.2 TEM micrographs of the SnO$_2$ nanoparticles
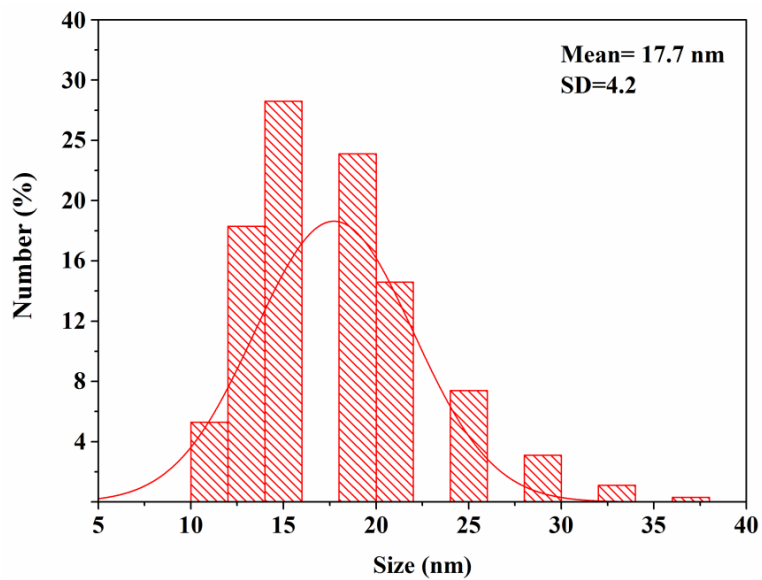
Figure 6.3 Particle size distribution of the SnO$_2$ nanoparticles

Figure 6.3 shows the particle size distribution chart of the SnO$_2$ nanoparticles obtained from the particle analysis test. It is observed that the average size of the synthesised SnO$_2$ nanoparticles was measured as 17.7 nm (standard deviation= 4.2). Almost 90%

of the particles fall in size range of 10-21 nm, while the rest of the particles fall in the size range of 25-37 nm.
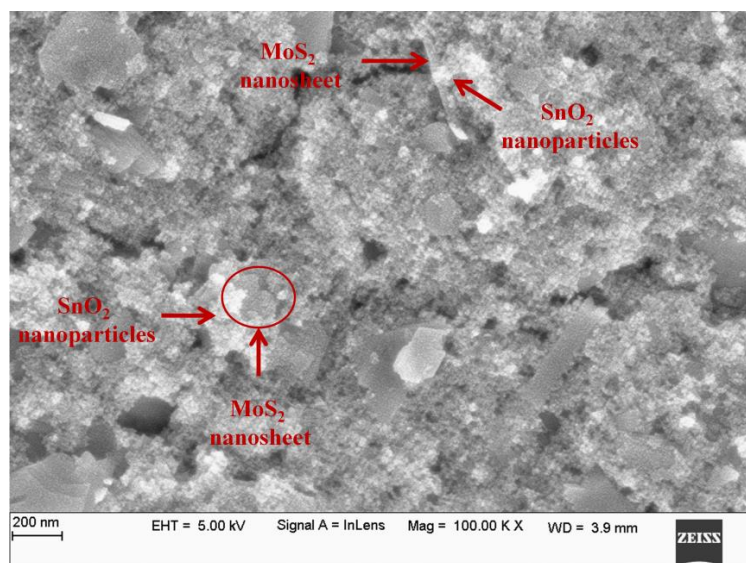
Figure 6.4 FESEM micrograph of the MoS_2-SnO_2 nanocomposite

Figure 6.4 shows the FESEM micrograph of the MoS_2-SnO_2 nanocomposite prepared by the ligand exchange process. The MoS_2 nanosheets exfoliated in the presence of PVP were added to the SnO_2 nanoparticles. The ammonium ions coordinated with SnO_2 nanoparticles replaced the PVP molecules attached with the surface of MoS_2 nanosheets. Thus, the SnO_2 nanoparticles were functionalized onto the surface of the exfoliated MoS_2 nanosheets. The SnO_2 nanoparticles were firmly attached to the surface of the MoS_2 nanosheets. Figure 6.5 shows the schematic diagram explaining the functionalization of MoS_2 nanosheets with SnO_2 nanoparticles by the ligand exchange process.

A thin layer of PVP molecules, from the exfoliation step, would still present onto the surface of the MoS_2 nanosheets even after the washing process because of C-S and O-S bonding between PVP and MoS_2 (Liu et al. 2018). Also, this PVP ligand attached with MoS_2 nanosheets kept nanosheets separated from each other. On the other hand, ammonium ions from ammonium salts coordinated with the SnO_2 nanoparticles during the synthesis process. These ammonium ions act as the surfactant to control the growth of the nanoparticles (Bob et al. 2016).
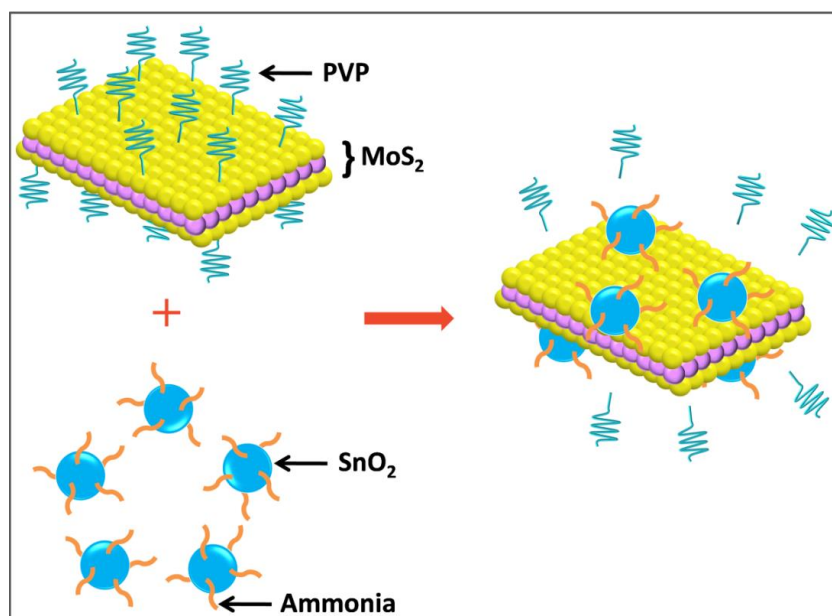
Figure 6.5 Schematic diagram explains the functionalization of MoS_2 nanosheets with SnO_2 nanoparticles

When the MoS_2 nanosheets are added into SnO_2 nanoparticles (Fig. 3.7), the ammonium ions attached with the SnO_2 nanoparticles strip off the PVP molecules from the surface of the MoS_2 nanosheets. Subsequently, the vacant sites left by the stripped PVP molecules were occupied by the SnO_2 nanoparticles. The ammonium ions present over the SnO_2 nanoparticles would help them to anchor onto the surface of the MoS_2 nanosheets (Bob et al. 2016). Likewise, the SnO_2 nanoparticles were decorated or functionalized on the surface of the MoS_2 nanosheets. Bob et al. (2016) also reported this ligand exchange process to deposit SnO_2 nanoparticles on the silver nanowires surface. When mixing the dispersion of silver nanowires and SnO_2 nanoparticles together, the SnO_2 nanoparticles get coated on the silver nanowires by stripping and replacing the PVP molecules from the nanowires through ammonia ions.

This functionalization process by exchanging the ligands is energy efficient compared to the hydrothermal method which involves high temperature and pressure (Ren et al. 2015). Once the PVP molecules were replaced by SnO_2 nanoparticles on the MoS_2 surface, the MoS_2-SnO_2 nanocomposite started to settle down as the precipitate (Fig. 3.7; Chapter 3). After removing the supernatant containing PVP molecules, the obtained residue was used for further studies.
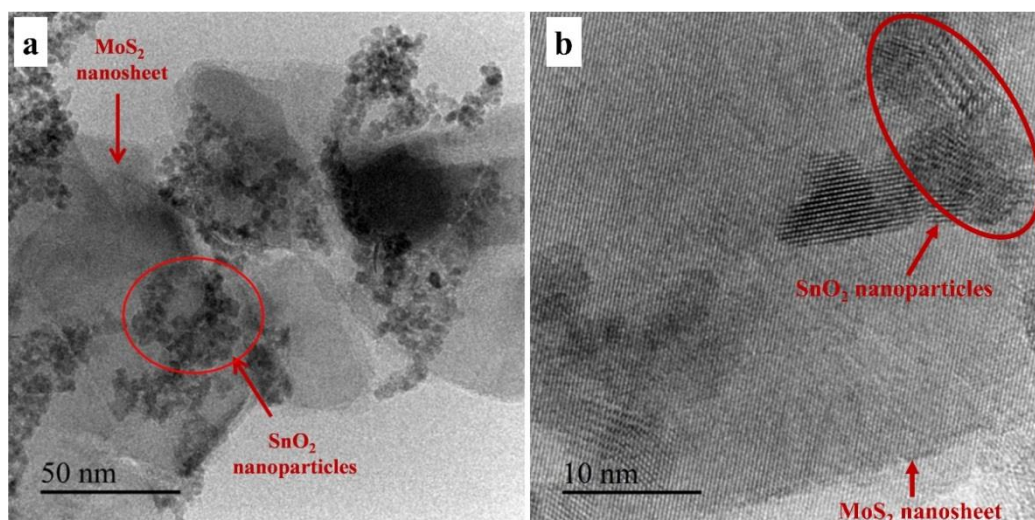
Figure 6.6 TEM micrographs of the MoS$_2$-SnO$_2$ nanocomposite

Figure 6.6 shows the TEM micrographs of the MoS$_2$-SnO$_2$ nanocomposite prepared by the ligand exchange process. The SnO$_2$ nanoparticles could be seen functionalized on the surface of the MoS$_2$ nanosheets. The MoS$_2$ nanosheets can act as the bridge between the SnO$_2$ nanoparticles.
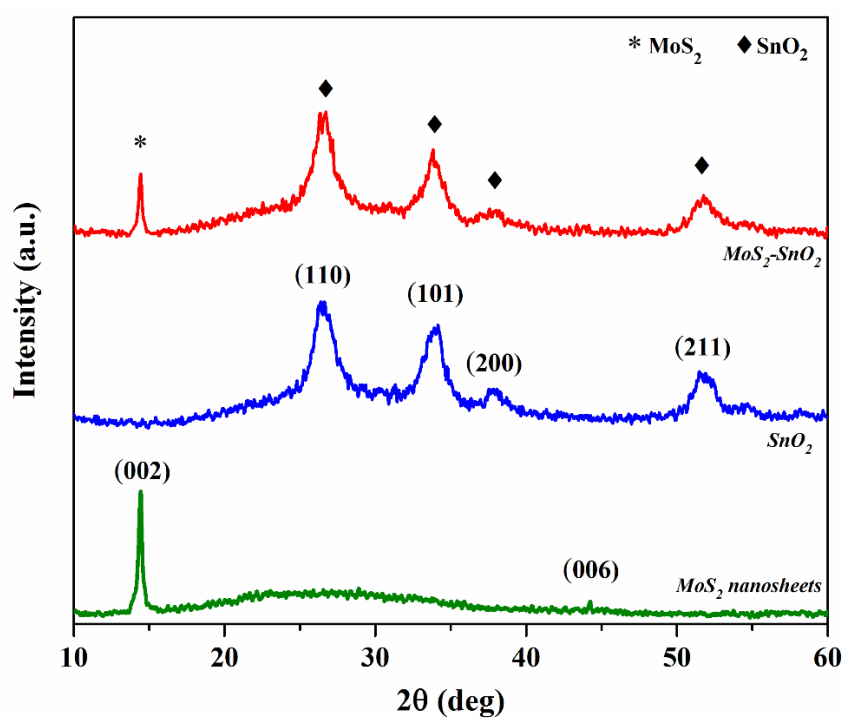
Figure 6.7 XRD patterns of the MoS$_2$ nanosheets, SnO$_2$ nanoparticles and MoS$_2$-SnO$_2$ nanocomposite

Figure 6.7 shows the XRD patterns of the SnO_2 nanoparticles and MoS_2-SnO_2 nanocomposite along with the MoS_2 nanosheets. Three peaks were observed at angles 26.2°, 33.8° and 51.2° for SnO_2 nanoparticles which are attributed to the planes (110), (101) and (211), respectively, of SnO_2 (Cassiterite, ICDD #041-1445). The XRD pattern of MoS_2-SnO_2 nanocomposite exhibited the peaks of both SnO_2 and MoS_2 phases.
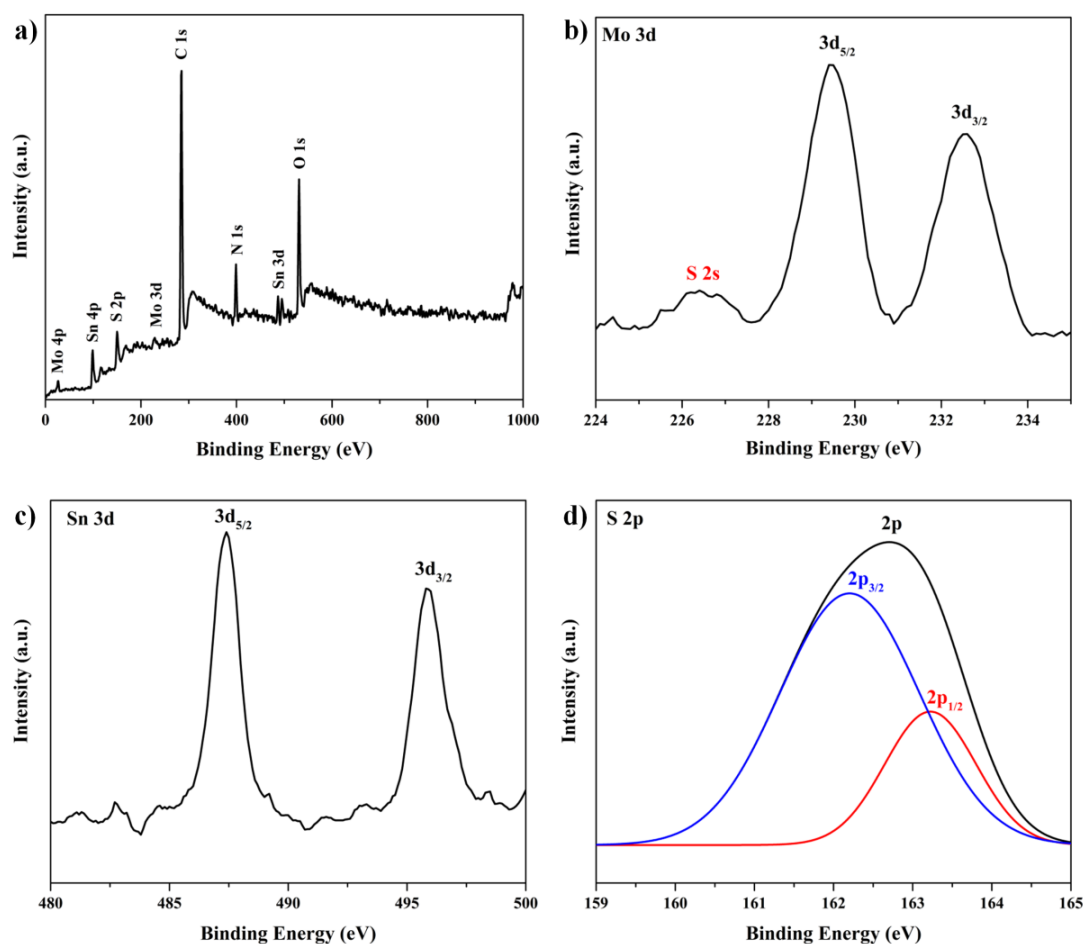
Figure 6.8 a) XPS spectrum of MoS_2-SnO_2 nanocomposite and high resolution XPS spectrum of b) Mo 3d, c) Sn 3d, d) S 2p

From the XPS survey spectrum of MoS_2-SnO_2 nanocomposite (Fig. 6.8a), the presence of peaks corresponding to Mo, Sn, S, O, N and C elements were observed. The high-resolution XPS spectrum of Mo 3d region (Fig. 6.8b) exhibited two peaks at the binding energies 229.4 and 232.4 eV which are belonged to $3d_{5/2}$ and $3d_{3/2}$, respectively. These binding energies were corresponding to the +4 oxidation state of Mo. Also, a broad

peak corresponding to S 2s was observed at 226.5 eV in the same spectrum. The high-resolution XPS spectrum of Sn 3d region is shown in Fig. 6.8c. Two peaks at 487.4 and 495.8 eV were observed. These were belonged to $3d_{5/2}$ and $3d_{3/2}$ of Sn (+4 oxidation state), respectively. The XPS spectrum of S is shown in Fig. 6.8d. The XPS spectrum of S 2p region was resolved into a doublet peak, with the binding energies 162.2 and 163.2 eV corresponding to $2p_{3/2}$ and $2p_{1/2}$ of S, respectively. This peak deconvolution was done considering the spin-orbit coupling rule. The above results confirm the presence of MoS_2 and SnO_2 without any other oxidation products (Chen et al. 2014).

6.2 Electrochemical Characterization of MoS_2-SnO_2 Nanocomposite for the Supercapacitor Application

The specific surface area of MoS_2 nanosheets is large (17.5 m^2 g^{-1}). The conductivity of MoS_2 nanosheet is better than the metal oxides. The flexibility of the MoS_2 nanosheet is also excellent that can act as the supportive structure for the metal nanoparticles. However, the MoS_2 nanosheets tend to get restacked on each other during the electrochemical cycle. This results in the increased thickness and reduced surface area. So, the scope of using MoS_2 nanosheet as a supercapacitor material is limited as mentioned in the comment. But it acts a good additive material when mixed with metal oxide nanoparticles to prepare supercapacitor electrode. The MoS_2 nanosheets would act as the conductive and support structure between the metal oxide nanoparticles at the same time the restacking of MoS_2 nanosheets would be prevented by the metal oxide nanoparticles present in between each nanosheets.

The use of SnO_2 for the electrochemical energy storage application can be considered due to the reasons such as higher theoretical specific capacity (781 mAh g^{-1}), low synthesis cost, versatile nanostructure and morphology, low toxicity and non-carcinogenic. But the electrochemical instability caused by the volume expansion of SnO_2 nanoparticles limits the SnO_2 for the supercapacitor application. Use of SnO_2 nanoparticles functionalized MoS_2 nanosheets would mitigate the discontinuity issue caused by the volume expansion of SnO_2. So, in MoS_2-SnO_2 nanocomposite, the problems associated with each material are mitigated by other material to produce better electrochemical performance than the individual materials.
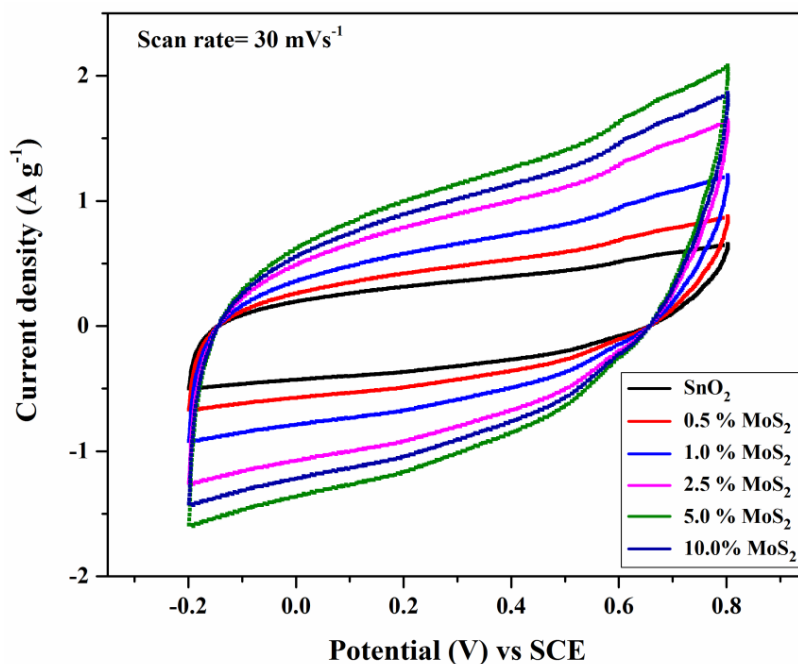
Figure 6.9 Cyclic voltammetry curves of bare SnO_2 nanoparticles and MoS_2-SnO_2 nanocomposite at scanning speed of 30 mVs^{-1} (material loading=1.1 mg cm^{-2})

The cyclic voltammetry (CV) was performed for SnO_2 and MoS_2-SnO_2 between the potential value range of -0.2 V to 0.8 V. The CV plots are shown in Fig. 6.9. CV curves for all samples showed the double layer supercapacitor behavior with a semi-rectangular shape curve. This result is in accordance with the previously reported results (Bonu et al. 2016) (Krishnamoorthy et al. 2016). From Fig. 6.9, it is observed that the output current density of the MoS_2-SnO_2 nanocomposite is higher than the output current density of the bare SnO_2 nanoparticles. During the electrochemical cycles, the SnO_2 nanoparticles undergo volume expansion that leads to increase in the particle size. The increase in particle size leads to microcracks between the SnO_2 particles (Lou et al. 2006) (Brousse et al. 1998). The formation of microcracks and the reduction in surface area were the reasons for the low performance of the SnO_2 nanoparticles. The addition of the MoS_2 nanosheets bridged the SnO_2 nanoparticles and offered a large surface area for the charge transportation between electrode and electrolyte. So, a gradual increase in the output current was observed with respect to increase in the MoS_2 to SnO_2 ratio. The 5% MoS_2-SnO_2 nanocomposite exhibited the highest current density amongst all the electrode materials. But the current density started to decrease when the

MoS$_2$ ratio was increased to 10%. So, it is concluded that the 5%, with highest electrochemical activity, is the optimum MoS$_2$-SnO$_2$ ratio for the supercapacitor application.
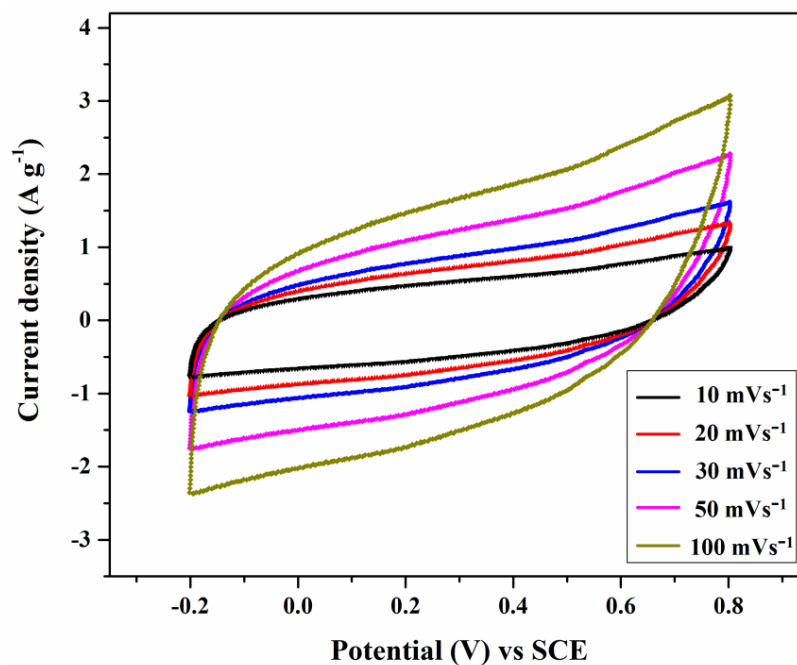
Figure 6.10 Cyclic voltammetry curves of 5% MoS$_2$-SnO$_2$ at different scanning speeds, between an applied potential range of -0.2 V to 0.8 V (material loading=1.1 mg cm^{-2})

Figure 6.10 shows the CV curves of 5% MoS$_2$-SnO$_2$ nanocomposite at the scanning speeds of 10, 20, 30, 50 and 100 mVs^{-1}, respectively. The obtained CV curves for all the scanning speeds are showing a semi-rectangular curve corresponding to double-layer capacitance.

The energy storage by the electric double layer capacitance is illustrated as Fig. 6.11.
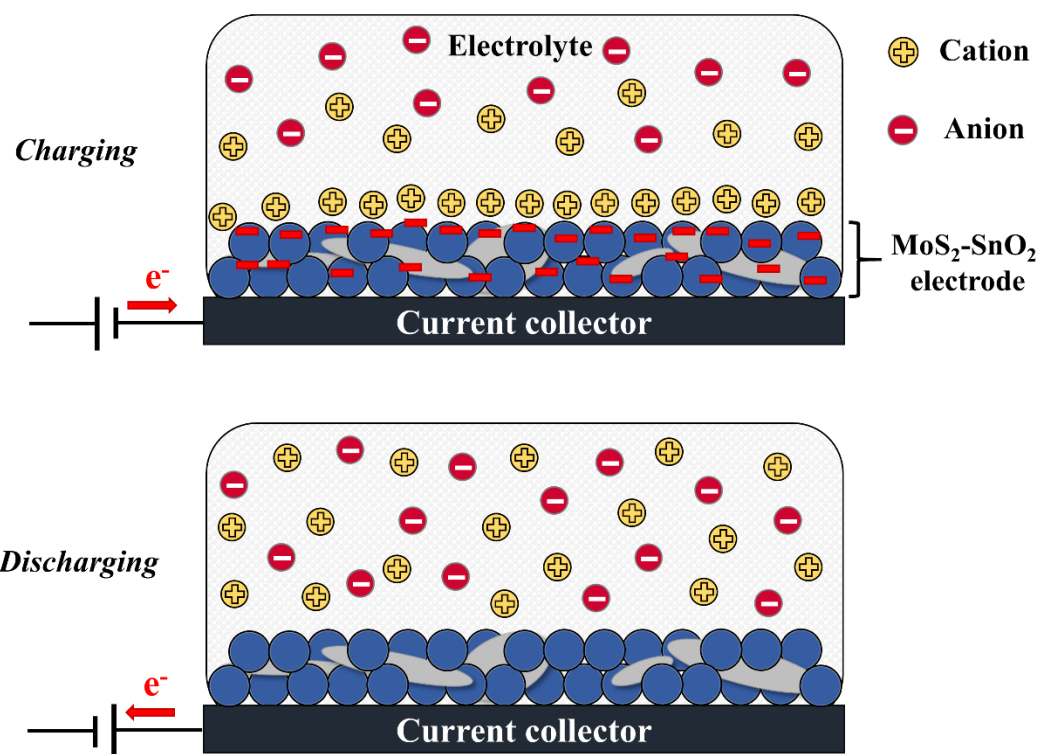
Figure 6.11 Charging and discharging of an electric double layer supercapacitor

During charging, the electrode is negatively polarized by the applied voltage. The cations from the electrolyte are attracted to the negatively charged electrode to neutralize the charge. The formation of oppositely charged layers at the electrode surface is called the electric double layer. This way, the energy is physically stored or accumulated on the surface of the electrode. During discharging, the electrons flow to the external circuit from the electrode surface (Pal et al. 2019).
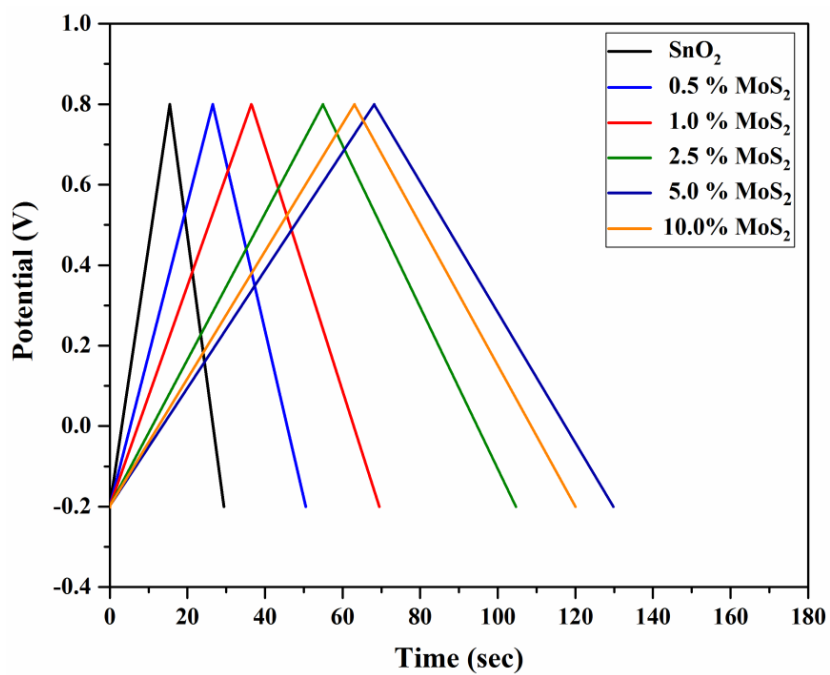
Figure 6.12 Galvanostatic charge-discharge curves of the SnO_2 and the MoS_2-SnO_2 at the constant current density of 1 A g^{-1}
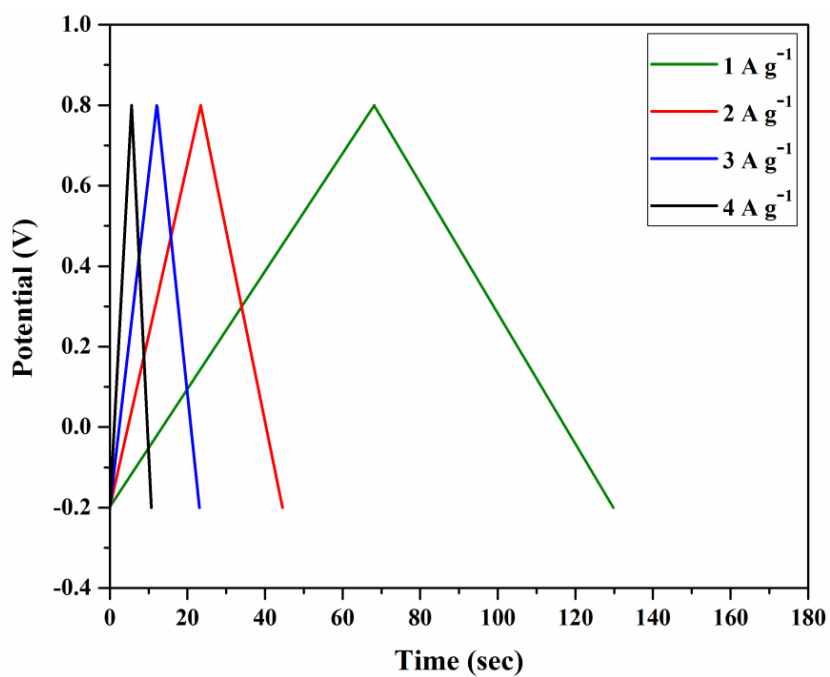
Figure 6.13 Galvanostatic charge-discharge curves of 5% MoS_2-SnO_2 at different current densities

Figure 6.12 shows the galvanostatic charge-discharge curves for the SnO_2 and the MoS_2-SnO_2 nanocomposite. The charge-discharge study was performed in the potential range of -0.2 V to 0.8 V at an applied current density of 1 A g^{-1}. The obtained charge-discharge curves are linear and triangular in shape. This indicates the capacitance nature of the prepared electrode materials. The discharge time of the SnO_2 nanoparticles was 14 seconds, whereas the MoS_2-SnO_2 nanocomposite showed a longer discharge time. The discharge time was increased from 24 seconds for 0.5% MoS_2-SnO_2 to 61 seconds for 5% MoS_2-SnO_2.

Figure 6.13 shows the galvanostatic charge-discharge curve of 5% MoS_2-SnO_2 nanocomposite at different current densities. The decrease in the charging and discharging time was observed when the current density was increased (Huang et al. 2014b). As the current is inversely proportional to the time (I=Q/t), the increase in current density resulted in decreased discharge time (t_d). The discharge time of 61, 21, 11, 5 seconds were measured for the applied current densities of 1, 2, 3 and 4 A g^{-1}, respectively.
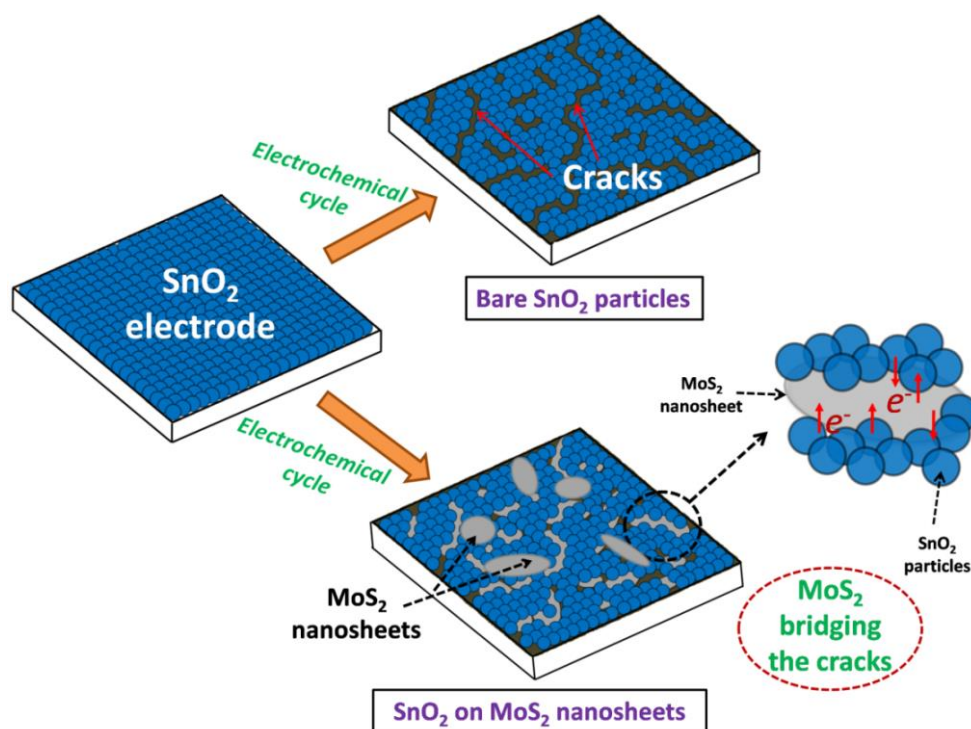
Figure 6.14 Schematic representation of the microcracks in the SnO_2 electrode and MoS_2 nanosheets bridging the microcracks

As mentioned earlier, the SnO_2 particles would go through volume or size change during the charge-discharge processes (Lou et al. 2006) (Brousse et al. 1998). This would lead to microcracks in the SnO_2 electrode. The discontinuities formed by these cracks would affect the charge transportation. But, when the MoS_2 nanosheets were introduced with the SnO_2 nanoparticles, the nanosheets acted as a conductive pathway between the SnO_2 nanoparticles. The MoS_2 nanosheets would anchor the SnO_2 nanoparticles within its surface and bridge the neighboring SnO_2 nanoparticles facilitating the easy charge transfer during the charge-discharge process (Huang et al. 2013). The large surface area of MoS_2 nanosheets leads to effective interaction between the electrode and the electrolyte. Thus, the electrochemical performance (CV curve area and discharge time) was increased for the MoS_2-SnO_2 nanocomposite. However, it was noticed that increasing the MoS_2 ratio beyond 5% led to a decrease in the discharge time. When the ratio of the MoS_2 was increased above the optimum value, the discharge time started to decrease because of the reduction in active SnO_2 material. So it is concluded that 5% is the optimum ratio of MoS_2 nanosheets in the MoS_2-SnO_2 nanocomposite. This is also in accordance with the cyclic voltammetry study.
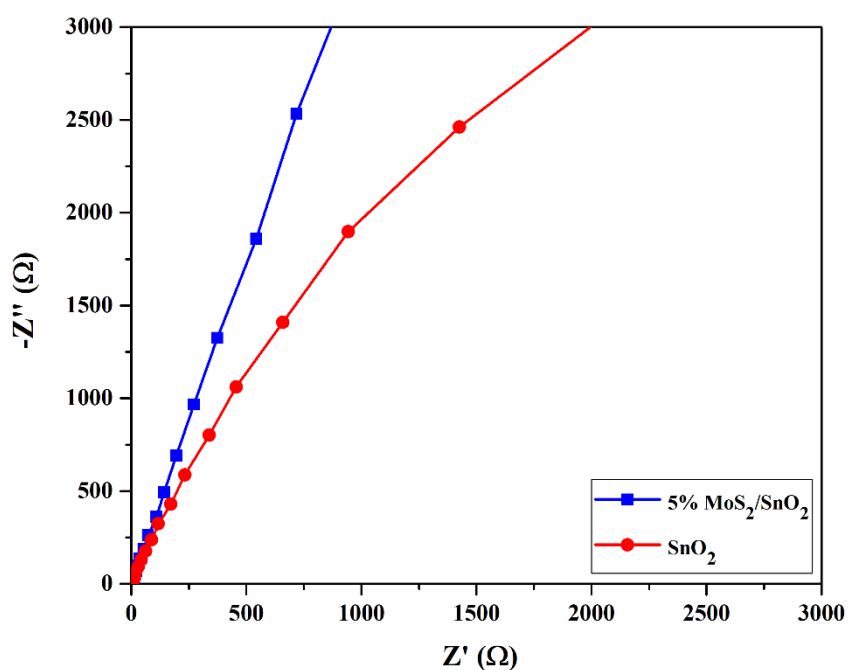
Figure 6.15 Nyquist curve of SnO_2 and 5% MoS_2-SnO_2 nanocomposite
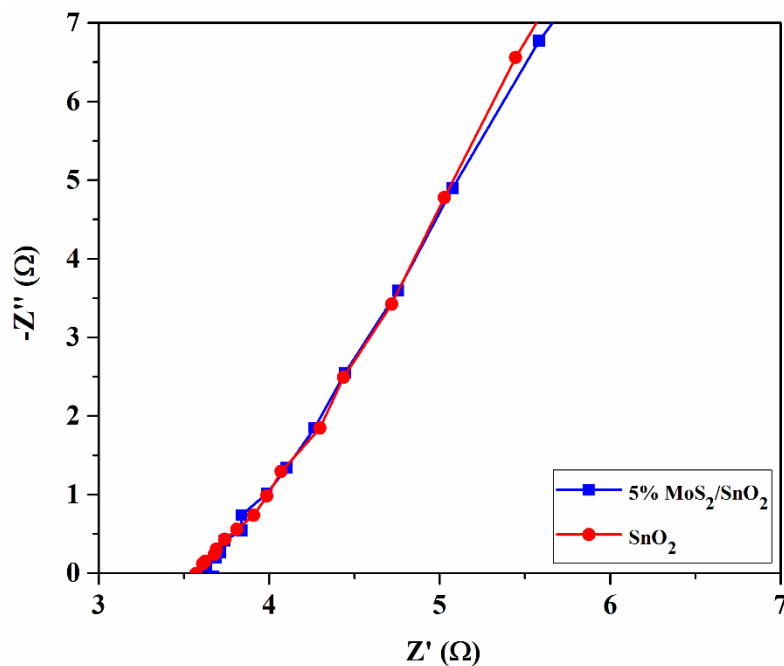
Figure 6.16 Nyquist curve of SnO_2 and 5% MoS_2-SnO_2 nanocomposite: magnified at high frequency region

The Nyquist plot obtained from the electrochemical impedance spectroscopy (EIS) is shown in Fig. 6.15. EIS was performed over the frequency range of 0.1 Hz to 100 kHz for bare SnO_2 and 5% MoS_2-SnO_2 and the plots are compared. A straight line was observed for both materials at the lower frequency region. However, the slope of the 5% MoS_2-SnO_2 nanocomposite was higher than that of the bare SnO_2 nanoparticles. This proves that the diffusion resistance of the MoS_2-SnO_2 nanocomposite was lower than that of the bare SnO_2 nanoparticles. It indicated that the MoS_2-SnO_2 nanocomposite exhibited more ideal capacitor behavior than the bare SnO_2 nanoparticles. The high-frequency region was enlarged and shown in Fig. 6.16. The curves tend to show a very small semi-circle or loop in the high-frequency range indicates the minimum charge-transfer resistance in the material. It is attributed to the low charge transfer resistance of the electrode (Sreejesh et al. 2015). The solution resistance is the value at which the curve is intersecting with the real axis. The values were almost equal for 5% MoS_2-SnO_2 nanocomposite and SnO_2 nanoparticles with 3.67 and 3.6 Ω, respectively.

114

The specific capacitance was calculated from the charge-discharge curves by the following equation (Huang et al. 2013),

$$C_s = (I \cdot t_d) / (m \cdot \Delta V) \qquad (1)$$

Where "C_s" is the specific capacitance (F g^{-1}), "I" is the discharge current (A), "t_d" is the discharge time (s), "m" is the mass of the electrode material (g) and "ΔV" is the potential window. The values of C_s for SnO_2 and MoS_2-SnO_2 were plotted and shown in Fig. 6.17.
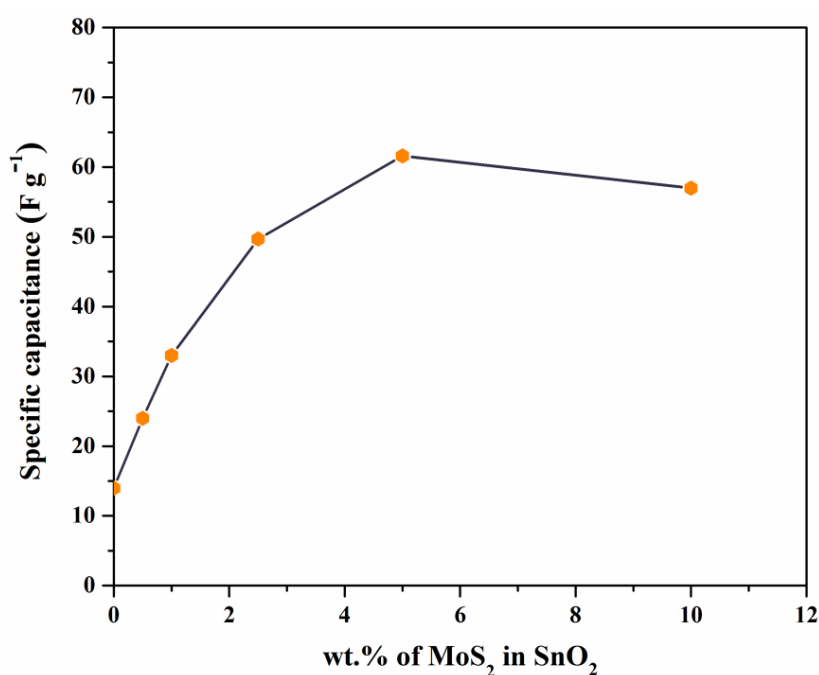
Figure 6.17 Specific capacitance of the MoS_2-SnO_2 nanocomposites with different ratio of MoS_2 in the composite

The specific capacitance (C_s) of bare SnO_2 nanoparticles was calculated as 14 F g^{-1}. The specific capacitance value of the SnO_2 is increased after the addition of the MoS_2 nanosheets. The high surface area and easy charge transportation between the electrode material and electrolyte were the reason for the increased value of the specific capacitance. The 5% MoS_2-SnO_2 nanocomposite showed the highest specific capacitance value of 61.6 F g^{-1} which is 4.4 times greater than that of the bare SnO_2 nanoparticles.
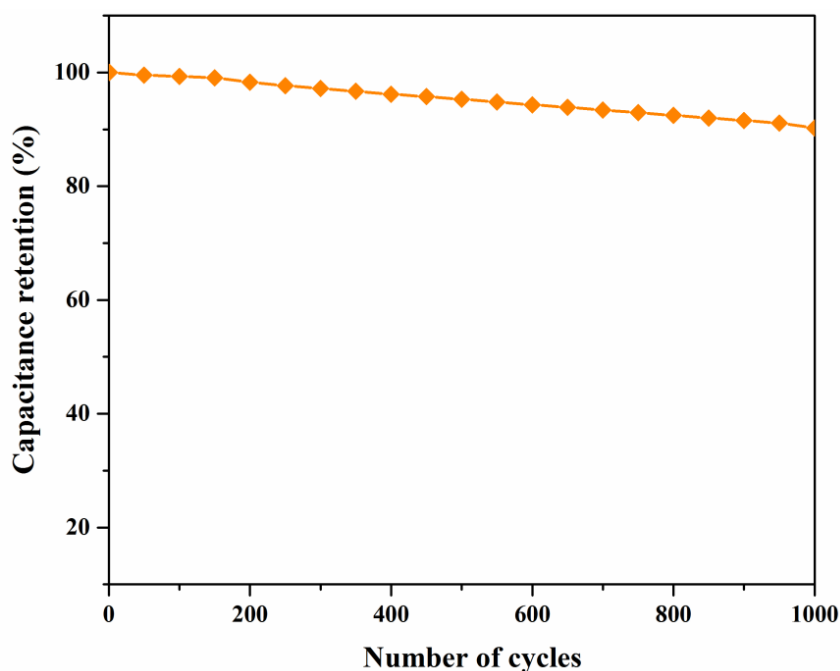
Figure 6.18 Capacitance retention versus the number of charge-discharge cycles for the 5% MoS_2-SnO_2 nanocomposite

The capacitance retention curve of 5% MoS_2-SnO_2 over the charge-discharge of 1000 cycles is shown in Fig. 6.18. The MoS_2-SnO_2 showed excellent cyclic stability by retaining 90% of its original capacitance even after 1000 charge-discharge cycles. This indicates that the electrochemical performance of the SnO_2 nanoparticles is improved by the addition of the MoS_2 nanosheets with the SnO_2. The reasons for the improvement in the performance are, (i) The MoS_2 nanosheets provided good support and conductive path in the electrode material when the microcracks are formed due to volume expansion of SnO_2; (ii) The high surface area offered to the electrode in the form of nanosheets made it easier for the ion transportation between electrolyte and electrode.

6.3 Summary

The SnO_2 nanoparticles were synthesised by the solvothermal method. The synthesised SnO_2 nanoparticles have a spherical-like morphology with the size range of 10 nm to 32 nm. The nanocomposite of exfoliated MoS_2 nanosheets and SnO_2 nanoparticles was prepared to improve the electrochemical performance of the SnO_2 towards the energy

116

storage application. The MoS_2-SnO_2 nanocomposite was prepared by functionalizing SnO_2 nanoparticles onto the surface of MoS_2 nanosheets by the ligand exchange process. The MoS_2 nanosheets mitigated the problem of volume expansion of SnO_2. The MoS_2 nanosheets acted as the conducting bridge between the SnO_2 nanoparticles for charge transportation during the charge-discharge process. Also, the nanosheets provided helped to improve the interaction between the electrolyte and electrode material. The benefits achieved by the compositing SnO_2 nanoparticles with MoS_2 nanosheets enhanced the specific capacitance value from 14 F g^{-1} to 61.6 F g^{-1}. By improving the electrochemical performance of SnO_2, the prepared MoS_2-SnO_2 nanocomposite paves a way to develop low-cost energy storage devices in the future.

Publications from chapter 6

1. Prabukumar, C., Sadiq, M. M. J., Bhat, D. K., and Bhat, K. U. (2019). "SnO_2 nanoparticles functionalized MoS_2 nanosheets as the electrode material for supercapacitor applications." *Materials Research Express*, 6(8), 085526.

CHAPTER 7

ENHANCING THE ELECTROCHEMICAL PERFORMANCE OF THE ZnO ANODE FOR ALKALINE BATTERY APPLICATION

This chapter discusses the synthesis and characterization of ZnO nanorods and ZnO microrods. The effect of size and shape of the ZnO on its electrochemical characteristics is studied in detail. The changes in electrochemical performance of ZnO in KOH electrolyte, owing to the MoS_2-SnO_2 nanocomposite additive, are examined by various analysis.

7.1 Synthesis of ZnO Nanorods and Microrods
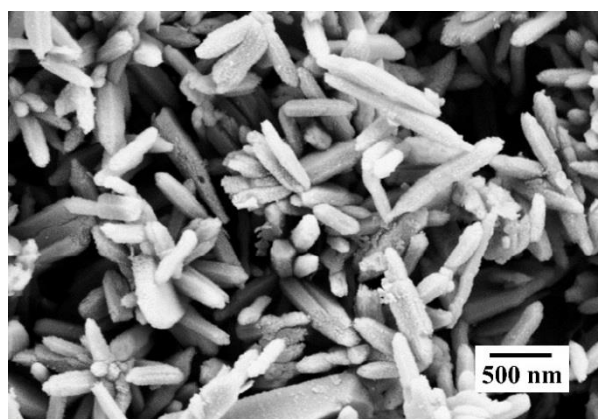
Figure 7.1 FESEM micrograph of the microwave synthesised ZnO nanorods
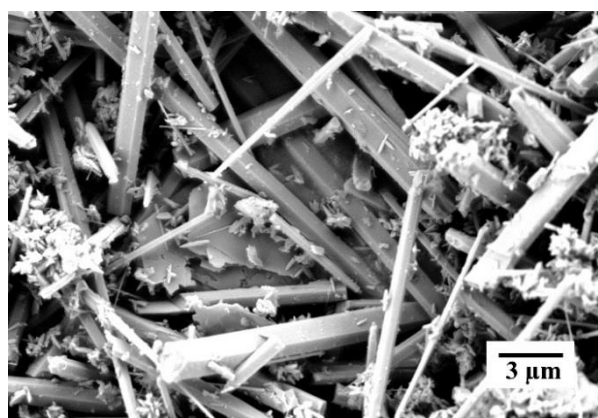
Figure 7.2 FESEM micrograph of the synthesised ZnO microrods
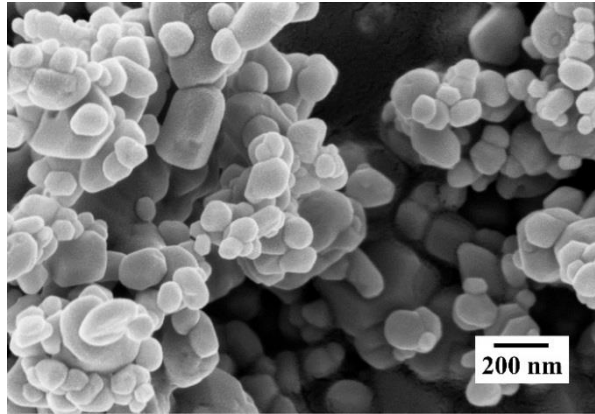
Figure 7.3 FESEM micrograph of commercial ZnO nanoparticles

Figure 7.1 shows the FESEM micrograph of the ZnO nanorods (NRs) synthesised using microwave heating method. It is observed that the synthesised product shows one-directional growth of nanorods. The length of the nanorods is in the range of 300 nm to 500 nm. The diameter of the nanorods is measured to be less than 100 nm. Figure 7.2 shows the FESEM micrograph of the hydrothermally synthesised ZnO microrods (MRs). The micrograph shows that the synthesised microrods have a hexagonal cross-section. The average length of the ZnO microrods is 10 µm and while the average diameter is 1 µm. Figure 7.3 shows the FESEM micrograph of the commercial ZnO nanoparticles (NPs). It is observed that the commercial ZnO NPs contained particles with different morphologies, such as plate-like, sphere-like and cylinder-like with a size range of 70 nm to 300 nm
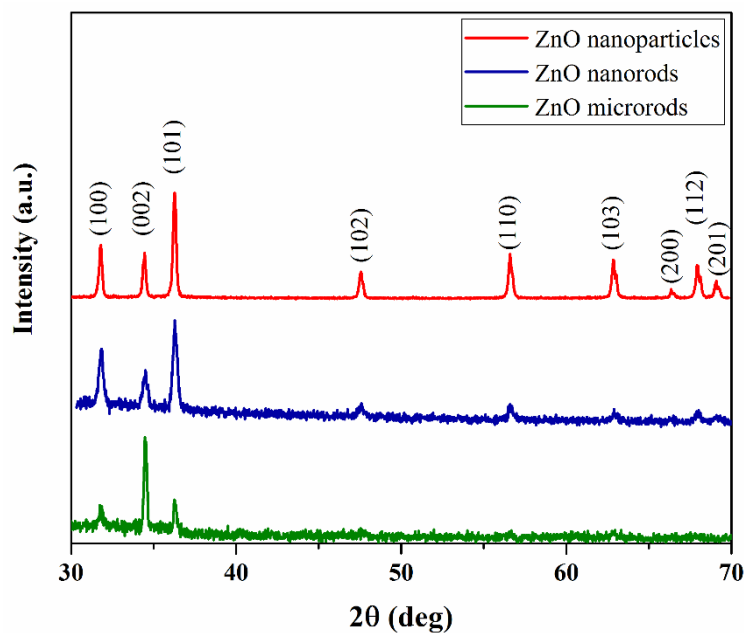
Figure 7.4 XRD patterns of commercial ZnO nanoparticles, microwave synthesised ZnO nanorods and hydrothermal synthesised ZnO microrods

Figure 7.4 shows the XRD patterns of the commercial ZnO nanoparticles, the microwave heated ZnO nanorods and the hydrothermally synthesised ZnO microrods. All the samples exhibit the peaks belonging to the ZnO wurtzite phase (ICDD 03-065-0523). The XRD patterns show that the ZnO nanoparticles and ZnO nanorods have preferred (101) orientation. But the relative intensity of the peak belonging to (101) plane is high for nanorods compared to that of the nanoparticles. On the other hand, the ZnO microrods show the preferred orientation of (002) plane. The preferred (002) orientation of ZnO microrods is attributed to its hexagonal cross-section.
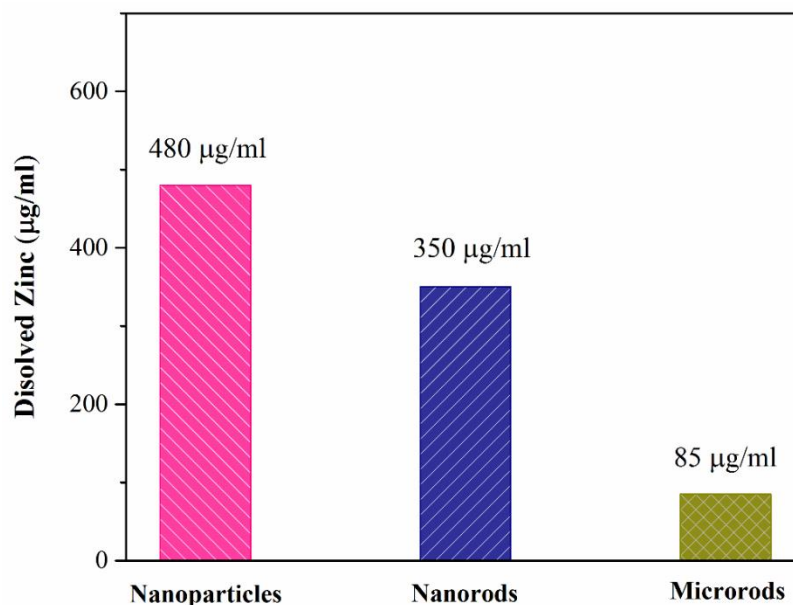
Figure 7.5 Solubility of the ZnO samples in 6 M KOH solution

The stability of ZnO samples in high concentration alkaline electrolyte was studied by determining the quantity of zinc dissolved in 6 M KOH solution. In Zn alkaline battery, the high solubility of ZnO in the electrolyte leads to uneven deposition of the zinc during the charging process. That eventually leads to the growth of undesired dendrite structures on the ZnO anode (Mainar et al. 2018a). The atomic absorption spectroscopy (AAS) result (Fig. 7.5) revealed that the dissolved zinc from ZnO nanoparticles, nanorods and microrods is 480 µg/ml, 350 µg/ml and 85 µg/ml, respectively. The one-dimensional ZnO rods (Microrods and nanorods) are more stable in the KOH electrolyte than the commercial ZnO nanoparticles with plate-like and sphere-like morphology. It should be noted that the ZnO microrods showed excellent stability compared to other ZnO samples. It is attributed to the less surface area of the microrods due to their longer length and large diameter. Since the surface area is low, the material had less interaction with the KOH electrolyte, resulting in low solubility. However, the reason behind the low solubility of nanorods compared to the nanoparticles is due to its rod morphology having fewer edges and corners that are the hotspots for the dissolution (Ullah et al. 2013).

7.2 Electrochemical Reactions of the ZnO Anode in Alkaline Electrolyte

In alkaline batteries, the charging and discharging processes are ascribed to oxidation and reduction reactions of the ZnO with the alkaline electrolyte (Mainar et al. 2018a). During charging, the ZnO is converted into the zincate ions, $Zn(OH)_4^{2-}$ (Eqn. 6). Then the zincate ions are reduced to metallic Zn (Eqn. 7). This is also called as Zn plating. During discharging, the Zn undergoes oxidation to form zincate ions (Eqn. 8). When the electrolyte solution close to the surface is saturated with the zincate ions, the zincate ions precipitate into ZnO. This is called as passivation process (Eqn. 9).

Charging/reduction reaction:

$$ZnO + H_2O + 2OH^- \rightarrow Zn(OH)_4^{2-} \tag{6}$$

$$Zn(OH)_4^{2-} + 2e^- \rightarrow Zn + 4OH^- \tag{7}$$
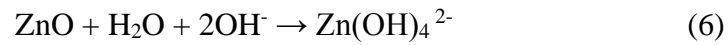
Discharging/oxidation reaction:

$$Zn + 4OH^- \rightarrow Zn(OH)_4^{2-} + 2e^- \tag{8}$$

$$Zn(OH)_4^{2-} \rightarrow ZnO + H_2O + 2OH^- \tag{9}$$
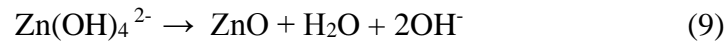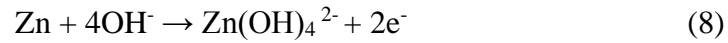
During charging, an undesired reaction occurs between the Zn and the water that lead to the evolution of hydrogen gas (Eqn. 10) (Mainar et al. 2018a) (Li and Dai 2014). The hydrogen evolution reaction (HER) from the Zn causes the corrosion of the Zn, water depletion in the electrolyte and increased internal pressure inside the battery (Mainar et al. 2018a).

$$Zn + 2H_2O \rightarrow Zn(OH)_2 + H_2 \uparrow \tag{10}$$
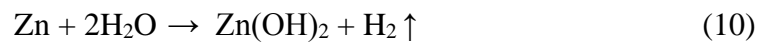
This could be avoided by minimizing the solubility of zincate ions into the alkaline electrolyte and suppressing the hydrogen evolution reaction (HER). The recyclability and reversibility of the anode are improved by reducing the passivation of ZnO.

7.3 Effect of Size and Shape of the ZnO on its Electrochemical Properties

The effect of size and type of the morphology of ZnO on its electrochemical properties such as HER, corrosion behaviour, electrochemical kinetics, such as charge-transfer resistance and oxidation-reduction reactions are studied.
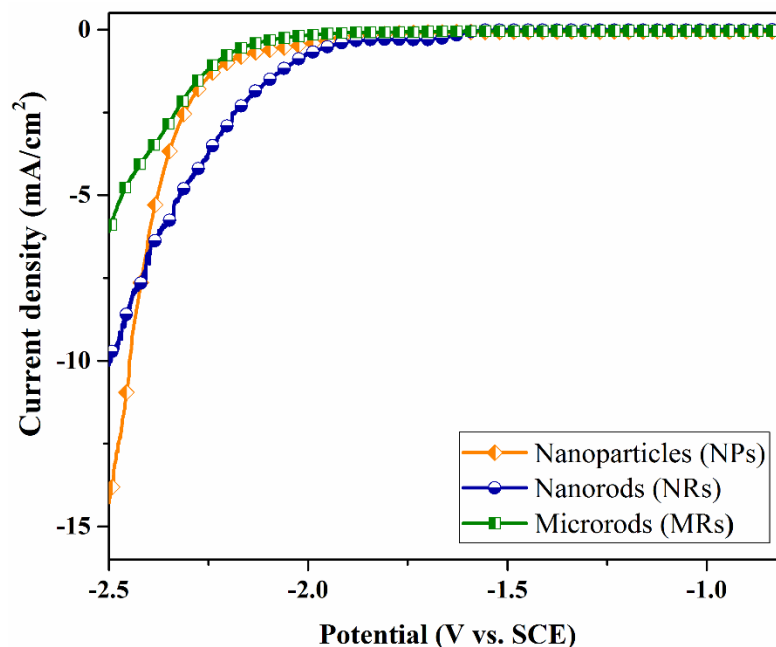
Figure 7.6 Cathodic polarization curves for commercial ZnO nanoparticles, microwave synthesised ZnO nanorods and hydrothermal synthesised ZnO microrods

The hydrogen evolution reaction (HER) or generation of hydrogen gas at the ZnO electrode is one of the major factors that deteriorate the performance of the zinc alkaline batteries (Dundálek et al. 2017) (Zhang et al. 2020c). The cathodic polarization study was performed to understand the influence of the size and shape of the active ZnO material on the hydrogen evolution. Figure 7.6 shows the cathodic polarization curves of ZnO nanoparticles, ZnO nanorods and ZnO microrods in the KOH electrolyte. The low current density from the ZnO microrods indicates its low HER activity. The HER activity of ZnO nanorods was higher than the ZnO nanoparticles in the beginning. However, the HER activity of the ZnO nanoparticles increased more than that from the nanorods towards the end that is observed by the higher current density from the ZnO nanoparticles.
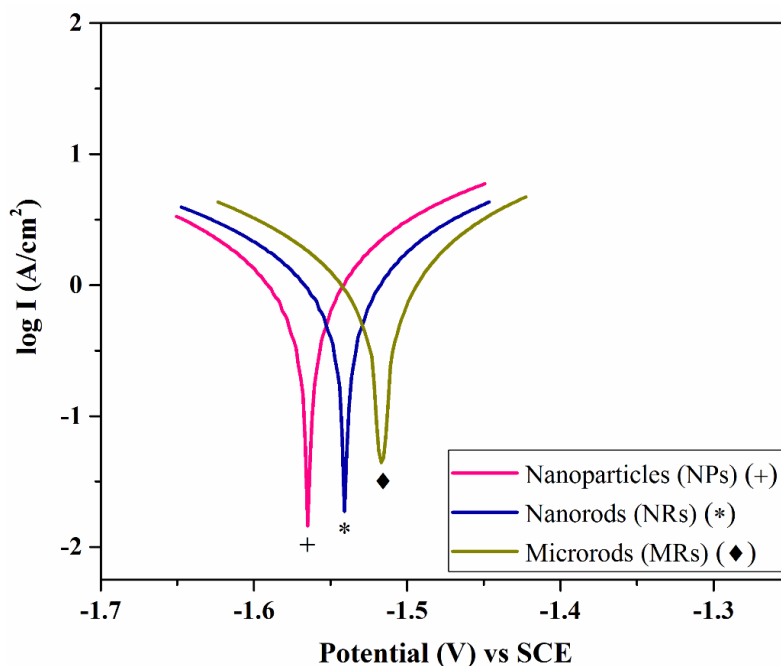
Figure 7.7 Tafel polarization curves for the ZnO nanoparticles, ZnO nanorods and ZnO microrods

Figure 7.7 shows the Tafel polarization curves of the ZnO nanoparticles, ZnO nanorods and ZnO microrods. It is observed that the corrosion potential (E_{corr}) for ZnO nanoparticles, ZnO nanorods and ZnO microrods is -1.565 V, -1.539 V and -1.516 V, respectively. The corrosion current (I_{corr}) was determined as 3.15 mA/cm^2, 2.42 mA/cm^2 and 1.815 mA/cm^2 for nanoparticles, nanorods and microrods, respectively. High 'E_{corr}' and low 'I_{corr}' attribute to the anti-corrosion behaviour of the material. The corrosion of Zn/ZnO is associated with the hydrogen evolution reaction (Li and Dai 2014)(Long et al. 2016). The ZnO microrods with high 'E_{corr}' and low 'I_{corr}' are less prone to corrosion. This is again due to its large diameter that offered less surface area to interact with the KOH electrolyte. The ZnO nanorods show the second-best performance against corrosion, while the ZnO nanoparticles with the sphere-like and plate-like morphologies were very prone to corrosion. It is inferred that the nanorod morphology of the ZnO was more stable than the spherical-like and plate-like morphology against corrosion.
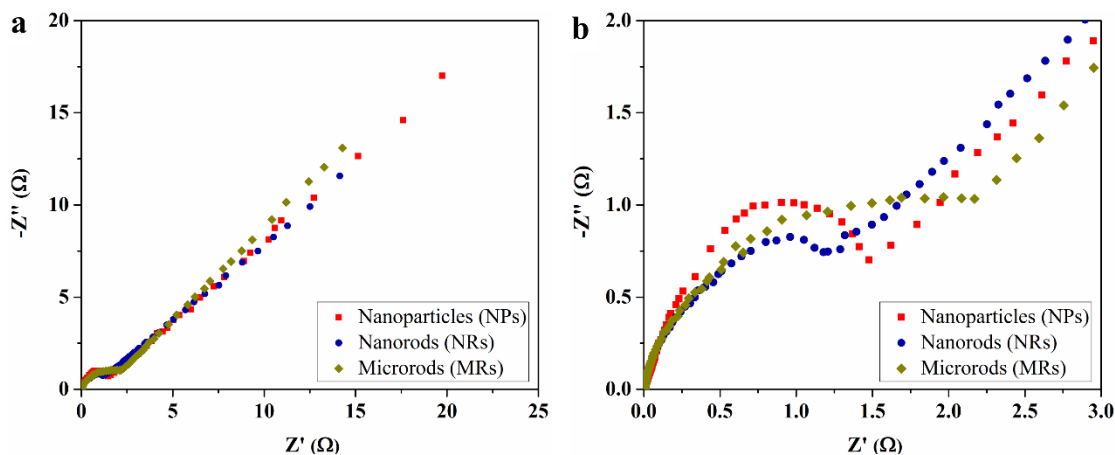
Figure 7.8 a) Nyquist plots for the ZnO nanoparticles, ZnO nanorods and ZnO microrods, b) their corresponding Nyquist plots in high frequency region

Figure 7.8 shows the Nyquist plots obtained from the electrochemical impedance spectroscopy (EIS) for the ZnO nanoparticles, ZnO nanorods and ZnO microrods. The semi-circle in the high-frequency region denotes the charge-transfer resistance (R_{ct}) between the ZnO electrode and the electrolyte. The Nyquist plots for all ZnO samples at the high-frequency region are shown in Fig. 7.8b. The diameter of the semi-circle denotes the charge-transfer resistance. The 'R_{ct}' values for the ZnO nanoparticles, ZnO nanorods and ZnO microrods are determined as 2.42 Ω, 2.2 Ω and 2.44 Ω, respectively. The charge-transfer resistance for the ZnO nanorods is relatively low compared to that of the ZnO nanoparticles and the ZnO microrods. The low 'R_{ct}' is be attributed to reduced polarization in the material due to its uniform morphology and high electrochemical activity due to the high surface area (Chamoun et al. 2015) (Long et al. 2017b). The 'R_{ct}' value for the ZnO microrods was high due to the relatively low surface area that limited the electrochemical activity.

Figure 7.9, 7.10 and 7.11 show the cyclic voltammetry (CV) results of the ZnO nanoparticles, ZnO nanorods and ZnO microrods, respectively. The cyclic voltammetry curves explain the anodic and cathodic behaviour of the ZnO. The anodic and cathodic peaks of cyclic voltammetry are attributed to oxidation and reduction reactions of the corresponding material, respectively.
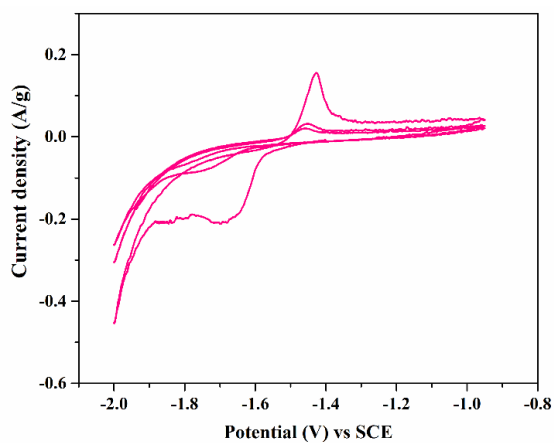
Figure 7.9 Cyclic voltammetry (CV) curves of commercial ZnO nanoparticles (material loading= 2 mg cm^{-2})
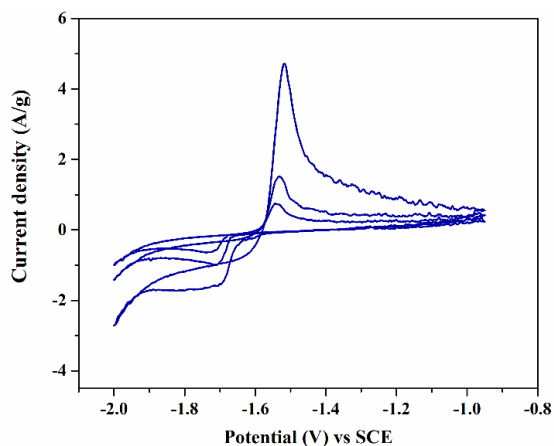
Figure 7.10 Cyclic voltammetry curves of microwave synthesised ZnO nanorods (material loading= 2 mg cm^{-2})
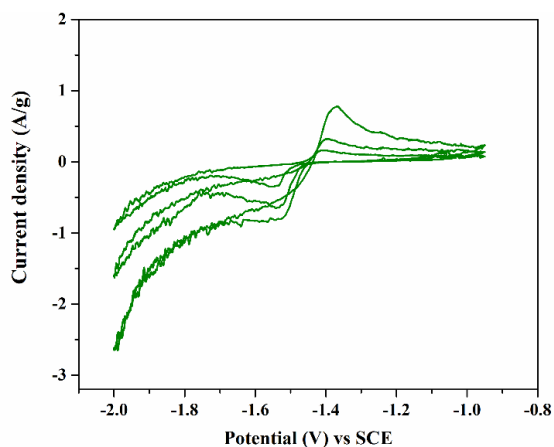
Figure 7.11 Cyclic voltammetry curves of hydrothermal synthesised ZnO microrods (material loading= 2 mg cm^{-2})

126

It is observed that the anodic and the cathodic peaks of the ZnO nanorods exhibit high current density compared to the ZnO nanoparticles and the ZnO microrods. This enhanced current density would result in an enlarged area under the CV curve. The increased area under the CV curve indicates the enhanced capacity of the material (Liu et al. 2019). The current densities at the anodic and cathodic peaks of the ZnO nanoparticles were the lowest. The reason behind the high electrochemical activity of the ZnO nanorod is due to their nanorods morphology and high specific surface area that enhanced the surface interaction between the ZnO and the electrolyte. The potential difference (ΔE_{ac}) between the anodic and the cathodic reactions is 0.274, 0.189 and 0.159 V for the ZnO nanoparticles, ZnO nanorods and ZnO microrods, respectively. The narrow 'ΔE_{ac}' means a small potential difference between the charging and discharging process (Long et al. 2016).

It is observed that the current densities at anodic and cathodic peaks were decreased in the subsequent cycles for all ZnO samples. This decrease in the current density, indicated by the area under the CV curve attributes to the non-recyclability of the material (Peng et al. 2019). When the electrolyte solution near the electrode surface is saturated with the zincate ions, the zincate ions precipitate as a passive layer on the ZnO. The diffusion of OH^- ions to the Zn is limited by this ZnO layer that would lead to the formation of thick ZnO (Mainar et al. 2018a). The reduction in current density of the second and the third cycle with respect to the first cycle was calculated. The I_2/I_1 and I_3/I_1 ratios of anodic and cathodic peaks for all ZnO materials are shown in Table 7.3. The anodic and cathodic current densities of the ZnO nanoparticles were reducing faster than that of the ZnO nanorods and the microrods. The small reduction in current densities for the ZnO microrods was due to its low solubility, which prevented the loss of zincate ions into the electrolyte. The decrease in current density could be minimized by avoiding the zincate dissolution into the electrolyte and improving the ionic transportation between the electrolyte and the ZnO electrode.

The further increase in the current density in the cathodic region after the cathodic peak is attributed to the hydrogen evolution reaction from the ZnO in the KOH solution (Gallaway et al. 2014) (Peng et al. 2019). It is observed that the current density from HER activity was notably higher compared to the current density corresponding to the

127

cathodic peak. Among all ZnO samples, the ZnO nanorods exhibited higher cathodic current density relative to that from HER activity. In contrast, the current density from HER activity was more prominent than that of cathodic reaction for the ZnO nanoparticles and the ZnO microrods.

Among bare ZnO samples (ZnO without any additives), the ZnO nanorods showed excellent output current density due to reduction and oxidation reactions. Also, it showed a good performance against corrosion due to its rod morphology.

7.4 Effect of MoS$_2$-SnO$_2$ additive on the electrochemical properties of the ZnO

TEM micrographs (Fig. 6.6) of MoS$_2$-SnO$_2$ nanocomposite were analysed in the chapter 6. It was established that the SnO$_2$ nanoparticles were functionalized on the surface of MoS$_2$ nanosheets. The MoS$_2$ nanosheets provide their surface to facilitate the charge transfer (Wang et al. 2016a). The SnO$_2$ has tendency to suppress the hydrogen gas evolution due to its high overpotential of hydrogen evolution reaction (HER) (Zheng et al. 2019).
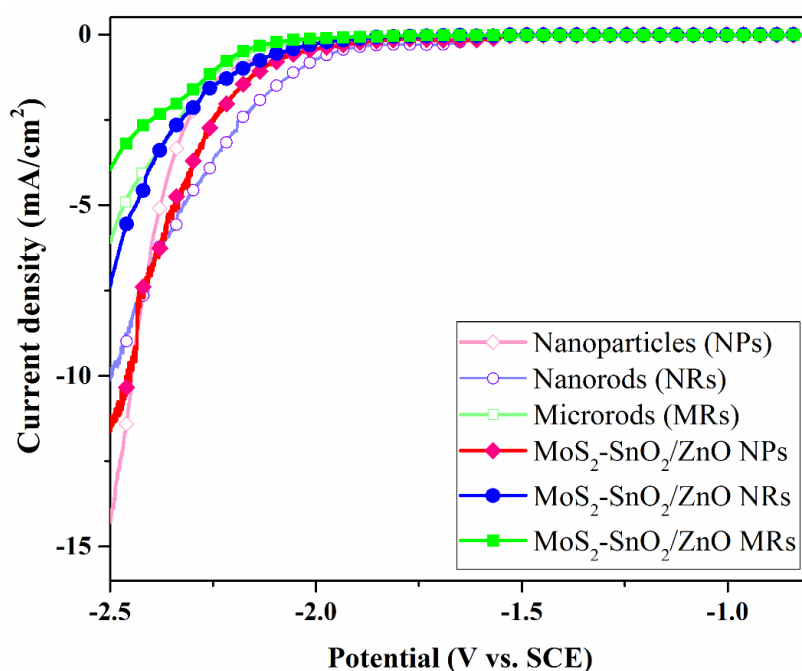
Figure 7.12 Cathodic polarization curves for the ZnO nanoparticles, ZnO nanorods and ZnO microrods, with the MoS$_2$-SnO$_2$ additive

The cathodic polarization curves for bare ZnO and MoS_2-SnO_2/ZnO samples are shown in Fig. 7.12. The MoS_2-SnO_2/ZnO hybrid contained ZnO, MoS_2-SnO_2 and PVA (binder) in the ratio of 75:15:10, respectively. It is observed that the current density for ZnO samples was reduced significantly after the addition of MoS_2-SnO_2 with them. The decrease in the current density indicates the effect of MoS_2-SnO_2 on suppressing the hydrogen evolution reaction. This is due to the high overpotential for hydrogen evolution of Sn and SnO_2 (Feng et al. 2014)(Zheng et al. 2019)(Yuan et al. 2005). Among all the MoS_2-SnO_2/ZnO samples, MoS_2-SnO_2/ZnO nanoparticles showed high HER activity. MoS_2-SnO_2/ZnO nanorods showed moderate HER activity, while MoS_2-SnO_2/ZnO microrods showed low HER activity.
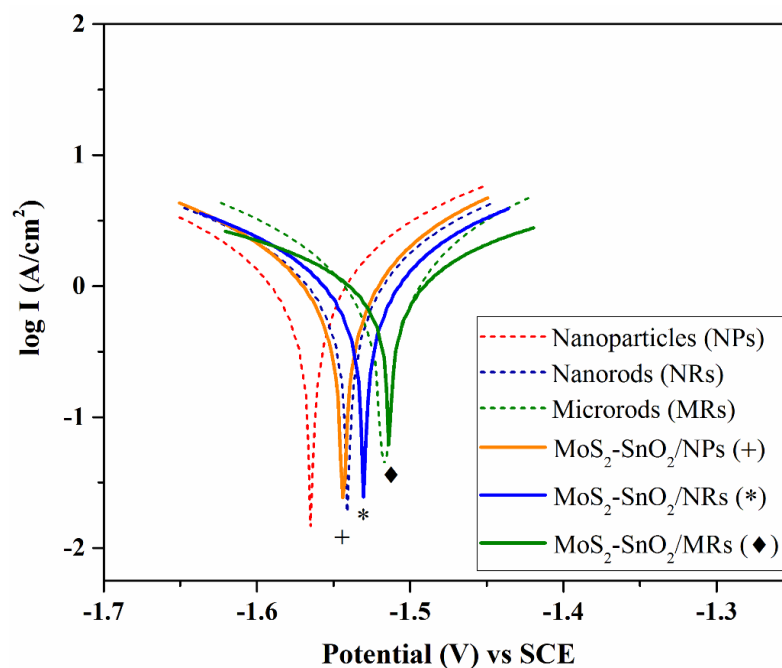
Figure 7.13 Tafel polarization curves for the ZnO nanoparticles, ZnO nanorods and ZnO microrods, with and without MoS_2-SnO_2 additive

The Tafel polarization curves for all MoS_2-SnO_2/ZnO samples are shown in Fig. 7.13. The Tafel plots for the bare ZnO samples are also shown for the comparison purpose. The effect of MoS_2-SnO_2 additive on the inhibition of corrosion of ZnO is understood from the increase in 'E_{corr}' values. The corrosion potential (E_{corr}) and corrosion current density (I_{corr}) values for the bare ZnO and the MoS_2-SnO_2/ZnO samples obtained from Tafel polarization are shown in Table 7.1.

129

Table 7.1 Tafel plot values for bare ZnO (commercial, microwave synthesised, hydrothermal synthesised) and the MoS$_2$-SnO$_2$/ZnO samples

Sample	ZnO NPs	ZnO NRs	ZnO MRs	MoS$_2$-SnO$_2$/ZnO NPs	MoS$_2$-SnO$_2$/ZnO NRs	MoS$_2$-SnO$_2$/ZnO MRs
E$_{corr}$ (V)	-1.565	-1.539	-1.516	-1.544	-1.530	-1.514
I$_{corr}$ (mA/cm²)	3.15	2.42	1.815	2.86	1.87	1.678
Inhibition Efficiency (%)	-	23.2	42.4	9.2	40.6	46.7

The corrosion potential, 'E$_{corr}$' values for the MoS$_2$-SnO$_2$/ZnO samples are shifted towards more positive values with respect to corresponding bare ZnO samples. The shift of 'E$_{corr}$' to more positive indicates that the MoS$_2$-SnO$_2$ additive made ZnO more anti-corrosion in the KOH electrolyte. Similarly, the corrosion current, 'I$_{corr}$', which is attributed to the rate of corrosion was also reduced for the MoS$_2$-SnO$_2$/ZnO samples. The inhibition efficiency was calculated to determine the effect of MoS$_2$-SnO$_2$ on inhibiting the corrosion. The inhibition efficiency for the ZnO samples with and without MoS$_2$-SnO$_2$ additive was calculated by the formula given below (Long et al. 2017b).

$$\text{Inhibition efficiency} = (I^0_{corr} - I_{corr})/(I^0_{corr}) * 100 \qquad (11)$$

Here, 'I$^0_{corr}$' denotes the current density for the commercial ZnO nanoparticles. I$_{corr}$ represents other individual ZnO samples used in the present study. Table 7.1 recites that the inhibition efficiency for ZnO samples was improved after the addition of MoS$_2$-SnO$_2$ to ZnO. The MoS$_2$-SnO$_2$/ZnO microrods and ZnO microrods showed high inhibition efficiency of 46.7% against corrosion. It is mainly because of their large diameter that offered low surface area to interact with the electrolyte. On the other hand, the MoS$_2$-SnO$_2$/ZnO nanorods showed the inhibition efficiency of 40.6%. The inhibition efficiency was improved significantly from 23.2% (bare ZnO nanorods) after

the addition of MoS_2-SnO_2. The MoS_2-SnO_2/ZnO nanoparticles also showed a 9% inhibition efficiency against corrosion. As stated earlier, hydrogen evolution is the major factor for the corrosion of ZnO in the KOH electrolyte (Long et al. 2016). The addition of MoS_2-SnO_2 to ZnO showed effectiveness in suppressing the HER activity by the cathodic polarization study mentioned already. So, the positive shift in 'E_{corr}' and reduction in 'I_{corr}' resulted from incorporating the MoS_2-SnO_2 additive to the ZnO. The MoS_2-SnO_2 passivated the ZnO surface that avoided the direct contact of ZnO with the electrolyte. This prevented the loss of zinc species into the electrolyte. These are the contributing factors for the improvement of the anti-corrosion behaviour of the MoS_2-SnO_2/ZnO composite samples.
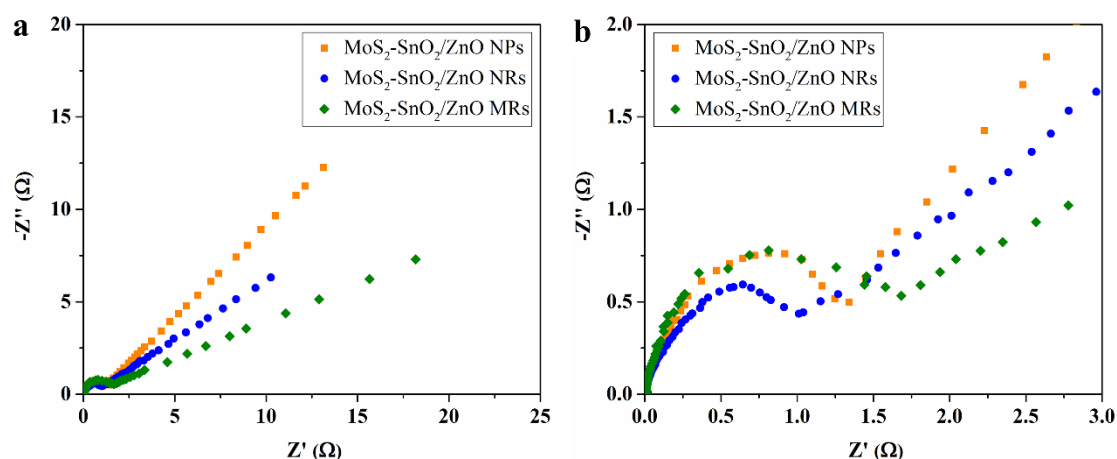
Figure 7.14 Nyquist plots for the ZnO nanoparticles, ZnO nanorods and ZnO microrods, with MoS_2-SnO_2 additive, b) their corresponding Nyquist plots in high-frequency region

Figure 7.14 shows the Nyquist plots of MoS_2-SnO_2/ZnO nanoparticles, MoS_2-SnO_2/ZnO nanorods and MoS_2-SnO_2/ZnO microrods. The charge-transfer resistance (R_{ct}) determined from the semi-circle in the high-frequency region is 1.705 Ω, 1.5 Ω and 1.82 Ω for the MoS_2-SnO_2/ZnO nanoparticles, MoS_2-SnO_2/ZnO nanorods and MoS_2-SnO_2/ZnO microrods, respectively. Though the difference in 'R_{ct}' of bare ZnO is narrow, the addition of MoS_2-SnO_2 to ZnO reduced the charge-transfer resistance significantly in MoS_2-SnO_2/ZnO. The decrease in charge-transfer resistance was the result of increased conductivity by the MoS_2-SnO_2 incorporated with the ZnO. The MoS_2 nanosheets offered a large surface area to facilitate the charge transfer between

KOH electrolyte and ZnO particles/rods as well as the KOH electrolyte and the SnO_2 nanoparticles. Also, the SnO_2 nanoparticles that are in contact with the surface of ZnO enhanced its conductivity. The charge-transfer resistance is an important factor of an electrode material for the battery application. The potential loss is minimized due to the decreased charge-transfer resistance and it would result in better charge-discharge cycles (Chamoun et al. 2015). It is observed that the MoS_2-SnO_2/ZnO nanorods show the smallest 'R_{ct}' value among bare ZnO and MoS_2-SnO_2/ZnO samples.
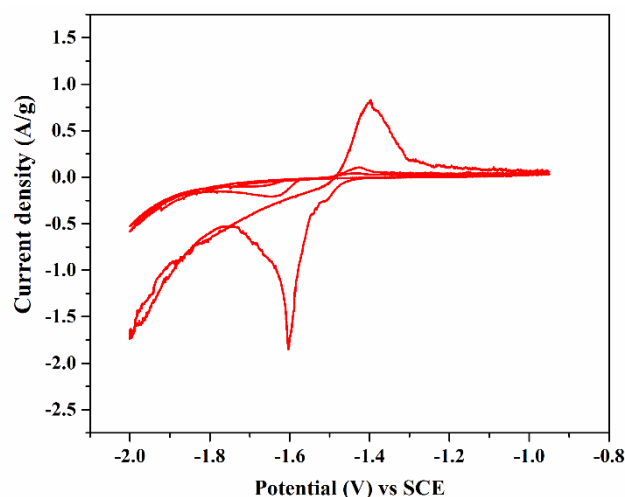
Figure 7.15 Cyclic voltammetry curves of MoS_2-SnO_2/ZnO nanoparticles (material loading= 2 mg cm^{-2})
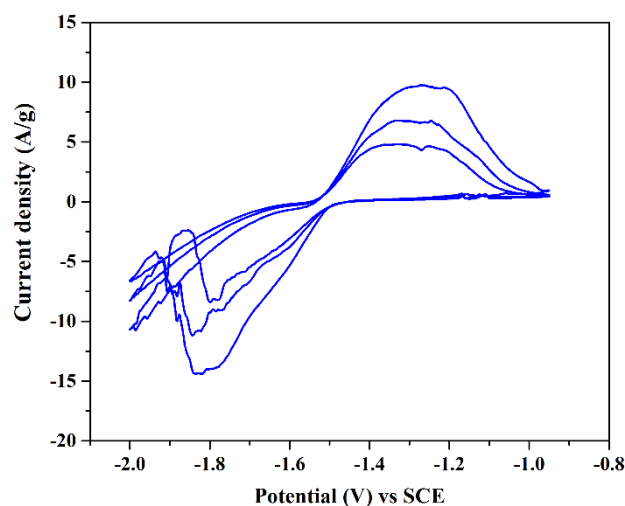
Figure 7.16 Cyclic voltammetry curves of MoS_2-SnO_2/ZnO nanorods (material loading= 2 mg cm^{-2})
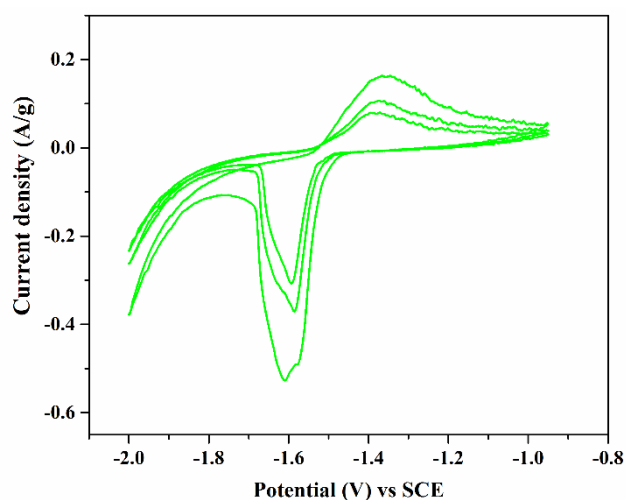
Figure 7.17 Cyclic voltammetry curves of MoS$_2$-SnO$_2$/ZnO microrods (material loading= 2 mg cm^{-2})

Figure 7.15 shows the CV result of the MoS$_2$-SnO$_2$/ZnO nanoparticles. The anodic and cathodic peak potentials are observed at -1.396 V and -1.602 V, respectively. The potential difference (ΔE_{ac}) between anodic and cathodic reactions is 0.206 V. The area under the CV curve of the MoS$_2$-SnO$_2$/ZnO nanoparticles is large compared to that of the bare ZnO nanoparticles. From the CV curve of MoS$_2$-SnO$_2$/ZnO nanorods (Fig. 7.16), the anodic and cathodic potentials are measured as -1.269 V and -1.84 V, respectively. The potential difference, 'ΔE_{ac}' for MoS$_2$-SnO$_2$/ZnO nanorods is 0.571 V. Similar to the MoS$_2$-SnO$_2$/ZnO nanoparticles, the area under the CV curve for ZnO nanorods is increased after the addition of MoS$_2$-SnO$_2$ (Fig. 7.16). Figure 7.17 shows the CV result of MoS$_2$-SnO$_2$/ZnO microrods. The potentials for the anodic and cathodic reaction are observed at -1.366 V and -1.609 V, respectively. The potential difference, 'ΔE_{ac}' is 0.243 V. In contrast to other ZnO samples, the addition of MoS$_2$-SnO$_2$ did not improve the anodic and cathodic current densities of ZnO microrods. The potential and current density values of the anodic and cathodic processes for the bare ZnO and MoS$_2$-SnO$_2$/ZnO samples are listed in Table 7.2.

133

Table 7.2 Potential and current density values of the anodic and cathodic processes for bare ZnO and MoS$_2$-SnO$_2$/ZnO samples

Samples	Anodic		Cathodic	
	Potential (V)	Current density (A/g)	Potential (V)	Current density (A/g)
ZnO NPs	-1.426	0.156	-1.700	-0.211
ZnO NRs	-1.517	4.712	-1.706	-1.595
ZnO MRs	-1.368	0.777	-1.527	-0.805
MoS$_2$-SnO$_2$/ZnO NPs	-1.396	0.828	-1.602	-1.852
MoS$_2$-SnO$_2$/ZnO NRs	-1.269	9.755	-1.84	-14.35
MoS$_2$-SnO$_2$/ZnO MRs	-1.366	0.163	-1.609	-0.527

The Nyquist plots (Fig. 7.14) showed that the addition of MoS$_2$-SnO$_2$ nanocomposite reduces the charge-transfer resistance between the ZnO and the electrolyte by forming a conductive network on the ZnO surface. The decrease in 'R$_{ct}$' minimizes the potential losses (Chamoun et al. 2015). The enhanced output current densities and enlarged area under the CV curve for the MoS$_2$-SnO$_2$/ZnO nanoparticles and the MoS$_2$-SnO$_2$/ZnO nanorods resulted from improved conductivity due to the SnO$_2$ nanoparticles on the ZnO surface. Besides, the large surface area offered by the MoS$_2$ nanosheets acted as the active sites for ZnO and electrolyte interactions (Yang et al. 2018). It is observed that the anodic peak potential shifted to a more negative value for the second and third cycles with respect to the first cycle. Similarly, the cathodic peak potential shifted to a less negative value that minimizes the difference between the anodic and the cathodic potential. As the difference between the anodic and the cathodic potential becomes smaller, the reversibility of the material is improved (Zeng et al. 2017).

It is important to note that the effect of the hydrogen evolution reaction was suppressed after the addition of MoS$_2$-SnO$_2$ nanocomposite. It is seen by the decrease in current density with respect to the bare ZnO samples at the end of the cathodic sweep. The cathodic current densities for all MoS$_2$-SnO$_2$/ZnO samples are higher than that derived

from HER activity. This is due to the high hydrogen evolution overpotential of the SnO_2 nanoparticles.

Table 7.3 Change in anodic and cathodic current densities for bare ZnO and MoS_2-SnO_2/ZnO samples

Reaction		ZnO NPs	ZnO NRs	ZnO MRs	MoS_2-SnO_2/ZnO NPs	MoS_2-SnO_2/ZnO NRs	MoS_2-SnO_2/ZnO MRs
Anodic	I_2/I_1	0.204	0.321	0.412	0.127	0.696	0.653
	I_3/I_1	0.131	0.159	0.205	0.052	0.493	0.485
Cathodic	I_2/I_1	0.364	0.624	0.814	0.113	0.778	0.702
	I_3/I_1	0.270	0.393	0.436	0.052	0.584	0.582

Table 7.3 shows the change in anodic and cathodic current densities for second and third cycles with respect to the first cycle. The I_2/I_1 and I_3/I_1 ratios are higher for the MoS_2-SnO_2/ZnO nanorods compared to the MoS_2-SnO_2/ZnO nanoparticles and the MoS_2-SnO_2/ZnO microrods. This indicates that the recyclability is higher for MoS_2-SnO_2/ZnO nanorods than MoS_2-SnO_2/ZnO nanoparticles and MoS_2-SnO_2/ZnO microrods.
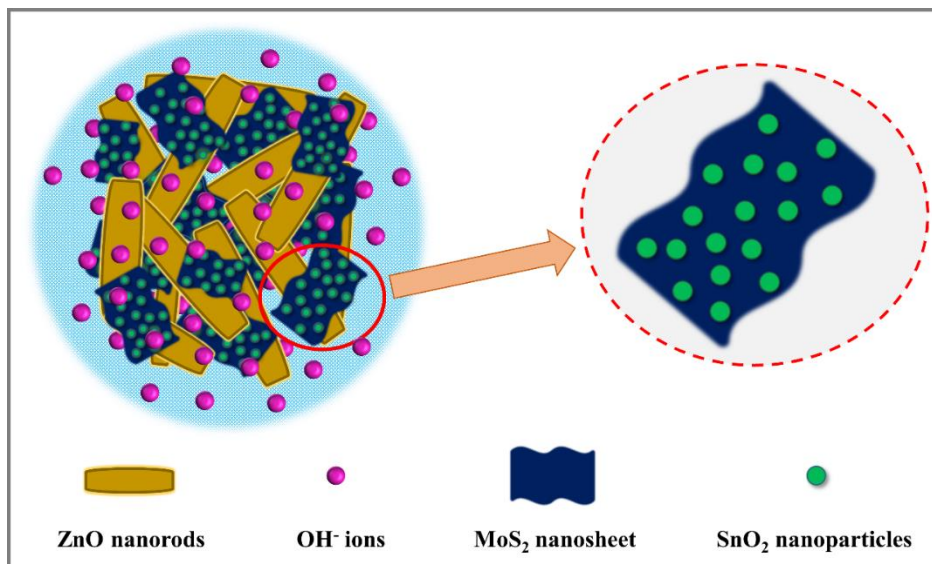
Figure 7.18 Interaction of the MoS_2-SnO_2/ZnO nanorods and the OH⁻ ions from the electrolyte

Figure 7.18 shows the interaction of MoS_2-SnO_2/ZnO nanorods and the OH⁻ ions from the electrolyte. The addition of MoS_2-SnO_2 nanocomposite to ZnO samples reduced charge-transfer resistance due to improved conductivity. The large surface area and conductivity offered by the MoS_2 nanosheets and SnO_2 nanoparticles helped to enhance the electrochemical activity of the ZnO. At the same time, the problem of corrosion and hydrogen evolution was minimized. Similar to the bare ZnO results, the MoS_2-SnO_2/ZnO nanorods showed better electrochemical performance than the MoS_2-SnO_2/ZnO nanoparticles and the MoS_2-SnO_2/ZnO microrods. Also, the MoS_2-SnO_2/ZnO nanorods showed significant improvement in suppressing HER activity, better anti-corrosion behaviour and enhanced output current density from the reduction and oxidation reactions.

7.5 Summary

The ZnO nanorods and the ZnO microrods were synthesised by microwave heating and hydrothermal method. The effect of size and morphology of the ZnO on its electrochemical performance in the KOH electrolyte was studied. The one-dimensional ZnO nanorods and microrods exhibited better stability and corrosion resistance than the ZnO nanoparticles with sphere-like and plate-like morphology. Among all bare ZnO

samples, the ZnO nanorods exhibited superior performance due to their high surface area and uniform rod morphology. The MoS_2-SnO_2 nanocomposite was prepared by functionalization of the SnO_2 nanoparticles on the surface of MoS_2 nanosheets. The influence of the MoS_2-SnO_2 as an additive to the ZnO was evaluated. The MoS_2-SnO_2 nanocomposite suppressed the hydrogen evolution reaction from the ZnO due to the high hydrogen overpotential of SnO_2. The MoS_2-SnO_2 passivated the ZnO surface that minimized the loss of zincate ions into the electrolyte, thus resulting in better anti-corrosion behaviour of the ZnO. The interaction between the ZnO and the electrolyte was improved by the larger area offered by the MoS_2 nanosheets. Also, the charge-transfer resistance of ZnO was decreased because of the conductive network formed by the MoS_2-SnO_2. These factors contributed in achieving higher output current density from the oxidation and reduction of the ZnO in the KOH electrolyte. The MoS_2-SnO_2/ZnO nanorods exhibited excellent performance amongst all ZnO based samples due to their high surface area and nanorod morphology along with the MoS_2-SnO_2 nanocomposite additive.

Publications from chapter 7

1. Prabukumar, C., Meti, S. and Bhat, K. U., "Enhancing the electrochemical performance of ZnO anode by novel additive of MoS_2-SnO_2 nanocomposite for the zinc alkaline battery application." Accepted for publication in *Journal of Materials Science: Materials in Electronics*, Manuscript ID: JMSE-D-21-01860R1.

CHAPTER 8

CONCLUSIONS

The present study focussed on transparent conductive silver nanowires films and ZnO anode for future electronics and energy storage devices. This work aimed to enhance the growth of silver nanowires (Ag NWs) with new oxygen scavenger, Mn(II) ions and improving the electrochemical performance of ZnO in aqueous KOH electrolyte by tailoring its morphology and with a novel MoS_2-SnO_2 additive.

The following conclusions are drawn from the results discussed in the previous chapters.

- Transparent conductive silver nanowires films were fabricated using the Ag NWs synthesised by the polyol method. The chloride conditions of $CuCl_2$ and $MnCl_2$ produced longer Ag NWs. This enhanced growth was due to the added Cu(II) ions or Mn(II) ions which acted as the oxygen scavenger to remove the atomic oxygen that blocked the active sites of the silver seed surfaces.

- The Ag NWs synthesised with the presence of Cu(II) ions (22 mM $CuCl_2$) showed the mean length and diameter of 7.2 µm and 151 nm, respectively. On the other hand, the Ag NWs synthesised with the presence of Mn(II) ions (22 mM $MnCl_2$) showed the mean length and diameter of 5.2 µm and 60 nm. The Ag NWs synthesised with $MnCl_2$ were thinner and more uniform in size (length and diameter) than those synthesised with $CuCl_2$. This was attributed to the effective removal of atomic oxygen from silver seed surfaces by the Mn(II) ions.

- The concentration of $MnCl_2$ was optimized by synthesising Ag NWs with three different concentrations of $MnCl_2$ (22 mM, 40 mM and 65 mM). The 40 mM $MnCl_2$ produced Ag NWs with a high aspect ratio. Its mean length and diameter were measured as 7.7 µm and 80 nm. The fabricated transparent conductive Ag NWs (40 mM $MnCl_2$) film exhibited the optical transmittance (%T_{550nm}) of 79% and the sheet resistance of 29 Ω/sq.

- The mechanical flexibility of Ag NWs film was superior to commercial ITO film. After 500 bending cycles, the Ag NWs film showed a minimal increase in

the sheet resistance compared to the ITO film. The Ag NWs film was proved as an excellent transparent film heater by generating a temperature of 90 °C at the applied voltage of 10 V.

- o The MoS_2 nanosheets were exfoliated by the ultrasonication-assisted method in the presence of PVP. The exfoliated MoS_2 nanosheets having a few-layer thickness were confirmed by electron microscopy (FESEM, TEM) and Raman spectroscopy. The exfoliated MoS_2 nanosheets showed a large surface area of $17 \ m^2 \ g^{-1}$.

- o The SnO_2 nanoparticles were synthesised by the solvothermal method. The synthesised SnO_2 nanoparticles had spherical-like morphology with a size range of 10 nm to 32 nm. The nanocomposite of exfoliated MoS_2 nanosheets and SnO_2 nanoparticles was prepared by functionalizing the SnO_2 nanoparticles onto the surface of MoS_2 nanosheets by the ligand exchange process.

- o The prepared MoS_2-SnO_2 nanocomposite was tested as the electrode material for supercapacitor application. The MoS_2 nanosheets significantly improved the electrochemical performance of the SnO_2 nanoparticles. The 5% MoS_2-SnO_2 showed best performance among all MoS_2-SnO_2 (0, 1, 2.5, 5 and 10% MoS_2) samples. The specific capacitance of SnO_2 nanoparticles was increased from 14 $F \ g^{-1}$ to 61 $F \ g^{-1}$ by functionalizing them on the surface of MoS_2 nanosheets.

- o The improved performance of the MoS_2-SnO_2 nanocomposite was attributed to the enhanced stability of SnO_2 nanoparticles by MoS_2 nanosheets. The MoS_2 nanosheets acted as the bridge between the SnO_2 nanoparticles. The large surface area of MoS_2 nanosheets enhanced the electrochemical interaction between the electrode and electrolyte.

- • The ZnO nanorods and microrods were synthesised by microwave heating and hydrothermal method, respectively, for the zinc alkaline battery application. Their performance in the KOH electrolyte was evaluated and compared to that of commercial ZnO nanoparticles having plate-like and sphere-like morphology.

- • The ZnO with one-dimensional rod morphology dissolved less in KOH solution than the commercial ZnO nanoparticles (NPs). The ZnO microrods (MRs) had the lowest solubility because of low surface interaction with KOH due to their

large diameter. The ZnO nanorods (NRs) were less soluble than the ZnO NPs owing to their smooth rod morphology with fewer edges and corners.

- The bare ZnO MRs showed better performance against hydrogen evolution and corrosion while the bare ZnO NPs were more prone to hydrogen evolution and corrosion. The ZnO NRs showed moderate hydrogen evolution and corrosion activities.

- The ZnO NRs showed highest electrochemical activity observed from cyclic voltammetry due to their low charge-transfer resistance, moderate resistance to solubility, hydrogen evolution, and corrosion in the KOH electrolyte.

- The addition of MoS_2-SnO_2 nanocomposite improved the electrochemical performance of the ZnO. The hydrogen evolution reaction was decreased for all MoS_2-SnO_2/ZnO hybrid samples because of the high hydrogen evolution overpotential of SnO_2. The surface of ZnO was passivated by MoS_2-SnO_2 that prevented the direct interaction with KOH electrolyte that minimized the corrosion of ZnO and the loss of zincate ions into the electrolyte.

- The charge transfer between ZnO and KOH electrolyte was improved by the MoS_2-SnO_2 nanocomposite addition that offered a large surface area and enhanced conductivity. Amongst all ZnO samples, the MoS_2-SnO_2/ZnO nanorods exhibited excellent electrochemical activity. It was observed by the increase in anodic and cathodic current densities in the cyclic voltammetry.

- The one-dimensional ZnO morphology with the MoS_2-SnO_2 nanocomposite addition makes the MoS_2-SnO_2/ZnO nanorods an excellent anode material for the zinc alkaline battery application.

Scope for the future work

In the present study, the silver nanowires were synthesised by the polyol method in the presence of Mn(II) ions. The silver nanowires were synthesised with different concentrations of $MnCl_2$ without changing any other synthesis parameters. The addition of $MnCl_2$ during the synthesis process produced thin, uniform-length silver nanowires with a high aspect ratio. The study on the ZnO anode for the alkaline battery was carried out by tailoring the size and morphology of ZnO. The electrochemical performance of ZnO with MoS_2-SnO_2 additive was evaluated. The ZnO nanorods with MoS_2-SnO_2 additive exhibited excellent electrochemical performance in the KOH electrolyte. Based on the findings from the present study, the following studies are derived for future work.

- Multistep synthesis of silver nanowires using high molecular weight PVP with $MnCl_2$, KBr in high pressure or nitrogen gas environment to produce long and thin silver nanowires.
- Fabrication of Zn-Ag coin cell battery using MoS_2-SnO_2/ZnO as the anode and silver nanowires as the cathode.
- Fabrication of Zn-Ag thin-film battery with sol-gel polymer/KOH electrolyte
- Performance evaluation of the fabricated Zn-Ag coin cell and Zn-Ag thin-film batteries.

REFERENCES

Abbasi, N. M., Wang, L., Yu, H., Zain-ul-Abdin, Akram, M., Khalid, H., Yongshen, C., Sun, R., Saleem, M., and Deng, Z. (2016). "Glycerol and Water Mediated Synthesis of Silver Nanowires in the Presence of Cobalt Chloride as Growth Promoting Additive." *J. Inorg. Organomet. Polym. Mater.*, 26(3), 680–690.

Abel, B., Coskun, S., Mohammed, M., Williams, R., Unalan, H. E., and Aslan, K. (2015). "Metal-enhanced fluorescence from silver nanowires with high aspect ratio on glass slides for biosensing applications." *J. Phys. Chem. C*, 119(1), 675–684.

Acerce, M., Voiry, D., and Chhowalla, M. (2015). "Metallic 1T phase MoS_2 nanosheets as supercapacitor electrode materials." *Nat. Nanotechnol.*, 10(4), 313–318.

Akti, F. (2018). "Photocatalytic degradation of remazol yellow using polyaniline–doped tin oxide hybrid photocatalysts with diatomite support." *Appl. Surf. Sci.*, 455, 931–939.

Al-Hamdi, A. M., Rinner, U., and Sillanpää, M. (2017). "Tin dioxide as a photocatalyst for water treatment: A review." *Process Saf. Environ. Prot.*, 107, 190–205.

Alamro, T., and Ram, M. K. (2017). "Polyethylenedioxythiophene and molybdenum disulfide nanocomposite electrodes for supercapacitor applications." *Electrochim. Acta*, 235, 623–631.

Amendola, V., Pilot, R., Frasconi, M., Maragò, O. M., and Iatì, M. A. (2017). "Surface plasmon resonance in gold nanoparticles: A review." *J. Phys. Condens. Matter*, 29(20).

Amjadi, M., Pichitpajongkit, A., Lee, S., Ryu, S., and Park, I. (2014). "Highly stretchable and sensitive strain sensor based on silver nanowire-elastomer nanocomposite." *ACS Nano*, 8(5), 5154–5163.

Anbazhagan, R., Wang, H. J., Tsai, H. C., and Jeng, R. J. (2014). "Highly concentrated MoS_2 nanosheets in water achieved by thioglycolic acid as stabilizer and used as biomarkers." *RSC Adv.*, 4(81), 42936–42941.

Azani, M. R., and Hassanpour, A. (2019). "Synthesis of Silver Nanowires with Controllable Diameter and Simple Tool to Evaluate their Diameter, Concentration and Yield." *ChemistrySelect*, 4(9), 2716–2720.

Baletto, F., and Ferrando, R. (2005). "Structural properties of nanoclusters: Energetic, thermodynamic, and kinetic effects." *Rev. Mod. Phys.*, 77(1), 371–423.

Bansal, S., Pandya, D. K., and Kashyap, S. C. (2012). "Charge transport mechanism in high conductivity undoped tin oxide thin films deposited by reactive sputtering." *Thin Solid Films*, 524, 30–34.

Berchmans, S., Bandodkar, A. J., Jia, W., Ramírez, J., Meng, Y. S., and Wang, J. (2014). "An epidermal alkaline rechargeable Ag-Zn printable tattoo battery for wearable electronics." *J. Mater. Chem.* A, 2(38), 15788–15795.

Bertolazzi, S., Brivio, J., and Kis, A. (2011). "Stretching and breaking of ultrathin MoS2." *ACS Nano*, 5(12), 9703–9709.

Bid, A., Bora, A., and Raychaudhuri, A. K. (2006). "Temperature dependence of the resistance of metallic nanowires of diameter ≥15 nm: Applicability of Bloch-Grüneisen theorem." *Phys. Rev. B - Condens. Matter Mater. Phys.*, 74(3), 035426.

Birrozzi, A., Raccichini, R., Nobili, F., Marinaro, M., Tossici, R., and Marassi, R. (2014). "High-stability graphene nano sheets/SnO_2 composite anode for lithium ion batteries." *Electrochim. Acta*, 137, 228–234.

Bob, B., Machness, A., Song, T. Bin, Zhou, H., Chung, C. H., and Yang, Y. (2016). "Silver nanowires with semiconducting ligands for low-temperature transparent conductors." *Nano Res.*, 9(2), 392–400.

Bonu, V., Gupta, B., Chandra, S., Das, A., Dhara, S., and Tyagi, A. K. (2016). "Electrochemical supercapacitor performance of SnO_2 quantum dots." *Electrochim. Acta*, 203, 230–237.

Brousse, T., Retoux, R., Herterich, U., and Schleich, D. M. (1998). "Thin-Film Crystalline SnO_2-Lithium Electrodes." *J. Electrochem. Soc.*, 145(1), 1–4.

Brunetti, F., Operamolla, A., Castro-Hermosa, S., Lucarelli, G., Manca, V., Farinola, G. M., and Brown, T. M. (2019). "Printed Solar Cells and Energy Storage Devices on Paper Substrates." *Adv. Funct. Mater.*, 29(21).

Chamoun, M., Hertzberg, B. J., Gupta, T., Davies, D., Bhadra, S., Tassell, B. Van, Erdonmez, C., and Steingart, D. A. (2015). "Hyper-dendritic nanoporous zinc foam anodes." *NPG Asia Mater.*, 7(4), e178-8.

Chang, M. H., Cho, H. A., Kim, Y. S., Lee, E. J., and Kim, J. Y. (2014). "Thin and long silver nanowires self-assembled in ionic liquids as a soft template: Electrical and optical properties." *Nanoscale Res. Lett.*, 9(1), 1–7.

Chang, Y.-H., Lu, Y.-C., and Chou, K.-S. (2011). "Diameter Control of Silver Nanowires by Chloride Ions and Its Application as Transparent Conductive Coating." *Chem. Lett.*, 40(12), 1352–1353.

Chen, P., Wu, Y., Zhang, Y., Wu, T. H., Ma, Y., Pelkowski, C., Yang, H., Zhang, Y., Hu, X., and Liu, N. (2018). "A deeply rechargeable zinc anode with pomegranate-inspired nanostructure for high-energy aqueous batteries." *J. Mater. Chem.* A, 6(44), 21933–21940.

Chen, Y., Lu, J., Wen, S., Lu, L., and Xue, J. (2014). "Synthesis of SnO_2/MoS_2 composites with different component ratios and their applications as lithium ion battery anodes." *J. Mater. Chem. A*, 2(42), 17857–17866.

Chen, Z., Cotterell, B., Wang, W., Guenther, E., and Chua, S. J. (2001). "A mechanical assessment of flexible optoelectronic devices." *Thin Solid Films*, 394(1–2), 201–205.

Choi, D. Y., Kang, H. W., Sung, H. J., and Kim, S. S. (2013). "Annealing-free, flexible silver nanowire-polymer composite electrodes via a continuous two-step spray-coating method." *Nanoscale*, 5(3), 977–983.

Choi, W., Cho, M. Y., Konar, A., Lee, J. H., Cha, G. B., Hong, S. C., Kim, S., Kim, J., Jena, D., Joo, J., and Kim, S. (2012). "High-detectivity multilayer MoS_2 phototransistors with spectral response from ultraviolet to infrared." *Adv. Mater.*, 24(43), 5832–5836.

Chung, W. Y., Kim, T. H., Hong, Y. H., and Lee, D. D. (1995). "Characterization of porous tin oxide thin films and their application to microsensor fabrication." *Sensors Actuators B. Chem.*, 25(1–3), 482–485.

Coleman, J. N., Lotya, M., O'Neill, A., Bergin, S. D., King, P. J., Khan, U., Young, K., Gaucher, A., De, S., Smith, R. J., Shvets, I. V., Arora, S. K., Stanton, G., Kim, H. Y., Lee, K., Kim, G. T., Duesberg, G. S., Hallam, T., Boland, J. J., Wang, J. J., Donegan, J. F., Grunlan, J. C., Moriarty, G., Shmeliov, A., Nicholls, R. J., Perkins, J. M., Grieveson, E. M., Theuwissen, K., McComb, D. W., Nellist, P. D., and Nicolosi, V. (2011). "Two-dimensional nanosheets produced by liquid exfoliation of layered materials." *Science*, 331(6017), 568–571.

Coskun, S., Aksoy, B., and Unalan, H. E. (2011). "Polyol synthesis of silver nanowires: An extensive parametric study." *Cryst. Growth Des.*, 11(11), 4963–4969.

Coskun, S., Selen Ates, E., and Emrah Unalan, H. (2013). "Optimization of silver nanowire networks for polymer light emitting diode electrodes." *Nanotechnology*, 24(12), 125202.

Courtney, I. A., and Dahn, J. R. (1997). "Electrochemical and In Situ X-Ray Diffraction Studies of the Reaction of Lithium with Tin Oxide Composites." *J. Electrochem. Soc.*, 144(6), 2045–2052.

Cui, C., Li, M., Zhou, X., and Zhang, X. (2019). "Synthesis of ZnO/carbon nanotube composites for enhanced electrochemical performance of Ni-Zn secondary batteries." *Mater. Res. Bull.*, 112, 261–268.

Davies, G., Hsieh, A. G., Hultmark, M., Mueller, M. E., and Steingart, D. A. (2016). "Utilization of Hyper-Dendritic Zinc during High Rate Discharge in Alkaline Electrolytes." *J. Electrochem. Soc.*, 163(7), A1340–A1347.

Du, G., Guo, Z., Wang, S., Zeng, R., Chen, Z., and Liu, H. (2010). "Superior stability and high capacity of restacked molybdenum disulfide as anode material for lithium ion batteries." *Chem. Commun.*, 46(7), 1106–1108.

Dundálek, J., Šnajdr, I., Libánský, O., Vrána, J., Pocedič, J., Mazúr, P., and Kosek, J. (2017). "Zinc electrodeposition from flowing alkaline zincate solutions: Role of hydrogen evolution reaction." *J. Power Sources*, 372, 221–226.

Dungey, K. E., Curtis, M. D., and Penner-Hahn, J. E. (1998). "Structural Characterization and Thermal Stability of MoS_2 Intercalation Compounds." *Chem. Mater.*, 10(8), 2152–2161.

Eda, G., Yamaguchi, H., Voiry, D., Fujita, T., Chen, M., and Chhowalla, M. (2011). "Photoluminescence from chemically exfoliated MoS_2." *Nano Lett.*, 11(12), 5111–5116.

Elrouby, M., –Shafy Shilkamy, H. A. El, and Elsayed, A. (2021). "Development of the electrochemical performance of zinc via alloying with indium as anode for alkaline batteries application." *J. Alloys Compd.*, 854, 157285.

Etacheri, V., Seisenbaeva, G. A., Caruthers, J., Daniel, G., Nedelec, J. M., Kessler, V. G., and Pol, V. G. (2015). "Ordered network of interconnected SnO_2 nanoparticles for excellent lithium-ion storage." *Adv. Energy Mater.*, 5(5), 2–9.

Fan, L. Q., Liu, G. J., Zhang, C. Y., Wu, J. H., and Wei, Y. L. (2015). "Facile one-step hydrothermal preparation of molybdenum disulfide/carbon composite for use in supercapacitor." *Int. J. Hydrogen Energy*, 40(32), 10150–10157.

Fan, X., Yang, Z., Wen, R., Yang, B., and Long, W. (2013). "The application of Zn-Al-hydrotalcite as a novel anodic material for Ni-Zn secondary cells." *J. Power Sources*, 224, 80–85.

Feng, Z., Yang, Z., Huang, J., Xie, X., and Zhang, Z. (2014). "Influences of Zn-Sn-Al-Hydrotalcite Additive on the Electrochemical Performances of ZnO for Zinc-Nickel Secondary Cells." *J. Electrochem. Soc.*, 161(14), A1981–A1986.

Fukagawa, H., Sasaki, T., Tsuzuki, T., Nakajima, Y., Takei, T., Motomura, G., Hasegawa, M., Morii, K., and Shimizu, T. (2018). "Long-Lived Flexible Displays Employing Efficient and Stable Inverted Organic Light-Emitting Diodes." *Adv. Mater.*, 30(28), 1–7.

Gallaway, J. W., Gaikwad, A. M., Hertzberg, B., Erdonmez, C. K., Chen-Wiegart, Y. C. K., Sviridov, L. A., Evans-Lutterodt, K., Wang, J., Banerjee, S., and Steingartb, D. A. (2014). "An In Situ Synchrotron Study of Zinc Anode Planarization by a Bismuth Additive." *J. Electrochem. Soc.*, 161(3), A275–A284.

Gao, Y., Jiang, P., Song, L., Liu, L., Yan, X., Zhou, Z., Liu, D., Wang, J., Yuan, H., Zhang, Z., Zhao, X., Dou, X., Zhou, W., Wang, G., and Xie, S. (2005). "Growth mechanism of silver nanowires synthesized by polyvinylpyrrolidone-assisted polyol reduction." *J. Phys. D. Appl. Phys.*, 38(7), 1061–1067.

Gao, Y., Xie, C., and Zheng, Z. (2021). "Textile Composite Electrodes for Flexible Batteries and Supercapacitors: Opportunities and Challenges." *Adv. Energy Mater.*, 11(3), 1–9.

Govindaraj, A., Satishkumar, B. C., Nath, M., and Rao, C. N. R. (2000). "Metal nanowires and intercalated metal layers in single-walled carbon nanotube bundles." *Chem. Mater.*, 12(1), 202–205.

Gupta, A., Arunachalam, V., and Vasudevan, S. (2016). "Liquid-Phase Exfoliation of MoS_2 Nanosheets: The Critical Role of Trace Water." J. Phys. Chem. Lett., 7(23), 4884–4890.

Gupta, D., Chauhan, V., and Kumar, R. (2020). "A comprehensive review on synthesis and applications of molybdenum disulfide (MoS_2) material: Past and recent developments." *Inorg. Chem. Commun.*, 121(August), 108200.

Ha, B., and Jo, S. (2017). "Hybrid Ag nanowire transparent conductive electrodes with randomly oriented and grid-patterned Ag nanowire networks." *Sci. Rep.*, 7(1), 1–8.

Haacke, G. (1976). "New figure of merit for transparent conductors." *J. Appl. Phys.*, 47(9), 4086–4089.

Hecht, D., Hu, L., and Grüner, G. (2006). "Conductivity scaling with bundle length and diameter in single walled carbon nanotube networks." *Appl. Phys. Lett.*, 89(13), 133112.

Hota, P., Miah, M., Bose, S., Dinda, D., Ghorai, U. K., Su, Y. K., and Saha, S. K. (2020). "Ultra-small amorphous MoS_2 decorated reduced graphene oxide for supercapacitor application." *J. Mater. Sci. Technol.*, 40, 196–203.

Hu, L., Kim, H. S., Lee, J. Y., Peumans, P., and Cui, Y. (2010). "Scalable coating and properties of transparent, flexible, silver nanowire electrodes." *ACS Nano*, 4(5), 2955–2963.

Huang, J., and Yang, Z. (2014). "Improved cycling performance of cellular sheet-like carbon-coated ZnO as anode material for Zn/Ni secondary battery." *ECS Electrochem. Lett.*, 3(11), A116–A119.

Huang, J., Yang, Z., and Wang, T. (2014a). "Evaluation of tetraphenylporphyrin modified ZnO as anode material for Ni-Zn rechargeable battery." *Electrochim. Acta*, 123, 278–284.

Huang, K. J., Wang, L., Liu, Y. J., Wang, H. B., Liu, Y. M., and Wang, L. L. (2013). "Synthesis of polyaniline/2-dimensional graphene analog MoS_2 composites for high-performance supercapacitor." *Electrochim. Acta*, 109, 587–594.

Huang, K. J., Zhang, J. Z., Shi, G. W., and Liu, Y. M. (2014b). "Hydrothermal synthesis of molybdenum disulfide nanosheets as supercapacitors electrode material." *Electrochim. Acta*, 132, 397–403.

Huang, M., Chen, H., He, J., An, B., Sun, L., Li, Y., Ren, X., Deng, L., and Zhang, P. (2019a). "Ultra small few layer MoS_2 embedded into three-dimensional macro-micro-mesoporous carbon as a high performance lithium ion batteries anode with superior lithium storage capacity." *Electrochim. Acta*, 317, 638–647.

Huang, X., Liu, J., Ding, J., Deng, Y., Hu, W., and Zhong, C. (2019b). "Toward Flexible and Wearable Zn-Air Batteries from Cotton Textile Waste." *ACS Omega*, 4(21), 19341–19349.

Hwang, B., Lee, J., Trung, T. Q., Roh, E., Kim, D., Kim, S., and Lee, N. (2015). "Transparent Stretchable Self-Powered Patchable Sensor Platform with Ultrasensitive Recognition of Human Activities." *ACS Nano*, 9(9), 8801–8810.

Hyning, D. L. Van, and Zukoski, C. F. (1998). "Formation Mechanisms and Aggregation Behavior of Borohydride Reduced Silver Particles." *Langmuir*, 14(24), 7034–7046.

Im, Y., Kang, S., Kwak, B. S., Park, K. S., Cho, T. W., Lee, J. S., and Kang, M. (2016). "Electrochemical performance of three shaped ZnO nanoparticles prepared in LiOH, NaOH and KOH alkaline solutions as anodic materials for Ni/Zn redox batteries." *Korean J. Chem. Eng*., 33(4), 1447–1455.

Ingole, S. M., Navale, Y. H., Bandgar, D. K., Patil, V. B., Navale, S. T., Stadler, F. J., Ramgir, N. S., Gupta, S. K., Aswal, D. K., and Mane, R. S. (2017). "Nanostructured tin oxide films: Physical synthesis, characterization, and gas sensing properties." *J. Colloid Interface Sci.*, 493(2), 162–170.

Jang, H. W., Hwang, B. Y., Lee, K. W., Kim, Y. M., and Kim, J. Y. (2018). "Controlling the size of silver nanowires produced by a tetrabutylammonium dichlorobromide salt-based polyol process: Kinetics of silver crystal growth." *AIP Adv*., 8(2).

Jang, H. W., Kim, Y. H., Lee, K. W., Kim, Y. M., and Kim, J. Y. (2017). "Research Update: Synthesis of sub-15-nm diameter silver nanowires through a water-based hydrothermal method: Fabrication of low-haze 2D conductive films." *APL Mater*., 5(8).

Jarrett, R., and Crook, R. (2016). "Silver nanowire purification and separation by size and shape using multi-pass filtration." *Mater. Res. Innov*., 20(2), 86–91.

Ji, H. M., Luan, A. L., Dai, C. C., Man Li, Yang, G., and Hou, W. H. (2019). "Highly active free-standing and flexible MoS_2/rGO sandwich-structured films for supercapacitor applications." *Solid State Commun*., 297(May), 45–49.

Jiu, J., Murai, K., Kim, D., Kim, K., and Suganuma, K. (2009). "Preparation of Ag nanorods with high yield by polyol process." *Mater. Chem. Phys*., 114(1), 333–338.

Joensen, P., Frindt, R. F., and Morrison, S. R. (1986). "Single-layer MoS_2." *Mater. Res. Bull*., 21(4), 457–461.

Kang, S. B., Noh, Y. J., Na, S. I., and Kim, H. K. (2014). "Brush-painted flexible organic solar cells using highly transparent and flexible Ag nanowire network electrodes." *Sol. Energy Mater. Sol. Cells*, 122, 152–157.

Karpinski, A. P., Makovetski, B., Russell, S. J., Serenyi, J. R., and Williams, D. C. (1999). "Silver-zinc: Status of technology and applications." *J. Power Sources*, 80(1), 53–60.

Kim, K. H., Koo, B. R., and Ahn, H. J. (2018). "Sheet resistance dependence of fluorine-doped tin oxide films for high-performance electrochromic devices." *Ceram. Int.*, 44(8), 9408–9413.

Korte, K. E., Skrabalak, S. E., and Xia, Y. (2008). "Rapid synthesis of silver nanowires through a CuCl- or $CuCl_2$-mediated polyol process." *J. Mater. Chem.*, 18(4), 437–441.

Krishnamoorthy, K., Pazhamalai, P., Veerasubramani, G. K., and Kim, S. J. (2016). "Mechanically delaminated few layered MoS_2 nanosheets based high performance wire type solid-state symmetric supercapacitors." *J. Power Sources*, 321, 112–119.

Kwak, B. S., Jo, S. W., Park, K. S., Cho, T. W., Jeon, J., Chung, K. il, and Kang, M. (2017). "Synthesis of microcrystalline ZnO as an anodic material via a solvothermal method, and its electrochemical performance in Ni/Zn redox battery." *J. Ind. Eng. Chem.*, 46, 111–118.

Kwon, J., Ki Hong, Y., Kwon, H. J., Jin Park, Y., Yoo, B., Kim, J., Grigoropoulos, C. P., Suk Oh, M., and Kim, S. (2015). "Optically transparent thin-film transistors based on 2D multilayer MoS_2 and indium zinc oxide electrodes." *Nanotechnology*, 26(3), 035202.

Langley, D., Giusti, G., Mayousse, C., Celle, C., Bellet, D., and Simonato, J. P. (2013). "Flexible transparent conductive materials based on silver nanowire networks: A review." *Nanotechnology*, 24(45), 452001.

Langley, D. P., Lagrange, M., Giusti, G., Jiménez, C., Bréchet, Y., Nguyen, N. D., and Bellet, D. (2014). "Metallic nanowire networks: Effects of thermal annealing on electrical resistance." *Nanoscale*, 6(22), 13535–13543.

Larcher, D., Gérand, B., and Tarascon, J. M. (2000). "Low temperature synthesis of γ-Li$_{(x)}$MnO$_2$ powders in ethylene glycol." *Int. J. Inorg. Mater.*, 2(5), 389–396.

Lee, D., Bang, G., Byun, M., and Choi, D. (2020). "Highly flexible, transparent and conductive ultrathin silver film heaters for wearable electronics applications." *Thin Solid Films*, 697, 137835.

Lee, J. H., Lee, P., Lee, D., Lee, S. S., and Ko, S. H. (2012a). "Large-scale synthesis and characterization of very long silver nanowires via successive multistep growth." *Cryst. Growth Des.*, 12(11), 5598–5605.

Lee, J., Lee, P., Lee, H., Lee, D., Lee, S. S., and Ko, S. H. (2012b). "Very long Ag nanowire synthesis and its application in a highly transparent, conductive and flexible metal electrode touch panel." *Nanoscale*, 4(20), 6408–6414.

Lee, J. Y., Connor, S. T., Cui, Y., and Peumans, P. (2008). "Solution-processed metal nanowire mesh transparent electrodes." *Nano Lett.*, 8(2), 689–692.

Lee, S. M., Kim, Y. J., Eom, S. W., Choi, N. S., Kim, K. W., and Cho, S. B. (2013). "Improvement in self-discharge of Zn anode by applying surface modification for Zn-air batteries with high energy density." *J. Power Sources*, 227, 177–184.

Lee, Y. H., Zhang, X. Q., Zhang, W., Chang, M. T., Lin, C. Te, Chang, K. Di, Yu, Y. C., Wang, J. T. W., Chang, C. S., Li, L. J., and Lin, T. W. (2012c). "Synthesis of large-area MoS$_2$ atomic layers with chemical vapor deposition." *Adv. Mater.*, 24(17), 2320–2325.

Li, B., Ye, S., Stewart, I. E., Alvarez, S., and Wiley, B. J. (2015). "Synthesis and Purification of Silver Nanowires to Make Conducting Films with a Transmittance of 99%." *Nano Lett.*, 15(10), 6722–6726.

Li, J., Tang, W., Yang, H., Dong, Z., Huang, J., Li, S., Wang, J., Jin, J., and Ma, J. (2014). "Enhanced-electrocatalytic activity of Ni$_{1-x}$Fe$_x$ alloy supported on polyethyleneimine functionalized MoS$_2$ nanosheets for hydrazine oxidation." *RSC Adv.*, 4(4), 1988–1995.

Li, W., Wang, K., Zhou, M., Zhan, H., Cheng, S., and Jiang, K. (2018). "Advanced Low-Cost, High-Voltage, Long-Life Aqueous Hybrid Sodium/Zinc Batteries Enabled by a Dendrite-Free Zinc Anode and Concentrated Electrolyte." *ACS Appl. Mater. Interfaces*, 10(26), 22059–22066.

Li, Y., and Dai, H. (2014). "Recent advances in Zinc-air batteries." *Chem. Soc. Rev.*, 43(15), 5257–5275.

Liang, D., Tian, Z., Liu, J., Ye, Y., Wu, S., Cai, Y., and Liang, C. (2015). "MoS_2 nanosheets decorated with ultrafine Co_3O_4 nanoparticles for high-performance electrochemical capacitors." *Electrochim. Acta*, 182, 376–382.

Liang, S., Zhou, J., Liu, J., Pan, A., Tang, Y., Chen, T., and Fang, G. (2013). "PVP-assisted synthesis of MoS_2 nanosheets with improved lithium storage properties." *CrystEngComm*, 15(25), 4998–5002.

Liao, F., Guo, Z., Wang, Y., Xie, Y., Zhang, S., Sheng, Y., Tang, H., Xu, Z., Riaud, A., Zhou, P., Wan, J., Fuhrer, M. S., Jiang, X., Zhang, D. W., Chai, Y., and Bao, W. (2020). "High-performance logic and memory devices based on a dual-gated MoS_2 architecture." *ACS Appl. Electron. Mater.*, 2(1), 111–119.

Liao, F., Sheng, Y., Guo, Z., Tang, H., Wang, Y., Zong, L., Chen, X., Riaud, A., Zhu, J., Xie, Y., Chen, L., Zhu, H., Sun, Q., Zhou, P., Jiang, X., Wan, J., Bao, W., and Zhang, D. W. (2019). "MoS_2 dual-gate transistors with electrostatically doped contacts." *Nano Res.*, 12(10), 2515–2519.

Liu, J., Zeng, Z., Cao, X., Lu, G., Wang, L. H., Fan, Q. L., Huang, W., and Zhang, H. (2012). "Preparation of MoS_2-polyvinylpyrrolidone nanocomposites for flexible nonvolatile rewritable memory devices with reduced graphene oxide electrodes." *Small*, 8(22), 3517–3522.

Liu, M., Pu, X., Cong, Z., Liu, Z., Liu, T., Chen, Y., Fu, J., Hu, W., and Wang, Z. L. (2019). "Resist-Dyed Textile Alkaline Zn Microbatteries with Significantly Suppressed Zn Dendrite Growth." *ACS Appl. Mater. Interfaces*, 11(5), 5095–5106.

Liu, S., Wang, Z., Zhang, Y., Li, J., and Zhang, T. (2016). "Sulfonated graphene anchored with tin oxide nanoparticles for detection of nitrogen dioxide at room temperature with enhanced sensing performances." *Sensors Actuators, B Chem.*, 228(2), 134–143.

Liu, X., Wang, T., Hu, G., Xu, C., Xiong, Y., and Wang, Y. (2018). "Controllable synthesis of self-assembled MoS_2 hollow spheres for photocatalytic application." *J. Mater. Sci. Mater. Electron.*, 29(1), 753–761.

Liu, Z., Cao, Z., Deng, B., Wang, Y., Shao, J., Kumar, P., Liu, C. R., Wei, B., and Cheng, G. J. (2014). "Ultrafast and scalable laser liquid synthesis of tin oxide nanotubes and its application in lithium ion batteries." *Nanoscale*, 6(11), 5853–5858.

Long, J., Yang, Z., Huang, J., and Zeng, X. (2017a). "Self-assembly of exfoliated layered double hydroxide and graphene nanosheets for electrochemical energy storage in zinc/nickel secondary batteries." *J. Power Sources*, 359, 111–118.

Long, J., Yang, Z., Zeng, X., and Huang, J. (2016). "A new class of nanocomposites of Zn-Al-Bi layered double oxides: Large reversible capacity and better cycle performance for alkaline secondary batteries." *RSC Adv.*, 6(95), 92896–92904.

Long, J., Yang, Z., Zhang, Z., and Huang, J. (2017b). "Sheet-like carbon-coated Zn-Al-Bi layered double oxides nanocomposites enabling high performance for rechargeable alkaline batteries." J. *Electrochem. Soc.*, 164(13), A3068–A3074.

Lou, X. W., Wang, Y., Yuan, C., Lee, J. Y., and Archer, L. A. (2006). "Template-free synthesis of SnO_2 hollow nanostructures with high lithium storage capacity." *Adv. Mater.*, 18(17), 2325–2329.

Ma, H., Li, C., Su, Y., and Chen, J. (2007). "Studies on the vapour-transport synthesis and electrochemical properties of zinc micro-, meso- and nanoscale structures." *J. Mater. Chem.*, 17(7), 684–691.

Ma, J., and Zhan, M. (2014). "Rapid production of silver nanowires based on high concentration of $AgNO_3$ precursor and use of $FeCl_3$ as reaction promoter." *RSC Adv.*, 4(40), 21060–21071.

Ma, M., Tu, J. P., Yuan, Y. F., Wang, X. L., Li, K. F., Mao, F., and Zeng, Z. Y. (2008). "Electrochemical performance of ZnO nanoplates as anode materials for Ni/Zn secondary batteries." *J. Power Sources*, 179(1), 395–400.

Ma, X., and Shi, M. (2013). "Thermal Evaporation Deposition of Few-layer MoS_2 Films." *Nano-Micro Lett.*, 5(2), 135–139.

Madeira, A., Papanastasiou, D. T., Toupance, T., Servant, L., Tréguer-Delapierre, M., Bellet, D., and Goldthorpe, I. A. (2020). "Rapid synthesis of ultra-long silver nanowires for high performance transparent electrodes." *Nanoscale Adv.*, 2(9), 3804–3808.

Mainar, A. R., Colmenares, L. C., Blázquez, J. A., and Urdampilleta, I. (2018a). "A brief overview of secondary zinc anode development: The key of improving zinc-based energy storage systems." *Int. J. Energy Res.*, 42(3), 903–918.

Mainar, A. R., Iruin, E., Colmenares, L. C., Kvasha, A., Meatza, I. de, Bengoechea, M., Leonet, O., Boyano, I., Zhang, Z., and Blazquez, J. A. (2018b). "An overview of progress in electrolytes for secondary zinc-air batteries and other storage systems based on zinc." *J. Energy Storage*, 15, 304–328.

Manikandan, V., Petrila, I., Vigneselvan, S., Mane, R. S., Vasile, B., Dharmavarapu, R., Lundgaard, S., Juodkazis, S., and Chandrasekaran, J. (2020). "A reliable chemiresistive sensor of nickel-doped tin oxide (Ni-SnO_2) for sensing carbon dioxide gas and humidity." *RSC Adv.*, 10(7), 3796–3804.

Mishra, A. K., Lakshmi, K. V., and Huang, L. (2015). "Eco-friendly synthesis of metal dichalcogenides nanosheets and their environmental remediation potential driven by visible light." *Sci. Rep.*, 5, 15718.

Mogne, T. Le, Donnet, C., Martin, J. M., Tonck, A., Millard-Pinard, N., Fayeulle, S., and Moncoffre, N. (1994). "Nature of super-lubricating MoS_2 physical vapor deposition coatings." *J. Vac. Sci. Technol. A Vacuum, Surfaces, Film.*, 12(4), 1998–2004.

Moser, F., Fourgeot, F., Rouget, R., Crosnier, O., and Brousse, T. (2013). "In situ X-ray diffraction investigation of zinc based electrode in Ni-Znsecondary batteries." *Electrochim. Acta*, 109, 110–116.

Mutiso, R. M., Sherrott, M. C., Rathmell, A. R., Wiley, B. J., and Winey, K. I. (2013). "Integrating simulations and experiments to predict sheet resistance and optical transmittance in nanowire films for transparent conductors." *ACS nano*, 7(9), 7654-7663.

Najjar, M., Hosseini, H. A., Masoudi, A., Hashemzadeh, A., and Darroudi, M. (2020). "Preparation of tin oxide (IV) nanoparticles by a green chemistry method and investigation of its role in the removal of organic dyes in water purification." *Res. Chem. Intermed.*, 46(4), 2155–2168.

Nam, S., Song, M., Kim, D. H., Cho, B., Lee, H. M., Kwon, J. D., Park, S. G., Nam, K. S., Jeong, Y., Kwon, S. H., Park, Y. C., Jin, S. H., Kang, J. W., Jo, S., and Kim, C. S. (2014). "Ultrasmooth, extremely deformable and shape recoverable Ag nanowire embedded transparent electrode." *Sci. Rep.*, 4, 4788.

Narayanan, T. N., Vusa, C. S. R., and Alwarappan, S. (2014). "Selective and efficient electrochemical biosensing of ultrathin molybdenum disulfide sheets." *Nanotechnology*, 25(33), 335702.

Niu, Z., Cui, F., Kuttner, E., Xie, C., Chen, H., Sun, Y., Dehestani, A., Schierle-Arndt, K., and Yang, P. (2018). "Synthesis of Silver Nanowires with Reduced Diameters Using Benzoin-Derived Radicals to Make Transparent Conductors with High Transparency and Low Haze." *Nano Lett.*, 18(8), 5329–5334.

Novoselov, K. S., Geim, A. K., Morozov, S. V., Jiang, D., Zhang, Y., Dubonos, S. V., Grigorieva, I. V., and Firsov, A. A. (2004). "Electric field in atomically thin carbon films." *Science*, 306(5696), 666–669.

Oliveira, C. C. S. De, Ando, R. A., and Camargo, P. H. C. (2013). "Size-controlled synthesis of silver micro/nanowires as enabled by HCL oxidative etching." *Phys. Chem. Chem. Phys.*, 15(6), 1887–1893.

Ozgit, D., Hiralal, P., and Amaratunga, G. A. J. (2014). "Improving performance and cyclability of zinc-silver oxide batteries by using graphene as a two dimensional conductive additive." *ACS Appl. Mater. Interfaces*, 6(23), 20752–20757.

Pal, B., Yang, S., Ramesh, S., Thangadurai, V., and Jose, R. (2019). "Electrolyte selection for supercapacitive devices: A critical review." *Nanoscale Adv*., 1(10), 3807–3835.

Pan, Q. C., Huang, Y. G., Wang, H. Q., Yang, G. H., Wang, L. C., Chen, J., Zan, Y. H., and Li, Q. Y. (2016). "MoS2/C nanosheets Encapsulated Sn@SnOx nanoparticles as high-performance Lithium-iom battery anode material." *Electrochim. Acta*, 197, 50–57.

Panth, M., Cook, B., Zhang, Y., Ewing, D., Tramble, A., Wilson, A., and Wu, J. (2020). "High-Performance Strain Sensors Based on Vertically Aligned Piezoelectric Zinc Oxide Nanowire Array/Graphene Nanohybrids." *ACS Appl. Nano Mater*., 3(7), 6711–6718.

Park, J., Han, D., Choi, S., Kim, Y., and Kwak, J. (2019). "Flexible transparent film heaters using a ternary composite of silver nanowire, conducting polymer, and conductive oxide." *RSC Adv*., 9(10), 5731–5737.

Parker, J. F., Chervin, C. N., Nelson, E. S., Rolison, D. R., and Long, J. W. (2014). "Wiring zinc in three dimensions re-writes battery performance - Dendrite-free cycling." *Energy Environ. Sci*., 7(3), 1117–1124.

Peng, K., Zhang, Z., Zhao, Z., Yang, C., Tian, Z., and Lai, Y. (2019). "Performance of carbon-coated nano-ZnO prepared by carbonizing gel precursor as anodic material for secondary alkaline Zn batteries." *Trans. Nonferrous Met. Soc. China*, 29(10), 2151–2159.

Peng, Q., and De, S. (2013). "Outstanding mechanical properties of monolayer MoS2 and its application in elastic energy storage." *Phys. Chem. Chem. Phys*., 15(44), 19427–19437.

156

Pham-Cong, D., Park, J. S., Kim, J. H., Kim, J., Braun, P. V., Choi, J. H., Kim, S. J., Jeong, S. Y., and Cho, C. R. (2017). "Enhanced cycle stability of polypyrrole-derived nitrogen-doped carbon-coated tin oxide hollow nanofibers for lithium battery anodes." *Carbon*, 111, 28–37.

Qiao, X. Q., Hu, F. C., Tian, F. Y., Hou, D. F., and Li, D. S. (2016). "Equilibrium and kinetic studies on MB adsorption by ultrathin 2D MoS$_2$ nanosheets." *RSC Adv.*, 6(14), 11631–11636.

Qin, S., Lei, W., Liu, D., and Chen, Y. (2014). "In-situ and tunable nitrogen-doping of MoS$_2$ nanosheets." *Sci. Rep.*, 4, 7582.

Ramarajan, R. (2019). "Thermal stability study of niobium doped SnO$_2$ thin film for transparent conducting oxide application." *Superlattices Microstruct.*, 135(August), 106274.

Rao, R., Islam, A. E., Campbell, P. M., Vogel, E. M., and Maruyama, B. (2017). "In situ thermal oxidation kinetics in few layer MoS$_2$." *2D Mater.*, 4(2), 025058.

Reddy, S. S., Shin, S., Aryal, U. K., Nishikubo, R., Saeki, A., Song, M., and Jin, S. H. (2017). "Highly efficient air-stable/hysteresis-free flexible inverted-type planar perovskite and organic solar cells employing a small molecular organic hole transporting material." *Nano Energy*, 41, 10–17.

Ren, L., Zhang, G., Lei, J., Hu, D., Dou, S., Gu, H., Li, H., and Zhang, X. (2019). "Growth of PANI thin layer on MoS$_2$ nanosheet with high electro-capacitive property for symmetric supercapacitor." *J. Alloys Compd.*, 798, 227–234.

Ren, X., Pang, L., Zhang, Y., Ren, X., Fan, H., and Liu, S. (2015). "One-step hydrothermal synthesis of monolayer MoS$_2$ quantum dots for highly efficient electrocatalytic hydrogen evolution." *J. Mater. Chem. A*, 3(20), 10693–10697.

Renuka, R., Srinivasan, L., Ramamurthy, S., Veluchamy, A., and Venkatakrishnan, N. (2001). "Cyclic voltammetric study of zinc and zinc oxide electrodes in 5.3 M KOH." *J. Appl. Electrochem.*, 31(6), 655–661.

Rong, Y., Yang, Z., Deng, L., and Fu, Z. (2020). "ZnO@Ag microspheres used as the anodic materials of superior alkaline rechargeable Zn–Ni batteries." *Ceram. Int.*, 46(10), 16908–16917.

Rothermel, S., Evertz, M., Kasnatscheew, J., Qi, X., Grützke, M., Winter, M., and Nowak, S. (2016). "Graphite Recycling from Spent Lithium-Ion Batteries." *ChemSusChem*, 9(24), 3473–3484.

Sadeghzadeh-Attar, A. (2018). "Efficient photocatalytic degradation of methylene blue dye by SnO_2 nanotubes synthesized at different calcination temperatures." *Sol. Energy Mater. Sol. Cells*, 183(April), 16–24.

Schmid, M., and Willert-Porada, M. (2018). "Zinc particles coated with bismuth oxide based glasses as anode material for zinc air batteries with improved electrical rechargeability." *Electrochim. Acta*, 260, 246–253.

Sepulveda-Mora, S. B., and Cloutier, S. G. (2012). "Figures of merit for high-performance transparent electrodes using dip-coated silver nanowire networks." *J. Nanomater.*, 2012.

Sharma, V., Koivikko, A., Yiannacou, K., Lahtonen, K., and Sariola, V. (2020). "Flexible biodegradable transparent heaters based on fractal-like leaf skeletons." *npj Flex. Electron.*, 4(1).

Shin, J., You, J. M., Lee, J. Z., Kumar, R., Yin, L., Wang, J., and Shirley Meng, Y. (2016). "Deposition of ZnO on bismuth species towards a rechargeable Zn-based aqueous battery." *Phys. Chem. Chem. Phys.*, 18(38), 26376–26382.

Silva, R. R. Da, Yang, M., Choi, S. Il, Chi, M., Luo, M., Zhang, C., Li, Z. Y., Camargo, P. H. C., Ribeiro, S. J. L., and Xia, Y. (2016). "Facile Synthesis of Sub-20 nm Silver Nanowires through a Bromide-Mediated Polyol Method." *ACS Nano*, 10(8), 7892–7900.

Sneha, C., Prabukumar, C., Jayalakshmi, M., and Bhat, K. U. (2017). "Structural and morphological changes with substrate heating in zinc films synthesized by thermal vapor deposition technique." *J. Mater. Sci. Mater. Electron.*, 28(11), 8038–8042.

Sonntag, L., Eichler, F., Weiß, N., Bormann, L., Ghosh, D. S., Sonntag, J. M., Jordan, R., Gaponik, N., Leo, K., and Eychmüller, A. (2019). "Influence of the average molar mass of poly(N-vinylpyrrolidone) on the dimensions and conductivity of silver nanowires." *Phys. Chem. Chem. Phys.*, 21(18), 9036–9043.

Spechler, J. A., and Arnold, C. B. (2012). "Direct-write pulsed laser processed silver nanowire networks for transparent conducting electrodes." *Appl. Phys. A Mater. Sci. Process.*, 108(1), 25–28.

Sreejesh, M., Huang, N. M., and Nagaraja, H. S. (2015). "Solar exfoliated graphene and its application in supercapacitors and electrochemical H_2O_2 sensing." *Electrochim. Acta*, 160, 94–99.

Sun, Y., Gates, B., Mayers, B., and Xia, Y. (2002a). "Crystalline Silver Nanowires by Soft Solution Processing." *Nano Lett.*, 2(2), 165–168.

Sun, Y., Mayers, B., Herricks, T., and Xia, Y. (2003). "Polyol synthesis of uniform silver nanowires: A plausible growth mechanism and the supporting evidence." *Nano Lett.*, 3(7), 955–960.

Sun, Y., and Xia, Y. (2002). "Large-scale synthesis of uniform silver nanowires through a soft, self-seeding, polyol process." *Adv. Mater.*, 14(11), 833–837.

Sun, Y., Yin, Y., Mayers, B. T., Herricks, T., and Xia, Y. (2002b). "Uniform silver nanowires synthesis by reducing $AgNO_3$ with ethylene glycol in the presence of seeds and poly(vinyl pyrrolidone)." *Chem. Mater.*, 14(11), 4736–4745.

Tang, Z., Kotov, N. A., and Giersig, M. (2002). "Spontaneous organization of single CdTe nanoparticles into luminescent nanowires." *Science*, 297(5579), 237–240.

Thakur, P., Kool, A., Hoque, N. A., Bagchi, B., Khatun, F., Biswas, P., Brahma, D., Roy, S., Banerjee, S., and Das, S. (2018). "Superior performances of in situ synthesized ZnO/PVDF thin film based self-poled piezoelectric nanogenerator and self-charged photo-power bank with high durability." *Nano Energy*, 44(December 2017), 456–467.

Tiwari, N., Ankit, Rajput, M., Kulkarni, M. R., John, R. A., and Mathews, N. (2017). "Healable and flexible transparent heaters." *Nanoscale*, 9(39), 14990–14997.

Tokuno, T., Nogi, M., Karakawa, M., Jiu, J., Nge, T. T., Aso, Y., and Suganuma, K. (2011). "Fabrication of silver nanowire transparent electrodes at room temperature." *Nano Res.*, 4(12), 1215–1222.

Tsai, M. L., Su, S. H., Chang, J. K., Tsai, D. S., Chen, C. H., Wu, C. I., Li, L. J., Chen, L. J., and He, J. H. (2014). "Monolayer MoS_2 heterojunction solar cells." *ACS Nano*, 8(8), 8317–8322.

Turney, D. E., Gallaway, J. W., Yadav, G. G., Ramirez, R., Nyce, M., Banerjee, S., Chen-Wiegart, Y. C. K., Wang, J., D'Ambrose, M. J., Kolhekar, S., Huang, J., and Wei, X. (2017). "Rechargeable Zinc Alkaline Anodes for Long-Cycle Energy Storage." *Chem. Mater.*, 29(11), 4819–4832.

Ullah, S., Ahmed, F., Badshah, A., Ali Altaf, A., Raza, R., Lal, B., and Hussain, R. (2013). "Solvothermal Preparation of ZnO Nanorods as Anode Material for Improved Cycle Life Zn/AgO Batteries." *PLoS One*, 8(10), 1–7.

Vialat, P., Leroux, F., and Mousty, C. (2015). "Electrochemical properties of layered double hydroxides containing 3d metal cations." J. *Solid State Electrochem.*, 19(7), 1975–1983.

Voiry, D., Salehi, M., Silva, R., Fujita, T., Chen, M., Asefa, T., Shenoy, V. B., Eda, G., and Chhowalla, M. (2013). "Conducting MoS_2 nanosheets as catalysts for hydrogen evolution reaction." *Nano Lett.*, 13(12), 6222–6227.

Wang, C., Zhu, G., Liu, P., and Chen, Q. (2020). "Monolithic Nanoporous Zn Anode for Rechargeable Alkaline Batteries." *ACS Nano*, 14(2), 2404–2411.

Wang, M., Fei, H., Zhang, P., and Yin, L. (2016a). "Hierarchically Layered MoS_2/Mn_3O_4 Hybrid Architectures for Electrochemical Supercapacitors with Enhanced Performance." *Electrochim. Acta*, 209, 389–398.

Wang, Q., Ping, P., Zhao, X., Chu, G., Sun, J., and Chen, C. (2012). "Thermal runaway caused fire and explosion of lithium ion battery." *J. Power Sources*, 208, 210–224.

Wang, R., and Yang, Z. (2013). "Synthesis and high cycle performance of Zn-Al-In-hydrotalcite as anode materials for Ni-Zn secondary batteries." *RSC Adv.*, 3(43), 19924–19928.

Wang, S., Tian, Y., Ding, S., and Huang, Y. (2016b). "Rapid synthesis of long silver nanowires by controlling concentration of Cu^{2+} ions." *Mater. Lett.*, 172, 175–178.

Wang, W., Li, L., Wu, K., Zhu, G., Tan, S., Li, W., and Yang, Y. (2015). "Hydrothermal synthesis of bimodal mesoporous MoS_2 nanosheets and their hydrodeoxygenation properties." *RSC Adv.*, 5(76), 61799–61807.

Wei, H., Hu, X., Zhang, X., Yu, Z., Zhou, T., Liu, Y., Liu, Y., Wang, Y., Xie, J., Sun, L., Liang, M., and Jiang, P. (2019). "Zn@C Core–Shell Nanocomposite for Rechargeable Aqueous Zn//MnO_2 Batteries with Long Lifetime." *Energy Technol.*, 7(4), 1–6.

Weng, Q., Wang, X., Wang, X., Zhang, C., Jiang, X., Bando, Y., and Golberg, D. (2015). "Supercapacitive energy storage performance of molybdenum disulfide nanosheets wrapped with microporous carbons." *J. Mater. Chem.* A, 3(6), 3097–3102.

Wiley, B., Herricks, T., Sun, Y., and Xia, Y. (2004). "Polyol synthesis of silver nanoparticles: Use of chloride and oxygen to promote the formation of single-crystal, truncated cubes and tetrahedrons." *Nano Lett.*, 4(9), 1733–1739.

Wiley, B., Sun, Y., Mayers, B., and Xia, Y. (2005). "Shape-controlled synthesis of metal nanostructures: The case of silver." *Chem. - A Eur. J.*, 11(2), 454-463.

Wiley, B., Sun, Y., and Xia, Y. (2007). "Synthesis of silver nanostructures with controlled shapes and properties." *Acc. Chem. Res.*, 40(10), 1067–1076.

Xu, F., Xu, W., Mao, B., Shen, W., Yu, Y., Tan, R., and Song, W. (2018). "Preparation and cold welding of silver nanowire based transparent electrodes with optical

transmittances >90% and sheet resistances <10 ohm/sq." *J. Colloid Interface Sci.*, 512, 208–218.

Xu, J., Li, Y., Huang, H., Zhu, Y., Wang, Z., Xie, Z., Wang, X., Chen, D., and Shen, G. (2011). "Synthesis, characterizations and improved gas-sensing performance of SnO_2 nanospike arrays." *J. Mater. Chem.*, 21(47), 19086–19092.

Xu, L. M., Ma, L., Xu, X. Y., Zhou, X. P., Zhang, L. L., and Chen, W. X. (2016). "Molybdenum disulfide microflowers assembled by few-layered nanosheets and their electrochemical performance for supercapacitor." *Mater. Lett.*, 173, 84–87.

Xu, Y., Zhang, C., Kuang, S., Zhao, K., Chen, M., Xu, D., Chen, W., and Yu, X. (2019). "Facile synthesis and electrochemical performances of activated bamboo charcoal supported MoS_2 nanoflakes as anodes materials for lithium-ion batteries." *J. Electroanal. Chem.*, 847(December 2018), 113265.

Yan, J., Wang, Q., Wei, T., and Fan, Z. (2014). "Recent advances in design and fabrication of electrochemical supercapacitors with high energy densities." *Adv. Energy Mater.*, 4(4), 1300816.

Yan, X., Chen, Z., Wang, Y., Li, H., and Zhang, J. (2018a). "In-situ growth of ZnO nanoplates on graphene for the application of high rate flexible quasi-solid-state Ni-Zn secondary battery." *J. Power Sources*, 407(October), 137–146.

Yan, Y., Zhang, Y., Wu, Y., Wang, Z., Mathur, A., Yang, H., Chen, P., Nair, S., and Liu, N. (2018b). "A Lasagna-Inspired Nanoscale ZnO Anode Design for High-Energy Rechargeable Aqueous Batteries." *ACS Appl. Energy Mater.*, 1(11), 6345–6351.

Yang, B., and Yang, Z. (2013). "Structure and improved electrochemical performance of a nanostructured layered double hydroxide-carbon nanotube composite as a novel anode material for Ni-Zn secondary batteries." *RSC Adv.*, 3(31), 12589–12592.

Yang, B., Yang, Z., Peng, Z., and Liao, Q. (2014a). "Effect of silver additive on the electrochemical performance of ZnAl-layered double hydroxide as anode material for nickel-zinc rechargeable batteries." *Electrochim. Acta*, 132, 83–90.

Yang, B., Yang, Z., and Wang, R. (2014b). "Facile synthesis of novel two-dimensional silver-coated layered double hydroxide nanosheets as advanced anode material for Ni-Zn secondary batteries." *J. Power Sources*, 251, 14–19.

Yang, C., Zhang, Z., Tian, Z., Zhang, K., Li, J., and Lai, Y. (2018). "Communication— Bi@CMC Composite as a Multifunctional Electrolyte Channel for the Anode of Rechargeable Zn–Ni Battery." *J. Electrochem. Soc.*, 165(2), A86–A88.

Yang, L., Zhang, T., Zhou, H., Price, S. C., Wiley, B. J., and You, W. (2011). "Solution-processed flexible polymer solar cells with silver nanowire electrodes." *ACS Appl. Mater. Interfaces*, 3(10), 4075–4084.

Yu, Y., Li, C., Liu, Y., Su, L., Zhang, Y., and Cao, L. (2013). "Controlled scalable synthesis of uniform, high-quality monolayer and few-layer MoS_2 films." *Sci. Rep.*, 3, 1866.

Yuan, H., Lei, T., Qin, Y., and Yang, R. (2019). "Flexible electronic skins based on piezoelectric nanogenerators and piezotronics." *Nano Energy*, 59(January), 84–90.

Yuan, Y. F., Li, Y., Tao, S., Ye, F. C., Yang, J. L., Guo, S. Y., and Tu, J. P. (2009). "Preparation and electrochemical performance of nanosized Bi compounds-modified ZnO for Zn/Ni secondary cell." *Electrochim. Acta*, 54(26), 6617–6621.

Yuan, Y. F., Tu, J. P., Wu, H. M., Li, Y., and Shi, D. Q. (2005). "Size and morphology effects of ZnO anode nanomaterials for Zn/Ni secondary batteries." *Nanotechnology*, 16(6), 803–808.

Zeng, X., Yang, Z., Cui, F., Chen, L., Meng, J., and Chen, H. (2020a). "The dodecahedral Nitrogen-doped carbon coated ZnO composite derived from zeolitic inidazolate framework-8 with excellent cycling performance for zinc based rechargeable batteries." *J. Power Sources*, 463(December 2019), 228193.

Zeng, X., Yang, Z., Fan, M., Cui, F., Meng, J., Chen, H., and Chen, L. (2020b). "Shape-controlled growth of three-dimensional flower-like ZnO@Ag composite and its outstanding electrochemical performance for Ni-Zn secondary batteries." *J. Colloid Interface Sci.*, 562, 518–528.

Zeng, X., Yang, Z., Liu, F., Long, J., Feng, Z., and Fan, M. (2017). "An In situ recovery method to prepare carbon-coated Zn-Al-hydrotalcite as the anode material for nickel-zinc secondary batteries." *RSC Adv.*, 7(70), 44514–44522.

Zeng, X., Zhou, B., Gao, Y., Wang, C., Li, S., Yeung, C. Y., and Wen, W. J. (2014). "Structural dependence of silver nanowires on polyvinyl pyrrolidone (PVP) chain length." *Nanotechnology*, 25(49), 495601.

Zhang, B., Dang, R., Cao, Q., Zhao, P., Chen, K., and Meng, H. (2019). "High-yield synthesis of long silver nanowires via chromic chloride and a stable reaction environment." *J. Nanomater.*, 2019.

Zhang, D., Qi, L., Ma, J., and Cheng, H. (2001). "Formation of silver nanowires in aqueous solutions of a double-hydrophilic block copolymer." *Chem. Mater.*, 13(9), 2753–2755.

Zhang, D., Sun, Y., Jiang, C., and Zhang, Y. (2017a). "Room temperature hydrogen gas sensor based on palladium decorated tin oxide/molybdenum disulfide ternary hybrid via hydrothermal route." *Sensors Actuators, B Chem.*, 242(January 2017), 15–24.

Zhang, H., Wang, S., Tian, Y., Wen, J., Hang, C., Zheng, Z., Huang, Y., Ding, S., and Wang, C. (2020a). "High-efficiency extraction synthesis for high-purity copper nanowires and their applications in flexible transparent electrodes." *Nano Mater. Sci.*, 2(2), 164–171.

Zhang, H., Wei, J., Yan, Y., Guo, Q., Xie, L., Yang, Z., He, J., Qi, W., Cao, Z., Zhao, X., Pan, P., Li, H., Zhang, K., Zhao, J., Li, X., Zhang, P., and Shah, K. W. (2020b). "Facile and scalable fabrication of MnO_2 nanocrystallines and enhanced electrochemical performance of MnO_2/MoS_2 inner heterojunction structure for supercapacitor application." *J. Power Sources*, 450(November 2019).

Zhang, K., Du, Y., and Chen, S. (2015). "Sub 30 nm silver nanowire synthesized using KBr as co-nucleant through one-pot polyol method for optoelectronic applications." *Org. Electron.*, 26, 380–385.

Zhang, P., Wei, Y., Ou, M., Huang, Z., Lin, S., Tu, Y. Y., and Hu, J. (2018a). "Behind the role of bromide ions in the synthesis of ultrathin silver nanowires." *Mater. Lett.*, 213, 23–26.

Zhang, Y., Guo, J., Xu, D., Sun, Y., and Yan, F. (2017b). "One-Pot Synthesis and Purification of Ultralong Silver Nanowires for Flexible Transparent Conductive Electrodes." *ACS Appl. Mater. Interfaces*, 9(30), 25465–25473.

Zhang, Y., Wu, Y., Ding, H., Yan, Y., Zhou, Z., Ding, Y., and Liu, N. (2018b). "Sealing ZnO nanorods for deeply rechargeable high-energy aqueous battery anodes." *Nano Energy*, 53(September), 666–674.

Zhang, Y., Wu, Y., You, W., Tian, M., Huang, P. W., Zhang, Y., Sun, Z., Ma, Y., Hao, T., and Liu, N. (2020c). "Deeply Rechargeable and Hydrogen-Evolution-Suppressing Zinc Anode in Alkaline Aqueous Electrolyte." *Nano Lett.*, 20(6), 4700–4707.

Zhang, Z., Yang, Z., Wang, R., Feng, Z., Xie, X., and Liao, Q. (2014). "Electrochemical performance of ZnO/SnO$_2$ composites as anode materials for Zn/Ni secondary batteries." *Electrochim. Acta*, 134, 287–292.

Zhao, K., Wang, C., Yu, Y., Yan, M., Wei, Q., He, P., Dong, Y., Zhang, Z., Wang, X., and Mai, L. (2018). "Ultrathin Surface Coating Enables Stabilized Zinc Metal Anode." *Adv. Mater. Interfaces*, 5(16).

Zhao, T., Shangguan, E., Li, Y., Li, J., Chang, Z., Li, Q., Yuan, X. Z., and Wang, H. (2015). "Facile synthesis of high tap density ZnO microspheres as advanced anode material for alkaline nickel-zinc rechargeable batteries." *Electrochim. Acta*, 182, 173–182.

Zhao, Y., Xu, L., Yan, J., Yan, W., Wu, C., Lian, J., Huang, Y., Bao, J., Qiu, J., Xu, L., Xu, Y., Xu, H., and Li, H. (2017). "Facile preparation of NiFe$_2$O$_4$/MoS$_2$ composite material with synergistic effect for high performance supercapacitor." *J. Alloys Compd.*, 726, 608–617.

Zheng, X., Ji, Y., Tang, J., Wang, J., Liu, B., Steinrück, H. G., Lim, K., Li, Y., Toney, M. F., Chan, K., and Cui, Y. (2019). "Theory-guided Sn/Cu alloying for efficient CO_2 electroreduction at low overpotentials." *Nat. Catal*., 2(1), 55–61.

Zhou, D., Song, W. L., Li, X., and Fan, L. Z. (2016). "Hierarchical porous reduced graphene oxide/SnO_2 networks as highly stable anodes for lithium-ion batteries." *Electrochim. Acta*, 207, 9–15.

Zhou, L., He, B., Yang, Y., and He, Y. (2014). "Facile approach to surface functionalized MoS_2 nanosheets." *RSC Adv*., 4(61), 32570–32578.

Zhu, J. J., Kan, C. X., Wan, J. G., Han, M., and Wang, G. H. (2011). "High-yield synthesis of uniform Ag nanowires with high aspect ratios by introducing the long-chain PVP in an improved polyol process." *J. Nanomater*., 2011.

Zhu, S., Gao, Y., Hu, B., Li, J., Su, J., Fan, Z., and Zhou, J. (2013). "Transferable self-welding silver nanowire network as high performance transparent flexible electrode." *Nanotechnology*, 24(33), 335202.

Zong, R. L., Zhou, J., Li, Q., Du, B., Li, B., Fu, M., Qi, X. W., Li, L. T., and Buddhudu, S. (2004). "Synthesis and optical properties of silver nanowire arrays embedded in anodic alumina membrane." *J. Phys. Chem. B*, 108(43), 16713–16716.
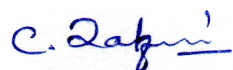
List of publications based on PhD Research Work

Sl. No.	Title of the paper/book chapter	Authors (in the same order as in the paper. Underline the Research Scholar's name)	Name of the Journal/book Conference/ Symposium, Vol., No., Pages	Month & Year of Publication	Category *
1	Purification of silver nanowires synthesised by polyol method.	<u>Prabukumar C.</u> and Udaya Bhat K.	Materials Today: Proceedings Vol: 5, Page: 22487–22493	November 2018	3
2	Effect of solvent on the morphology of MoS_2 nanosheets prepared by ultrasonication-assisted exfoliation	<u>Prabukumar C.</u>, Sadiq M. M. J., Bhat D. K. and Udaya Bhat K.	AIP Conference Proceedings Vol.: 1943 Page: 020084	April 2018	3
3	SnO_2 nanoparticles functionalized MoS_2 nanosheets as the electrode material for supercapacitor applications	<u>Prabukumar C.</u>, Sadiq M. M. J., Bhat D. K. and Udaya Bhat K.	Materials Research Express Vol.: 6, Pages: 085526	May 2019	1
4	Beneficial Effect of Manganese (II) Ions on the Morphology of Polyol Synthesised Silver Nanowires	<u>Prabukumar C.</u> and Udaya Bhat K.	Electronic Materials Letters Vol.: 16, Pages: 264-275	April 2020	1
5	Enhancing the electrochemical performance of ZnO anode by novel additive of MoS_2-SnO_2 nanocomposite for the zinc alkaline battery application	<u>Prabukumar C.</u>, Sunil Meti and Udaya Bhat K.	Journal of Materials Science: Materials in Electronics	*Accepted for Publication*	1

* Category: 1. Journal paper, full paper reviewed

                     2. Journal paper, Abstract reviewed

                     3. Conference/Symposium paper, full paper reviewed

                     4. Conference/Symposium paper, abstract reviewed

                     5. Others (including papers in Workshops, NITK Research Bulletins, Short notes etc.)

(If the paper has been accepted for publication but yet to be published, the supporting documents must be attached.)

Research Scholar   **Research Guide**

(Prabukumar C.)   (Prof. Udaya Bhat K.)

Date: 29.11.2021   Date: 29.11.2021

Page intentionally left blank

BIO-DATA

Name   : Prabukumar C.

Father's name   : Chinnusamy N.

Date of Birth   : 09-05-1989

Permanent address   : 4, C.H.B. colony west, Velur road,

                                  Tiruchengode, Namakkal - 637211

                                  Tamil Nadu.

Contact number   : +91-9740253476

                                  +91-9500933339

E-mail ID   : cprabumech@gmail.com

Academic Qualification:

Bachelor of Engineering (B.E.) in Mechanical Engineering from Kongu Engineering College, Perundurai, Erode (Affiliated to Anna University, Chennai) (2010).

Master of Technology (M.Tech.) in Materials Engineering from National Institute of Technology, Karnataka (NITK), Surathkal (2014).

List of Publications:

1. **Prabukumar, C.**, Sunil Meti and Bhat, K. U. "Enhancing the electrochemical performance of ZnO anode with 1-D morphology and MoS_2-SnO_2 nanocomposite additive for zinc alkaline battery application." submitted to *Journal of Materials Science: Materials in Electronics* (*Accepted for publication*)

2. **Prabukumar, C**. and Bhat, K. U. (2020). "Beneficial Effect of Manganese (II) Ions on the Morphology of Polyol Synthesised Silver Nanowires." *Electronic Materials Letters*, *16*(3), 264-275. DOI: 10.1088/2053-1591/ab2200

3. **Prabukumar, C**., Sadiq, M. M. J., Bhat, D. K. and Bhat, K. U. (2019). "SnO$_2$ nanoparticles functionalized MoS$_2$ nanosheets as the electrode material for supercapacitor applications." *Materials Research Express*, *6*(8), 085526. DOI: 10.1007/s13391-020-00211-6

4. **Prabukumar, C**., Sadiq, M. M. J., Bhat, D. K. and Bhat, K. U. (2018). "Effect of solvent on the morphology of MoS$_2$ nanosheets prepared by ultrasonication-assisted exfoliation." *AIP Conference Proceedings*, 1943(1), 020084. DOI: 10.1063/1.5029660

5. **Prabukumar, C**. and Bhat, K. U. (2018). Purification of silver nanowires synthesised by polyol method. *Materials Today: Proceedings*, *5*(10), 22487-22493. DOI: 10.1016/j.matpr.2018.06.620

6. **Prabukumar, C**., Jayalakshmi, M. and Udaya Bhat, K. (2015). Characterization of ZnO films produced by thermal evaporation and oxidation. *Materials Science Forum*, 830, 403-406. DOI:10.4028/www.scientific.net/MSF.830-831.403

7. Sneha, C., **Prabukumar, C**., Jayalakshmi, M., Bhat, S. and Bhat, K. U. (2017). Effect of substrate temperature on the characteristics of ZnO films produced by a combination of thermal vapor deposition and oxidation processes. *Journal of Materials Science: Materials in Electronics*, 28(21), 15959-15966. DOI: 10.1007/s10854-017-7493-2

8. Sneha, C., **Prabukumar, C**., Jayalakshmi, M. and Bhat, K. U. (2017). Structural and morphological changes with substrate heating in zinc films synthesized by thermal vapor deposition technique. *Journal of Materials Science: Materials in Electronics*, 28(11), 8038-8042. DOI: 10.1007/s10854-017-6509-2

9. Bhat, K. U., Meti, S., **Prabukumar, C**., and Bhat, S. (2020). Metal Sulphides for Lithium-ion Batteries. Lithium-ion Batteries: Materials and Applications, *Materials Research Foundations* 80, 91-122. DOI: 10.21741/9781644900918-4 (Book chapter)